

University of Windsor

## Scholarship at UWindsor

---

Electronic Theses and Dissertations

Theses, Dissertations, and Major Papers

---

1-1-1966

### Paramagnetic resonance of iron(3+) and manganese(2+) ions in natural crystals of spodumene.

Armen Manoogian  
*University of Windsor*

Follow this and additional works at: <https://scholar.uwindsor.ca/etd>

---

#### Recommended Citation

Manoogian, Armen, "Paramagnetic resonance of iron(3+) and manganese(2+) ions in natural crystals of spodumene." (1966). *Electronic Theses and Dissertations*. 6043.  
<https://scholar.uwindsor.ca/etd/6043>

This online database contains the full-text of PhD dissertations and Masters' theses of University of Windsor students from 1954 forward. These documents are made available for personal study and research purposes only, in accordance with the Canadian Copyright Act and the Creative Commons license—CC BY-NC-ND (Attribution, Non-Commercial, No Derivative Works). Under this license, works must always be attributed to the copyright holder (original author), cannot be used for any commercial purposes, and may not be altered. Any other use would require the permission of the copyright holder. Students may inquire about withdrawing their dissertation and/or thesis from this database. For additional inquiries, please contact the repository administrator via email ([scholarship@uwindsor.ca](mailto:scholarship@uwindsor.ca)) or by telephone at 519-253-3000ext. 3208.

PARAMAGNETIC RESONANCE OF  $\text{Fe}^{+3}$  AND  $\text{Mn}^{+2}$  IONS  
IN NATURAL CRYSTALS OF SPODUMENE.

BY

ARMEN MANOOGIAN

A Thesis

Submitted to the Faculty of Graduate Studies through the  
Department of Physics in Partial Fulfillment of  
the Requirements for the Degree of Doctor  
of Philosophy at the University  
of Windsor.

Windsor, Ontario

1966

UMI Number: DC52606

### INFORMATION TO USERS

The quality of this reproduction is dependent upon the quality of the copy submitted. Broken or indistinct print, colored or poor quality illustrations and photographs, print bleed-through, substandard margins, and improper alignment can adversely affect reproduction.

In the unlikely event that the author did not send a complete manuscript and there are missing pages, these will be noted. Also, if unauthorized copyright material had to be removed, a note will indicate the deletion.

**UMI**®

---

UMI Microform DC52606

Copyright 2008 by ProQuest LLC.

All rights reserved. This microform edition is protected against unauthorized copying under Title 17, United States Code.

ProQuest LLC  
789 E. Eisenhower Parkway  
PO Box 1346  
Ann Arbor, MI 48106-1346

11/21/67

Approved

*F. Holuj*

Dr. F. Holuj  
(Supervisor)

*N.E. Hedgecock*

Dr. N.E. Hedgecock

*E.E. Habib*

Dr. E.E. Habib

147498

ABSTRACT

The paramagnetic resonance spectra of  $\text{Fe}^{+3}$  and  $\text{Mn}^{+2}$  impurity ions in natural crystals of spodumene,  $\text{LiAl}(\text{SiO}_3)_2$ , and its varieties of kunzite and hiddenite, were studied at room temperature and at k-band microwave frequencies. The spectra were fitted to an appropriate spin Hamiltonian for S-state ions in crystalline electric fields of orthorhombic symmetry. The spin Hamiltonian, including hyperfine structure, is given by

$$\begin{aligned} \mathcal{H} = & \beta g_x S_x H_x + \beta g_y S_y H_y + \beta g_z S_z H_z \\ & + \frac{1}{3} b_2^0 b_2^0 + \frac{1}{3} b_2^2 b_2^2 + \frac{1}{60} b_4^0 b_4^0 + \frac{1}{60} b_4^2 b_4^2 + \frac{1}{60} b_4^4 b_4^4 \\ & + A I_z S_z + B I_y S_y + C I_x S_x . \end{aligned}$$

The parameters for  $\text{Fe}^{+3}$  were determined as:

$$g_x = 2.0047 \pm 10, \quad g_y = 2.0047 \pm 10, \quad g_z = 2.0041 \pm 5, \\ b_2^0 = 1,430, \quad b_2^2 = 280, \quad b_4^0 = 20, \quad b_4^2 = -82, \quad \text{and} \quad b_4^4 = 202$$

The values of  $b_n^m$  are in gauss. The parameters for the four  $\text{Mn}^{+2}$  complexes are given in the text. The signs of  $b_2^0$  were determined by examining the relative intensities of the spectra at  $4.2^\circ\text{K}$ . Using the values of the parameters, the energy levels were plotted as a function of the externally applied magnetic field.

The crystals were thermally quenched from various elevated temperatures to room temperature and the EPR spectra of both  $\text{Fe}^{+3}$  and  $\text{Mn}^{+2}$  were re-examined. It was found that the

spectral lines due to the four  $Mn^{+2}$  complexes gradually decreased their intensities while spectral lines due to  $Mn^{+2}$  in a single complex formed and increased their intensities with increasing temperature. Also, the line widths of  $Fe^{+3}$  increased. The spin Hamiltonian parameters for the single  $Mn^{+2}$  spectrum were calculated to be:  $g_y = 1.9972 \pm 25$ ,  $g_z = 2.0012 \pm 10$ ,  $A = -89.2$ ,  $B = -88.4$ ,  $b_2^0 = 577$ ,  $b_2^2 = 243$ ,  $b_4^0 = -1.07$ ,  $b_4^2 = 35$ ,  $b_4^4 = -44$ . The values of  $A$ ,  $B$  and  $b_n^m$  are again in gauss. A possible mechanism for the changed spectra of the thermally quenched samples is discussed in the text.

## ACKNOWLEDGEMENTS

The author wishes to thank Dr. F. Holuj for suggestion of the problem and for guidance during the course of the research. Helpful suggestions from Dr. J. Thyer regarding experimental techniques are also greatly appreciated. Thanks are also due to Mr. W. Grewe and the machine shop staff for construction of apparatus. Financial assistance in the form of an Ontario Government Research Fellowship is gratefully acknowledged.

## TABLE OF CONTENTS

	Page
ABSTRACT .....	ii
ACKNOWLEDGEMENTS .....	iv
LIST OF TABLES .....	vii
LIST OF FIGURES .....	viii
I. INTRODUCTION .....	1
II. CRYSTALLOGRAPHY .....	9
III. THEORY .....	18
A. Crystal Field Theory .....	18
B. Zeeman Interaction .....	19
C. Hyperfine Structure .....	20
D. The Spin Hamiltonian .....	21
(i) Zeeman interaction .....	22
(ii) Hyperfine interaction .....	22
(iii) Crystalline electric field interaction.	23
E. EPR Transitions For Fe <sup>+3</sup> In Spodumene .....	24
F. EPR Transitions For Mn <sup>+2</sup> In Kunzite .....	27
G. EPR Linewidths .....	29
(i) Spin - lattice interaction .....	29
(ii) Spin - spin interaction .....	30
H. Comparison Of Spin Hamiltonian And Quadrupole Resonance Parameters .....	30
IV. EQUIPMENT .....	36
A. K-Band Spectrometer .....	36
B. X-Band Spectrometer Used At Room Temperature.	38

	Page
C. X-Band Spectrometer Used At Liquid Helium	
Temperature .....	38
D. K-Band Cavities .....	40
E. X-Band Cavity .....	45
F. Crystal Heating Equipment .....	47
G. Magnetic Field Measurement .....	47
H. Microwave Frequency Measurement .....	49
V. EXPERIMENTAL PROCEDURE AND RESULTS .....	51
A. Fe <sup>+3</sup> In Spodumene .....	51
(i) Determination of the magnetic axes ....	51
(ii) Comparison of Fe <sup>+3</sup> spectra at room and liquid helium temperatures .....	53
(iii) Calculation of spin Hamiltonian parameters for Fe <sup>+3</sup> in spodumene .....	56
(iv) Heat-treatment of spodumene .....	58
(v) Line intensities of Fe <sup>+3</sup> in spodumene..	58
B. Mn <sup>+2</sup> In Kunzite .....	63
(i) Determination of the magnetic axes ....	65
(ii) Comparison of Mn <sup>+2</sup> spectra at room and liquid helium temperatures .....	68
(iii) Calculation of spin Hamiltonian parameters for Mn <sup>+2</sup> in kunzite .....	70
(iv) Heat-treatment of kunzite .....	71
C. Analysis Of Hiddenite Crystals .....	79
VI. DISCUSSION AND CONCLUSIONS .....	81
REFERENCES .....	89
VITA AUCTORIS .....	92

## LIST OF TABLES

Table		Page
1	Characteristics Of Ions In Spodumene	11
2	The Chief Isotopes Of Iron And Manganese With Some Of Their Characteristics	12
3	Matrix Of The Spin Hamiltonian (eq. (4)) In The $S=5/2$ Manifold	25
4	Relationship Between The Constants Of The Spin Hamiltonian For Different Orientations Of The Magnetic Field H	27
5	Resonant Fields Of $Fe^{+3}$ EPR Lines In Spodumene Along The Magnetic Axes	53
6	Line Widths And Integrated Intensities Of The Five Iron Lines In Spodumene Before And After Heat-Treatment	63
7	Magnetic Field Positions For The $m_I=5/2$ Transitions Of Each Group Of Hyperfine Lines In Each Of The Four Complexes	68
8	The Spin Hamiltonian Parameters For The Four Magnetic Complexes Of $Mn^{+2}$ In Kunzite	70
9	Magnetic Field Positions For The $m_I=+5/2$ Transitions Of Each Group Of Hyperfine Lines In Heat-Treated Kunzite	77
10	Line Widths And Integrated Intensities Of The Five Iron Lines In Hiddenite Before And After Heat-Treatment	79
11	Summary Of Data Obtained In Electric Quadropole Resonance In Spodumene And EPR Of $Fe^{+3}$ And $Mn^{+2}$ In Spodumene And Heat-Treated Kunzite	82

## LIST OF FIGURES

Figure		Page
1	Pyroxene structure, $(\text{SiO}_3)_n$ .	10
2	The projection of a unit cell of spodumene in the (010) plane.	13
3	Diagram showing the oxygen ions surrounding (a) $\text{Al}^{+3}$ and (b) $\text{Li}^+$ ions in spodumene.	14
4	X-ray photographs.	16
5	Block diagram of k-band spectrometer used for EPR measurements at room temperature.	37
6	Block diagram of x-band spectrometer used for EPR experiments at room temperature.	39
7	Block diagram of x-band superheterodyne spectrometer used for EPR measurements at liquid helium temperatures.	41
8	K-band cavity system with vertical crystal mount.	42
9	K-band cavity system with horizontal crystal mount.	43
10	X-band cavity system with horizontal crystal mount.	46
11	Crystal heat-treatment apparatus.	48
12	The spectrum of $\text{Fe}^{+3}$ ions in spodumene with the magnetic field along the z-axis.	52
13	Angular variation of the EPR spectrum $\text{Fe}^{+3}$ in the plane perpendicular to the magnetic x-axis.	54
14	Angular variation of the EPR spectrum of $\text{Fe}^{+3}$ in the plane perpendicular to the magnetic z-axis.	55
15	Comparison of the $\text{Fe}^{+3}$ spectra for the magnetic field along the z-axis at (a) room temperature	

	Page
and (b) liquid helium temperature.	57
16 Energy level diagram of $\text{Fe}^{+3}$ with the magnetic field along the z-axis.	59
17 Energy level diagram of $\text{Fe}^{+3}$ with the magnetic field along the y-axis.	60
18 Energy level diagram of $\text{Fe}^{+3}$ with the magnetic field along the x-axis.	61
19 The spectrum of heat-treated spodumene with the magnetic field along the z-axis of $\text{Fe}^{+3}$ .	62
20 A typical spectrum near the z-axes of the four magnetic complexes of $\text{Mn}^{+2}$ in kunzite.	64
21 Stereographic projection of the $\text{Mn}^{+2}$ magnetic axes in kunzite, along with the oxygen ligands surrounding an $\text{Al}^{+3}$ site.	66
22 Stereographic projection of the $\text{Mn}^{+2}$ magnetic axes in kunzite, along with the oxygen ligands surrounding an $\text{Li}^{+}$ site.	67
23 Comparison of the $\text{Mn}^{+2}$ spectra in kunzite for the magnetic field near the z-axis at (a) room temperature and (b) liquid helium temperature.	69
24 Energy level diagram of $\text{Mn}^{+2}$ in kunzite with the magnetic field direction along the z-axis.	72
25 Energy level diagram of $\text{Mn}^{+2}$ in kunzite with the magnetic field direction along the y-axis.	73
26 Energy level diagram of $\text{Mn}^{+2}$ in kunzite with the magnetic field direction along the x-axis.	74
27 Gradual collapse of the four $\text{Mn}^{+2}$ complexes in kunzite as a result of thermal quenching from various elevated temperatures.	75
28 The spectra of $\text{Mn}^{+2}$ in heat-treated kunzite.	76
29 Increase of amplitude ratios with increase of temperature.	78
30 Spectra of hiddenite with the magnetic field along the z-axis of $\text{Fe}^{+3}$ .	80

	Page	
31	Diagrams illustrating the mechanism causing broadening of the $\text{Fe}^{+3}$ lines.	85
32	Dissociation energy curve.	87

# I

## INTRODUCTION

The technique of electron paramagnetic resonance (EPR) permits an accurate description of the ground state and of the effect of the crystalline environment on the energy levels of a paramagnetic ion. Recently there has been an intensive study of S-state ions, especially those of the first transition series,  $\text{Fe}^{+3}$  and  $\text{Mn}^{+2}$ , which appear as impurities in natural minerals. Their ground states, which are spin sextets  $3d^5 \ ^6S_{5/2}$  in the free ionic state, or  $(dt_2)^3 (de)^2 \ ^6A_1$  in cubic symmetry, are very sensitive to the crystalline electric fields. The effect of a crystalline electric field on the energy levels is to remove the degeneracy either wholly or in part. This effect, commonly known as zero field splitting, is present in all experiments published to date.

A paramagnetic ion in the ground S-state has zero angular momentum ( $L=0$ ), hence it should not be directly affected by any crystalline electric field or by spin-orbit coupling. Bleaney and Ingram<sup>1</sup> investigated the EPR spectrum of manganese in Tutton salts and in manganese fluosilicate. They show that the  $\ ^6S_{5/2}$  state is split mainly by the small deviations from cubic symmetry in these crystals. The levels are split into three doublets of separation 0.061 and 0.109  $\text{cm}^{-1}$

between the  $M_S = \pm 1/2 \rightarrow \pm 3/2$  and  $M_S = \pm 3/2 \rightarrow \pm 5/2$  levels, respectively. The splitting by the predominantly cubic field is small and approximately  $0.002 \text{ cm}^{-1}$ .

Van Vleck and Penney<sup>2</sup> first discussed the mechanism by which such a splitting can be effected, and showed that a small admixture to the  ${}^6S_{5/2}$  state of small amounts of higher multiplets and configurations can cause a splitting by the crystalline electric field  $V$  and spin-orbit coupling  $W_{LS}$  through various higher order interactions. Since  $L=0$ , there is no first order effect due to spin-orbit coupling, and no first order effect due to the crystal field on the sixfold spin degenerate ground state.

Abragam and Pryce<sup>3</sup> suggested another mechanism, of second order, which might be responsible for the splitting of the  ${}^6S_{5/2}$  level, involving the spin-spin interaction  $W_{SS}$  between the  $3d^5$  electrons of the paramagnetic ion. The mechanism whereby such splitting takes place can be described as follows. In each of the substates  $M_S = 5/2, 3/2 \dots -5/2$ , which correspond to the various orientations of the total spin  $S$ , the spins of the individual  $3d^5$  electrons are also differently oriented. The dipole - dipole interaction between spin magnetic moments of the electrons depends on the orientation, and the total interaction energy is obtained by averaging this effect over the electron cloud distribution. When the distribution has spherical or cubic symmetry the resultant energy is independent of orientation, and this mechanism would not be operative. But when this cloud is distorted to a shape of lower symmetry, the different levels of

$M_S$  will no longer have the same energy. Since the magnetic interaction is not altered by reversing all the spins, the states  $+M_S$  and  $-M_S$  remain degenerate, and the Hamiltonian can be written as a sum of squares of the spin components  $S_x$ ,  $S_y$  and  $S_z$ . Hence it corresponds to an interaction of lower order than those considered by Van Vleck and Penny, and my outweigh them.

Watanabe<sup>4</sup> considered the problem of S-state splitting in detail and concluded that any perturbation of the ground state arising from higher order multiplets of the  $3d^5$  configuration involves the crystalline potential  $V$  to even powers only and will first appear as  $V^2$ . Perturbations arising from different configurations such as  $3d^4 4s$  can involve  $V$  to the first power; but for cubic crystalline electric fields this linear dependence is generally expected to be less than one-tenth as effective because of the greater energy separations of the different configurations from the ground state. More recently, Gabriel, Johnson and Powell<sup>5</sup> criticized Watanabe's results and performed a detailed calculation of the ground state splitting showing that contributions to this splitting which are odd in  $V$  also arise from higher order multiplets of the  $3d^5$  configuration.

The  $Fe^{+3}$  ion is commonly observed to have a small positive departure of  $g$  from the free spin value (2.0023) while  $Mn^{+2}$  has a negative departure. If the ground state of these ions was pure  ${}^6S_{5/2}$  then the  $g$  - factor would be equal to the free spin value. The theory of negative departure was developed by Watanabe<sup>4</sup> who attributed it to the admixture of the  ${}^4P$ - derived wave function to the ground state through  $W_{LS}$ . The calculation

was carried out in an approximation involving the intermediate crystal field. Leushin<sup>6</sup>, taking into account the fact that the effect of the crystal field on the ions investigated is of the same order of magnitude as the electrostatic interaction of their electrons, found that not only  $4P$  but also  $4F$  and  $4G$  states are admixed to the  $6S_{5/2}$  state. The resulting  $g$  - factor can be greater than 2.0023. The theory of positive departure was also developed by Watanabe<sup>7</sup> who attributed it to covalent bonding. Electron transfer processes through spin-orbit interaction from the ligands to the S-state ions were found to give rise to positive  $g$  shifts in cubic crystals.

Owen<sup>8</sup> discussed the influence of covalent bonding on the paramagnetic resonance spectra of the hydrated iron group. In the case of manganese having a  $(dt_2)^3 (de)^2$  configuration he showed that the  $dt_2$  electrons form molecular  $\pi$  - bonds with the  $2P_{\pi}$  electrons of adjacent oxygen ions, while the  $d_e$  electrons form  $\sigma$  - bonds with the  $2P_{\sigma}$  and  $2s$  electrons of the oxygen ions. The effect of  $\pi$  and  $\sigma$  bonding is very similar to an increase in the crystal field strength, resulting in the increase of the cubic field splitting.

According to Van Wieringen<sup>9</sup> there is an apparent correlation between the amount of covalent bonding and the decrease of the hyperfine splitting. That is, the greater the covalent bonding the smaller is the hyperfine splitting. Matumura<sup>10</sup> plots percent ionicity against the hyperfine splitting  $A$  for various host lattices. Using this plot one can obtain an estimate of the amount of covalency of  $Mn^{+2}$  in a particular crys-

tal.

It has been shown by Watkins<sup>11</sup>, for  $Mn^{+2}$  in NaCl, that impurity ions substituting for ions of different valency attract charge compensating defects in the lattice at temperatures at which the ions become mobile. Other indications of possible local charge compensation have come from EPR studies of chromium in  $TiO_2$  by Gerritsen<sup>12</sup>, of nickel in  $SrTiO_3$  by Rubins and Low<sup>13</sup> and of iron in  $SrTiO_3$  by Kirkpatrick et al<sup>14</sup>. The latter obtained a strong axial EPR spectrum for iron - doped strontium titanate which is attributed to local charge compensation taking place at a nearest oxygen site in the octahedron surrounding the iron impurity.

$Mn^{+2}$  impurity in diopside  $CaMg(SiO_3)_2$ , a crystal having spodumene structure, was investigated recently by Vinokurov et al<sup>15</sup>. They found that manganese enters both the  $Mg^{+2}$  and  $Ca^{+2}$  sites in about the same proportion. The spectra show that the manganese sites have moderately strong orthorhombic distortions from cubic symmetry.

Spodumene has been a subject of investigation by the nuclear electric quadrupole method. The  $Li^+$  and  $Al^{+3}$  ions of spodumene were studied by Volkoff, Petch and Smellie<sup>16</sup> and by Petch, Cranna and Volkoff<sup>17</sup>, respectively. Their data can be used in the interpretation of the orthorhombic parameters  $b_2^0$  and  $b_2^2$  of the spin Hamiltonian.

The present work involves the EPR of  $Fe^{+3}$  and  $Mn^{+2}$  ions which occur as impurities in natural crystals of spodumene,

$\text{LiAl}(\text{SiO}_3)_2$ , and also in the kunzite and hiddenite varieties of spodumene. All of these crystals contain  $\text{Fe}^{+3}$  and  $\text{Mn}^{+2}$  ion impurities in varying proportions. The spodumene crystals are colorless, the kunzite crystals are pink, and the hiddenite crystals are green.

The iron spectrum was analyzed in detail in a sample of spodumene which contained a relatively small amount of manganese so as not to mask the iron spectrum. The results obtained here have been published by Manoogian et al.<sup>18</sup>. The Kunzite crystals contained mostly  $\text{Mn}^{+2}$  impurities with only a trace of  $\text{Fe}^{+3}$ , and so the manganese spectrum was analyzed in detail in these crystals. The hiddenite crystals contained mostly  $\text{Fe}^{+3}$  impurities with only a very small amount of  $\text{Mn}^{+2}$ . The spectra of iron and manganese in hiddenite were similar to those in the colorless spodumene and in the kunzite crystals, and so were not analyzed in detail here.

The EPR of  $\text{Fe}^{+3}$  in spodumene was studied at k-band frequencies (24 kmc) because the large zero-field splitting due to the crystalline electric field causes the transitions at x-band frequencies (9 kmc) to fall at the crossing points of the energy levels, while those at k-band fall in the linear regions. The x-band results for  $\text{Fe}^{+3}$  were first obtained by Carswell<sup>19</sup>. He was unable to analyze the results satisfactorily because of the complexity of the spectrum. The spectrum of  $\text{Mn}^{+2}$  was analyzed at k-band frequencies but was subsequently shown that it could equally well have been done at x-band. This is because the crystalline electric field of manganese

in spodumene is considerably smaller than that of iron.

A single reading was taken for each of the two ions at liquid helium temperature ( $4.2^{\circ}\text{K}$ ), and at x-band, in order to determine the order of the energy levels in the  ${}^6\text{S}_{5/2}$  state; that is, to determine the sign of  $b_2^0$  in the spin Hamiltonian.

The crystals were also heat-treated in order to determine if the paramagnetic resonance spectra would change after the crystal was heated to a sufficiently high temperature and then quickly cooled. This is important in the case of manganese because in all the three varieties of spodumene studied there are four complexes due to  $\text{Mn}^{+2}$  instead of one as would be expected by crystal symmetry when this ion substitutes into an available cation site. The principal axes of the four complexes are displaced only a few degrees from each other. Upon heat-treatment, the spectral lines due to the four  $\text{Mn}^{+2}$  complexes gradually decreased their intensities while spectral lines due to  $\text{Mn}^{+2}$  in a single complex formed and increased their intensities with increasing temperature. Moreover, with the restoration of the single manganese spectrum, it was observed that the pink color of the kunzite crystal disappeared and the crystal became colorless. No color change was observed in the other two varieties of spodumene.

The EPR spectrum of  $\text{Fe}^{+3}$  was also investigated in the heat-treated samples of spodumene and hiddenite. It was found that the line widths of the iron lines increased measurably.

The spectra of the iron and manganese ions were matched to an appropriate spin Hamiltonian for S-state ions in crys-

talline electric fields of orthorhombic symmetry. Using the values of the constants found for the Hamiltonian, and with the aid of a 1620 computer, it was possible to plot the energy levels as a function of the externally applied magnetic field.

## II

### CRYSTALLOGRAPHY

The structure of spodumene,  $\text{LiAl}(\text{SiO}_3)_2$ , has been described by Wyckoff<sup>20</sup>. It is a monoclinic pyroxene with diopside structure. The space group is given in the Schoenflies notation by  $C_{2h}^6$ , in the International notation of 1935 by  $C_{2/c}$ , and in the 1952 International notation by  $B_{2/b}$ . The first notation indicates a two-fold rotation axis and a horizontal plane of symmetry perpendicular to this axis. The index 6 means that it is the sixth available monoclinic space group, as listed in conventional tables. The large C in the second notation indicates that the crystal is monoclinic; the 2 indicates that there is a two-fold rotation axis, and the small c indicates the presence of a glide plane in the direction of the c-axis with magnitude of translation equal to half the axial length. The third notation gives the same information as the second except that the glide plane is given as being along the b-axis.

The pyroxenes have structures in which the silicon-oxygen tetrahedra,  $(\text{SiO}_3)_n$ , form simple, indefinitely long chains as shown in Figure 1. The silicon atom is at the center of a tetrahedron. In spodumene the chains are parallel to the crystallographic c-axis and are held together by  $\text{Li}^+$  and  $\text{Al}^{+3}$  ions. There are four formulae units per unit cell. The charges in

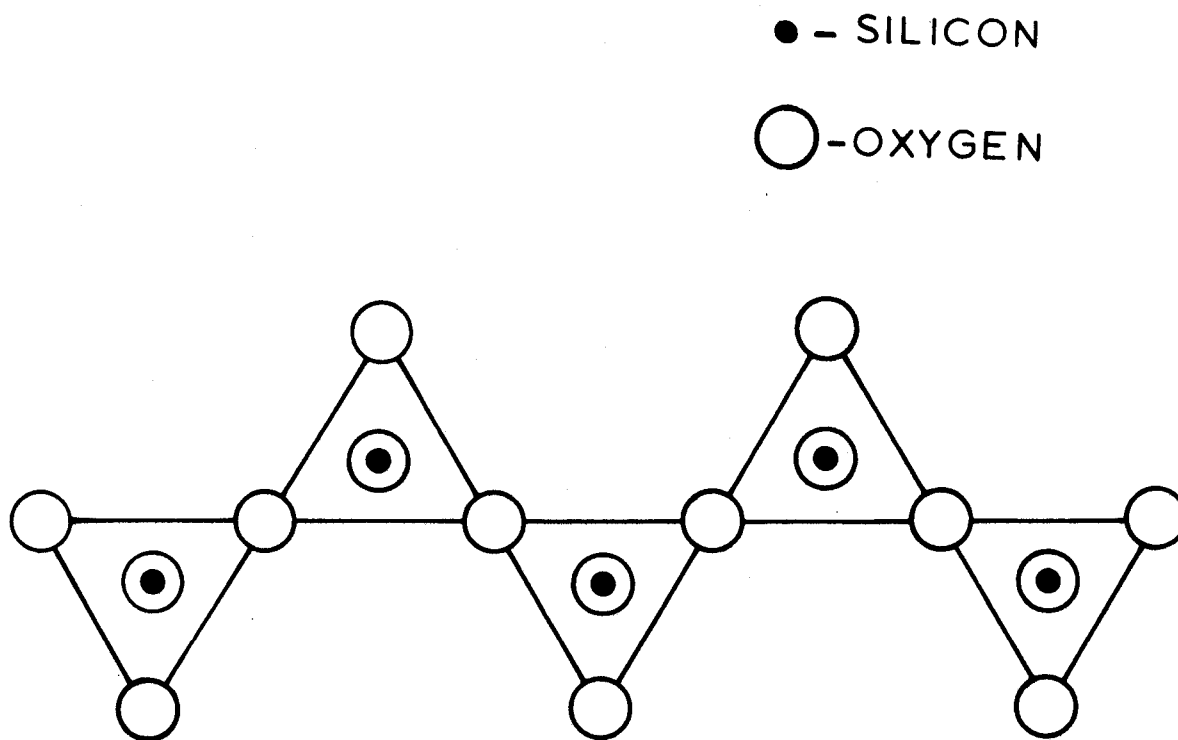


Fig. 1. Pyroxene structure,  $(SiO_3)_n$ . The silicon ion is at the center of a tetrahedron of oxygen ions.

a formula unit are  $\text{Li}^+\text{Al}^{+3}(\text{Si}^{+4}\text{O}_3^{-2})_2$ . The available cation sites for the substitution of  $\text{Fe}^{+3}$  and  $\text{Mn}^{+2}$  impurities in spodumene are those of  $\text{Li}^+$  and  $\text{Al}^{+3}$ . Table I gives some characteristics of the ions in spodumene.

TABLE I Characteristics Of Ions In Spodumene

Atom	Atomic Number	Ions Formed	Number of Electrons In Ion	Ground Config. Of Ion	Ionic Rad. In Å <sup>21</sup>
Li	3	$\text{Li}^+$	2	$1s^2$	0.60
O	8	$\text{O}^{-2}$	10	$1s^2 2s^2 2p^6$	1.40
Al	13	$\text{Al}^{+3}$	10	$1s^2 2s^2 2p^6$	0.50
Si	14	$\text{Si}^{+4}$	10	$1s^2 2s^2 2p^6$	0.41
Mn	25	$\text{Mn}^{+2}$	23	$(A)^{18} 3d^5 *$	0.80
Fe	26	$\text{Fe}^{+3}$	23	$(A)^{18} 3d^5 *$	0.64

\*  $(A)^{18}$  indicates the argon core:  $1s^2 2s^2 2p^6 3s^2 3p^6$ .

From Table 1, one notes the rule that for an isoelectronic series (a series of ions with the same number of electrons) the size of the ion decreases with increase in atomic number. Table 2 lists the chief isotopes of iron and manganese with some of their characteristics.

The dimensions of the unit cell of spodumene are:  $a = 9.52\text{Å}$ ,  $b = 8.32\text{Å}$ ,  $c = 5.25\text{Å}$ , and  $\beta = 69^\circ 40'$ . Figure 2 shows the pro-

TABLE 2. The Chief Isotopes Of Iron And Manganese With Some Of Their Characteristics<sup>22</sup>

Isotope	% Abundance	Nuclear Spin I	Magnetic Mom. (nm)	Quad. Mom. $\times 10^{-24} \text{cm}^2$
$^{54}\text{Fe}$	5.9	0	0	0
$^{56}\text{Fe}$	91.6	0	0	0
$^{57}\text{Fe}$	2.2	1/2	+0.05	0
$^{58}\text{Fe}$	0.33	0	0	0
$^{55}\text{Mn}$	100	5/2	+3.4681	+0.5

jection of a unit cell in the (010) plane. Figure 3 shows the polyhedron of oxygen ions surrounding the  $\text{Al}^{+3}$  and  $\text{Li}^{+}$  sites. There are four  $\text{Al}^{+3}$  and  $\text{Li}^{+}$  sites per unit cell and each has a twofold rotation axis passing through it parallel to the b-axis. The c-axis is readily identified because of prominent cleavage planes in the [001] direction. The b-axis, which is perpendicular to the c-axis, is along the bisector of the  $94^{\circ}$  angle between two cleavage planes. The a-axis is also perpendicular to the b-axis and makes an angle of  $69^{\circ}40'$  with the c-axis. Since the  $94^{\circ}$  angle is too close to  $90^{\circ}$ , and because the cleavage planes are not smooth, it was found desirable to identify the lattice parameters by means of x-ray analysis.

The c-axis is found quite easily by means of the rotation back-reflection x-ray method. In this method the crystal is rotated about a direction near the c-axis and monochromatic x-

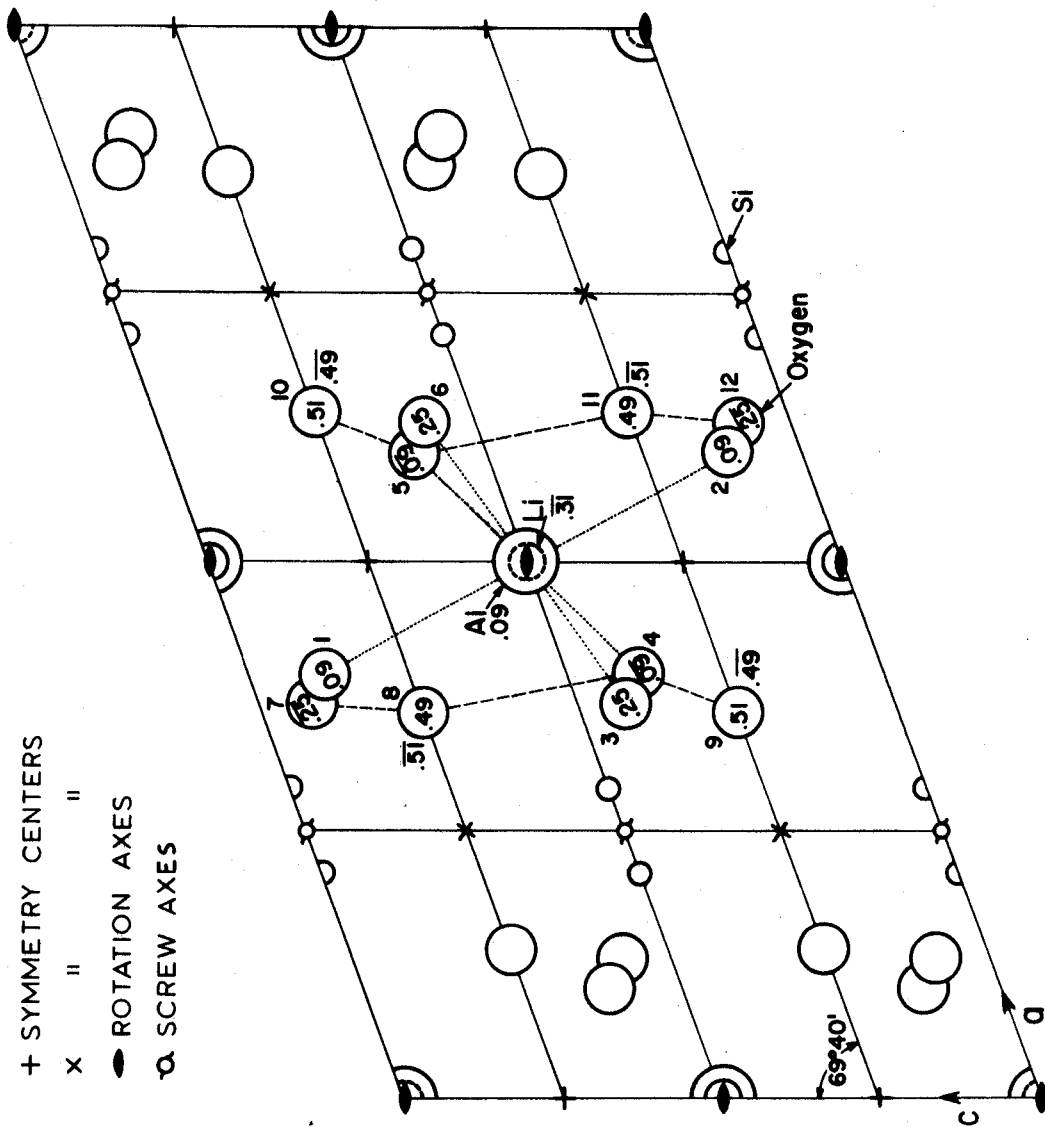
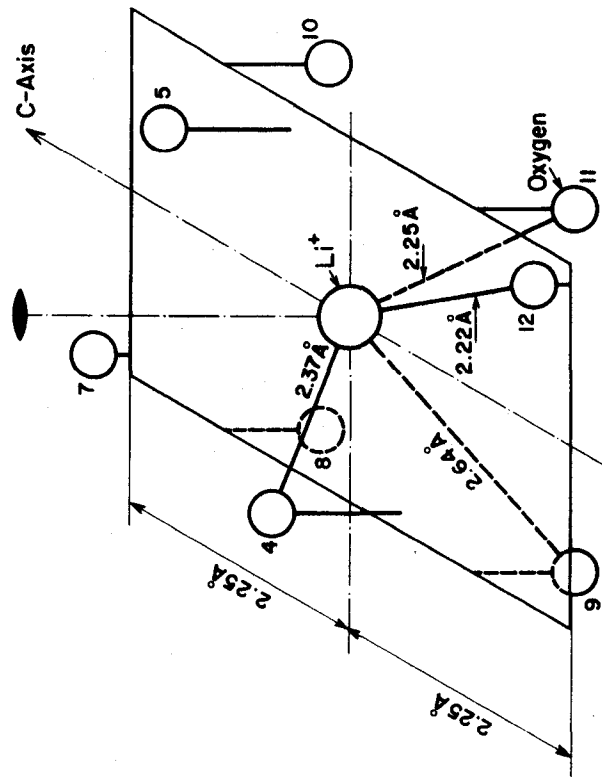
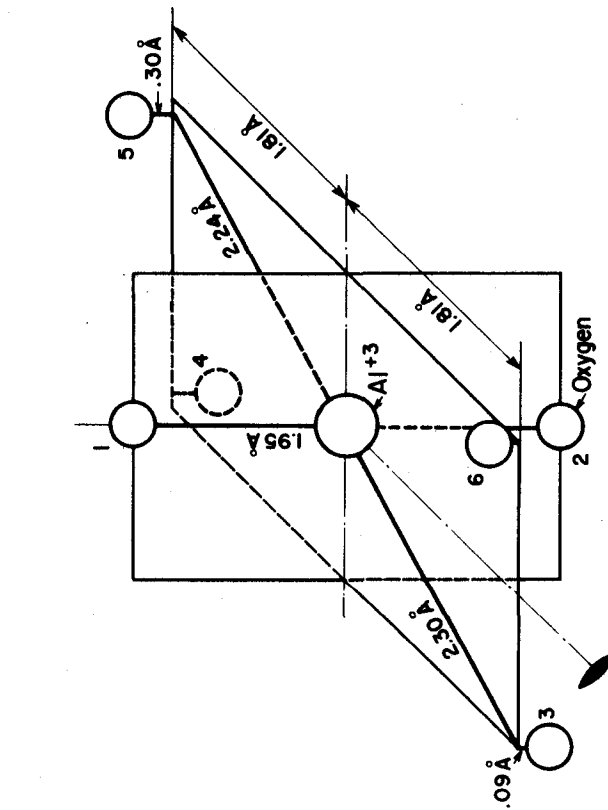


FIG. 2. The projection of a unit cell of spodumene in the (010) plane. The dotted and dashed lines connect the oxygen ions that are nearest neighbours to Al<sup>+3</sup> and Li<sup>+</sup> ions, respectively.



(a)  $\text{Al}^{+3}$  Site



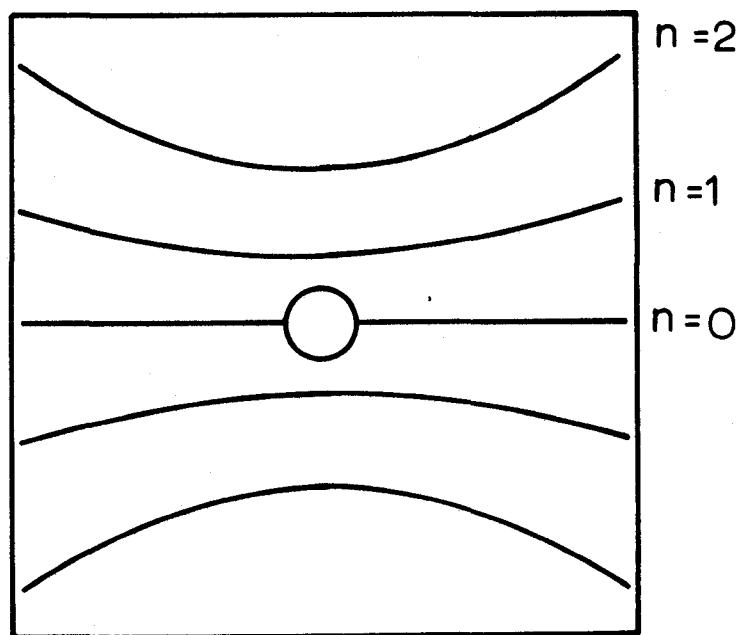
(b)  $\text{Li}^{+}$  Site

Fig. 3. Diagrams showing the oxygen ions surrounding (a)  $\text{Al}^{+3}$  and (b)  $\text{Li}^{+}$  ions in spodumene.

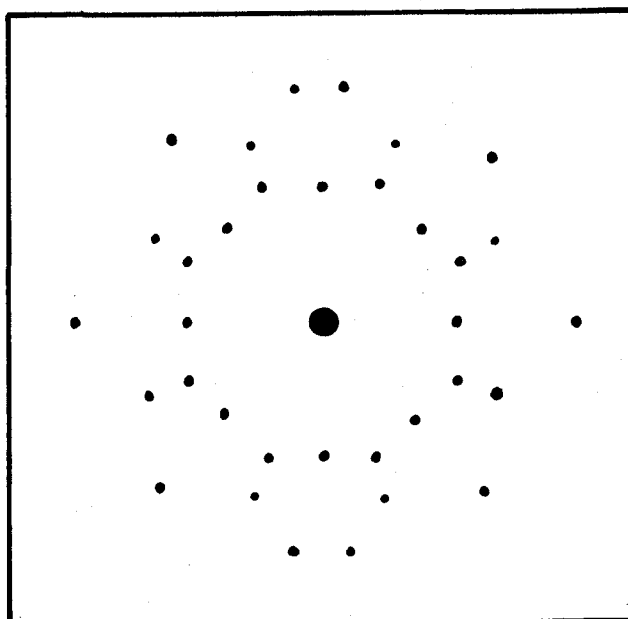
rays from a copper target and nickel filter strike the crystal almost perpendicular to the rotating axis. After alignment, when the x-rays are perpendicular to the axis, one observes a photograph as shown in Figure 4(a). The b-axis is similarly found but requires more time because its direction cannot initially be judged to better than  $10^\circ$ . Since the a-direction is also perpendicular to the b-direction, and makes an angle of  $69^\circ 40'$  to the c-direction, its position is easily found by means of the stationary transmission Laue method. White x-ray radiation is used in this method and, upon alignment, one obtains a photograph as shown in Figure 4(b).

The lattice parameters can easily be calculated if one measures the distance  $r$  between the photographic plate and the crystal face, and the distance  $s$  between the  $n=0$  to  $n=1$ , for example, level of the photographic plate. Using the well known formulae for x-ray diffraction:  $\tan \alpha = r/s$  and  $n\lambda = b \cos \alpha$ , the lattice parameters can be found. Here,  $b$  is the lattice parameter, and for a copper target with nickel filter  $\lambda = 1.539\text{\AA}$ . The parameters were calculated to be  $c = 5.12\text{\AA}$  and  $b = 8.16\text{\AA}$  compared to the correct values  $c = 5.25\text{\AA}$  and  $b = 8.32\text{\AA}$ . The a-parameter was not measured beyond confirming its position.

The spodumene sample used for studying the  $\text{Fe}^{+3}$  ion had dimensions of 4mm x 4mm x 7mm, the long dimension being along the c-axis. It was analyzed for impurity content by the National Research Council, in Ottawa, Ontario, with the following results: 0.2%  $\text{Fe}^{+3}$  and 0.05%  $\text{Mn}^{+2}$ , by weight. The kunzite and hiddenite samples had dimensions of 2mm x 2mm x 4mm. They were



(a)



(b)

Fig. 4. X-ray photographs. (a) shows a back-reflection x-ray photograph with x-rays lined perpendicular to a crystallographic axis. (b) shows a transmission Laue photograph with x-rays lined parallel to a crystallographic axis.

not analyzed for impurity content.

### III

#### THEORY

##### A. Crystal Field Theory

The crystal field theory assumes that the paramagnetic ion resides in a crystalline electric field due to point charges or point dipoles lying wholly outside the paramagnetic ion. The interaction energy between the neighbouring charges and the paramagnetic ion is added to the Hamiltonian of the free ion in order to calculate the new energy states. The crystalline potential, or field, has the symmetry of the neighbouring charges, and this symmetry fixes the properties of the ionic energy states.

The ground state for the S-state ions  $\text{Fe}^{+3}$  and  $\text{Mn}^{+2}$  is  ${}^6\text{S}_{5/2}$ , due to the  $3d^5$  electrons. In this state the ion has a resultant orbital angular momentum given by  $L=0$  and a resultant spin given by  $S=5/2$ . For a cubic crystalline electric field, Bethe<sup>23</sup> has shown by group theoretical methods that the six-fold degenerate  ${}^6\text{S}_{5/2}$  state is split into a quartet and a doublet. In an orthorhombic crystalline electric field the  ${}^6\text{S}_{5/2}$  state splits into three Kramer's doublets, which are further split when a constant magnetic field is applied. Kramer's theorem states that a purely electrostatic field acting on a system of an odd number of electrons can never reduce the degeneracy below two. Wigner<sup>24</sup> has shown that this degeneracy is related

to the invariance of the system under time reversal. The theoretical considerations regarding Kramer's doublets do not indicate which doublet lies lowest. To obtain this information the paramagnetic resonance spectrum must be studied at liquid helium temperatures where the effect of spin populations of the levels is observable.

### B. Zeeman Interaction

The Zeeman interaction between the external magnetic field and a valence electron can be found using Russell-Saunders coupling. For the uncoupled case we know

$$\vec{\mu}_l = \frac{e}{2mc} \vec{P}_l, \text{ where } P_l = \hbar\sqrt{l(l+1)} = \hbar l, \text{ say, and}$$

$$\vec{\mu}_s = 2 \frac{e}{2mc} \vec{P}_s, \text{ where } P_s = \hbar\sqrt{s(s+1)} = \hbar s, \text{ say.}$$

Here,  $\vec{\mu}_l$  and  $\vec{\mu}_s$  are the orbital magnetic moment and spin magnetic moment of the electron in terms of the orbital angular momentum  $\vec{P}_l$  and spin angular momentum  $\vec{P}_s$ , respectively. Also,  $e$  is the charge of the electron,  $m$  is its mass, and  $c$  is the velocity of light. For the case of Russell-Saunders coupling we can, in general, write

$$\vec{\mu}_j = g \frac{e}{2mc} \vec{P}_j, \text{ where } P_j = \hbar\sqrt{j(j+1)} = \hbar j, \text{ say.}$$

The quantity  $g$  is called the spectroscopic splitting factor. If the electron spin were absolutely free and had no coupling to any orbital motion, the  $g$  - factor would be 2 (or 2.0023 with the relativistic correction). In practice it is found to differ slightly from this value. Since the magnitude of the

orbital part of the magnetic moment depends on the crystal field, its magnitude is usually different for different directions of H, and shows an angular variation which has the symmetry of the crystal field.

The interaction energy of the total magnetic moment  $\vec{\mu}_J$  for several unpaired electrons with the external magnetic field H is

$$\begin{aligned} \mathcal{H}_{\text{Zeeman}} &= \vec{\mu}_J \cdot \vec{H} \\ &= g \frac{e}{2mc} \vec{P}_J \cdot \vec{H} \\ &= g \frac{e}{2mc} \hbar \vec{J} \cdot \vec{H} \end{aligned} \quad (1)$$

The quantity  $\beta = e\hbar/2mc$  is the Bohr magneton and so equation (1) can be written as

$$\mathcal{H}_{\text{Zeeman}} = g\beta \vec{J} \cdot \vec{H} \quad (2)$$

### C. Hyperfine Structure

The divalent manganese ion is in an S ground state and consequently no hyperfine structure would be expected. The fact is that in manganese a very large hyperfine splitting is observed. Abragam and Pryce<sup>3</sup> explained this as arising from configurational interaction with unpaired s electron states. Such an interaction may mix in states of the type  $3s3d^n4s$  to the  $3d^n$  ground state. Only a relatively small admixture of such states would be necessary to account for the observed splitting.

The unpaired s electrons contribute to the hyperfine structure splitting through the Fermi contact term given by

$$H_{\text{H.F.}} = 2\gamma \beta \beta_N \sum_k \left( \frac{8\pi}{3} (r_k)^{-3} \vec{s}_k \cdot \vec{I} \right). \quad (3)$$

Here,  $\delta(r_k)$  is the Dirac  $\delta$ -function,  $\gamma$  is the nuclear gyro-magnetic ratio,  $\beta$  is the Bohr magneton, and  $\beta_N$  is the nuclear magneton. The quantity  $r_k$  is the distance between the nucleus and the  $k$ 'th unpaired  $s$  electron, and the summation is over the electrons.

In general there is another contribution to the hyperfine structure due to the dipole-dipole interaction between the nucleus and the orbital motion of the electrons. However, for  $S$ -state ions the matrix of this interaction term is traceless and so its effect will average out to zero.

The magnetic field at the nucleus due to the contact term quantizes the nuclear magnetic moment into  $2I+1$  different orientations causing a perturbation on the electronic system of the atom and splitting each of the five electronic energy levels into  $2I+1=6$  lines. The six lines are in general unequally spaced. The spacing can be predicted from perturbation theory which involves the second order approximation.

#### D. The Spin Hamiltonian

The Hamiltonian for a paramagnetic ion in a crystalline electric field is in general quite complicated. Pryce<sup>25</sup> and Abragam and Pryce<sup>3</sup> have developed a very useful method for carrying out the perturbation calculation, and have applied it especially to the iron group. This calculation is based on the fact that transitions between the lowest energy levels are observed in the phenomenon of paramagnetic resonance. If tran-

sitions between  $2S'+1$  levels are observed experimentally, then  $S'$  can be defined as the fictitious spin of the system. In some cases, e.g. in the  ${}^6S_{5/2}$  state, the fictitious spin is identical to the free ion spin. Abragam and Pryce transform the various terms in the original Hamiltonian into a form involving appropriate angular momentum operators  $L, S$  and  $J$ . The advantage of using a spin Hamiltonian is that the rather complicated behaviour of the lowest energy levels of the paramagnetic ion in a magnetic field can be described in a relatively simple way by specifying the effective spin, together with a small number of parameters which measure the magnitudes of the various terms in the Hamiltonian. One must then find a model of a crystal field which corresponds to the spin Hamiltonian and which will explain the observed parameters.

The interaction terms describing the paramagnetic resonance spectra of  $Fe^{+3}$  and  $Mn^{+2}$  ions in the spin Hamiltonian are as follows:

- (i) Zeeman interaction. The Zeeman term given by equation (2) can be written for the case of an orbital singlet as

$$\begin{aligned} \mathcal{H}_{\text{Zeeman}} &= \beta \mathbf{S} \cdot \mathbf{g} \cdot \mathbf{H} \\ &= \beta g_x S_x H_x + \beta g_y S_y H_y + \beta g_z S_z H_z . \end{aligned}$$

- (ii) Hyperfine interaction. Following Abragam and Pryce,<sup>3</sup> the hyperfine interaction given by equation (3) can be written as

$$\mathcal{H}_{\text{H.F.}} = \sum_{i,j} A_{ij} I_i S_j .$$

The  $A_{ij}$  principal axes are taken to be along the  $g$  tensor axes. For an orthorhombic crystalline electric field we can write

$$\mathcal{H}_{\text{H.F.}} = A I_z S_z + B I_y S_y + C I_x S_x .$$

(iii) Crystalline electric field interaction. The spin Hamiltonian for a crystalline electric field of orthorhombic symmetry is given by Vinokurov et al<sup>15</sup> as being

$$\mathcal{H}_{\text{C.F.}} = \frac{1}{3} b_2^0 O_2^0 + \frac{1}{3} b_2^2 O_2^2 + \frac{1}{60} b_4^0 O_4^0 + \frac{1}{60} b_4^2 O_4^2 + \frac{1}{60} b_4^4 O_4^4 .$$

The form of these operators are given by Orbach<sup>26</sup>:

$$O_2^0 = 3S_z^2 - S(S+1)$$

$$O_2^2 = \frac{1}{2} (S_+^2 + S_-^2)$$

$$O_4^0 = 35S_z^2 - [30S(S+1) - 25]S_z^2 - 6S(S+1) + 3S^2(S+1)^2$$

$$O_4^2 = \frac{1}{4} \left\{ [7S_z^2 - S(S+1) - 5] (S_+^2 + S_-^2) + (S_+^2 + S_-^2) [7S_z^2 - S(S+1) - 5] \right\}$$

$$O_4^4 = \frac{1}{2} [S_+^4 + S_-^4]$$

where,

$$S_+ = S_x + iS_y$$

$$S_- = S_x - iS_y .$$

The matrix elements for these operators in various manifolds are given by Stevens<sup>27</sup>, and by Jones, Baker and Pope<sup>28</sup>, and by Low<sup>29</sup>.

The matrix elements of  $O_2^0$  and  $O_4^0$  are diagonal while those of  $O_2^2$ ,  $O_4^2$  and  $O_4^4$  are off-diagonal. Their values in the  $S = 5/2$  manifold are:

$$\begin{aligned}
0_2^0: & \quad (+1/2 \mid 0_2^0 \mid +1/2) = -8 \\
& \quad (+3/2 \mid 0_2^0 \mid +3/2) = -2 \\
& \quad (+5/2 \mid 0_2^0 \mid +5/2) = 10 \\
0_2^2: & \quad (+3/2 \mid 0_2^2 \mid +1/2) = 3\sqrt{2} \\
& \quad (+5/2 \mid 0_2^2 \mid +1/2) = \sqrt{10} \\
0_4^0: & \quad (+1/2 \mid 0_4^0 \mid +1/2) = 120 \\
& \quad (+3/2 \mid 0_4^0 \mid +3/2) = -180 \\
& \quad (+5/2 \mid 0_4^0 \mid +5/2) = 60 \\
0_4^2: & \quad (+3/2 \mid 0_4^2 \mid +1/2) = -15\sqrt{2} \\
& \quad (+5/2 \mid 0_4^2 \mid +1/2) = 9\sqrt{10} \\
0_4^4: & \quad (+5/2 \mid 0_4^4 \mid +3/2) = 12\sqrt{5}
\end{aligned}$$

#### E. EPR Transitions For Fe<sup>3+</sup> In Spodumene

The combined spin Hamiltonian for the Zeeman and crystal field interaction is

$$\begin{aligned}
\mathcal{H} = & \beta g_x S_x H_x + \beta g_y S_y H_y + \beta g_z S_z H_z \\
& + \frac{1}{3} b_2^0 O_2^0 + \frac{1}{3} b_2^2 O_2^2 + \frac{1}{60} b_4^0 O_4^0 + \frac{1}{60} b_4^2 O_4^2 + \frac{1}{60} b_4^4 O_4^4. \quad (4)
\end{aligned}$$

For the magnetic field H along the z magnetic axis, the matrix of equation (4) in the S=5/2 manifold is given in Table 3. It is noted that the 6x6 matrix can be written as two 3x3 matrices. When the Zeeman interaction is larger than the crystal field interaction the above matrix can be diagonalized using ordinary perturbation theory. The allowed EPR transition have the se-

TABLE 3. Matrix Of The Spin Hamiltonian (eq.(4)) In The S=5/2 Manifold.

	$+\frac{5}{2}$	$+\frac{1}{2}$	$+\frac{3}{2}$
$+\frac{5}{2}$	$+\frac{5}{2} g_z \beta H_z + \frac{10b_2^0}{3} + b_4^0$	$\frac{\sqrt{10}}{3} b_2^2 + \frac{3\sqrt{10}}{20} b_4^2$	$\frac{\sqrt{5}}{5} b_4^4$
$+\frac{1}{2}$	$\frac{\sqrt{10}}{3} b_2^2 + \frac{3\sqrt{10}}{20} b_4^2$	$+\frac{1}{2} g_z \beta H_z - \frac{8}{3} b_2^0 + 2b_4^0$	$\sqrt{2} b_2^2 - \frac{\sqrt{2}}{4} b_4^2$
$+\frac{3}{2}$	$\frac{\sqrt{5}}{5} b_4^4$	$\sqrt{2} b_2^2 - \frac{\sqrt{2}}{4} b_4^2$	$+\frac{3}{2} g_z \beta H_z - \frac{2}{3} b_2^0 - 3b_4^0$

selection rule  $\Delta M_S = \pm 1$ . In order to carry out an analysis of the  $Fe^{+3}$  spectrum the matrix was diagonalized to an approximation that included third-order perturbation terms. The transitions for the Z-direction are given by the following equations:

$$\begin{aligned}
 H_{5,1} &= H_0 + 4b_2^0 + 4b_4^0 + \frac{2b_2^0 A}{H_{5,1} - (b_2^0)^2} \\
 (+5/2 \rightarrow +3/2) & \\
 & - \frac{B}{H_{5,1} + 3b_2^0} + \frac{C}{H_{5,1} + b_2^0} + \frac{b_4^0 B}{2(3b_2^0 + H_{5,1})^2} + \frac{5b_4^0 C}{(2b_2^0 + H_{5,1})^2} \\
 & + \sqrt{ABC} \left[ \frac{1}{(b_2^0)^2 - H_{5,1}} + \frac{1}{(b_2^0 + H_{5,1})(3b_2^0 + H_{5,1})} \right]. \quad (5)
 \end{aligned}$$

147498

UNIVERSITY OF WINDSOR LIBRARY

$$\begin{aligned}
H_{4,2}^{+3/2 \rightarrow +1/2} &= H_0 + 2b_2^0 + 5b_4^0 - \frac{A}{H_{4,2} + b_2^0} - \frac{B}{H_{4,2} + 3b_2^0} \\
&+ \frac{2b_2^0 c}{H_{4,2} - (b_2^0)^2} + \frac{5b_4^0 c H_{4,2}^2}{(b_2^0)^2 - H_{4,2}^2} + \frac{b_4^0 B}{2(3b_2^0 + H_{4,2})^2} \\
&+ \frac{2\sqrt{ABC}}{(b_2^0 + H_{4,2})(3b_2^0 + H_{4,2})} + \frac{\sqrt{ABC}}{(b_2^0)^2 - H_{4,2}^2}, \quad (6)
\end{aligned}$$

$$\begin{aligned}
H_{4,2}^{1/2 \rightarrow -1/2} &= H_0 + \frac{2BH_3}{H_3 - (3b_2^0)^2} - \frac{2CH_3}{H_3 - (b_2^0)^2} + \frac{10b_4^0 b_2^0 c H_3}{((b_2^0)^2 - H_3)^2} \\
&- \frac{6b_2^0 b_4^0 B H_3}{((3b_2^0)^2 - H_3)^2} - \frac{8b_2^0 \sqrt{ABCH_3}}{((b_2^0)^2 - H_3)((3b_2^0)^2 - H_3)}, \quad (7)
\end{aligned}$$

where

$$A = \frac{1}{20} (b_4^0)^2, \quad B = 5 \left( \frac{b_2^0}{3} + \frac{3b_4^0}{20} \right)^2, \quad C = \left( b_2^0 - \frac{b_4^0}{4} \right)^2, \quad H_0 = \frac{h\nu}{\epsilon\beta}$$

and the  $b_n^m$  coefficients are in gauss. Equations 5-7 can be applied to the other two axes by substituting Vinokurov's<sup>15</sup> equivalents in place of  $b_n^m$ , which are listed in Table 4.

TABLE 4. Relationship Between The Parameters Of The Spin Hamiltonian For Different Orientations Of The Magnetic Field H.

H    Z	H    X	H    Y
$b_2^0$	$-\frac{1}{2} (b_2^0 - b_2^2)$	$-\frac{1}{2} (b_2^0 + b_2^2)$
$b_2^2$	$\frac{1}{2} (3b_2^0 + b_2^2)$	$\frac{1}{2} (3b_2^0 - b_2^2)$
$b_4^0$	$\frac{1}{8} (3b_4^0 - b_4^2 + b_4^4)$	$\frac{1}{8} (3b_4^0 + b_4^2 + b_4^4)$
$b_4^2$	$-\frac{1}{2} (5b_4^0 - b_4^2 - b_4^4)$	$-\frac{1}{2} (5b_4^0 + b_4^2 - b_4^4)$
$b_4^4$	$\frac{1}{8} (35b_4^0 + 7b_4^2 + b_4^4)$	$\frac{1}{8} (35b_4^0 - 7b_4^2 + b_4^4)$
A	B	C
B	A	A
C	C	B

F. EPR Transitions For  $Mn^{+2}$  In Kunzite

The combined spin Hamiltonian for Zeeman, crystal field and hyperfine interaction is

$$\begin{aligned}
 \mathcal{H} = & \beta g_x S_x H_x + \beta g_y S_y H_y + \beta g_z S_z H_z \\
 & + \frac{1}{3} b_2^0 O_2^0 + \frac{1}{3} b_2^2 O_2^2 + \frac{1}{60} b_4^0 O_4^0 + \frac{1}{60} b_4^2 O_4^2 + \frac{1}{60} b_4^4 O_4^4 \\
 & + A I_z S_z + B I_y S_y + C I_x S_x .
 \end{aligned}$$

The matrix elements of the hyperfine interaction term is added to the spin Hamiltonian matrix given in Table 3 and the whole matrix is then diagonalized to the second order of perturbation theory. Using the selection rules:  $\Delta M_S = \pm 1, \Delta m_I = 0$ , for allowed transitions, one finds the magnetic field positions of the hyperfine lines along the z-axis to be given by the following expressions:

$$\begin{aligned} H_{5,1}^{H_{5,1}} &= H_0 \mp 4b_2^0 \mp 4b_4^0 + \frac{4}{9} \left(\frac{b_2^2}{H_0}\right)^2 - \frac{1}{20} \left(\frac{b_4^2}{H_0}\right)^2 - \frac{b_2^2 b_4^2}{H_0} \\ (\pm 5/2, m \rightarrow \pm 3/2, m) & - Am - \frac{B^2 + C^2}{4H_0} [I(I+1) - m^2] \mp \frac{2BC}{H_0} m. \quad (8) \end{aligned}$$

$$\begin{aligned} H_{4,2}^{H_{4,2}} &= H_0 \mp 2b_2^0 \pm 5b_4^0 - \frac{5}{9} \left(\frac{b_2^2}{H_0}\right)^2 - \frac{9}{80} \left(\frac{b_4^2}{H_0}\right)^2 \\ (\pm 3/2, m \rightarrow \pm 1/2, m) & - \frac{1}{20} \frac{b_4^4}{H_0} - \frac{b_2^2 b_4^2}{2H_0} - Am \\ & - \frac{B^2 + C^2}{4H_0} [I(I+1) - m^2] \mp \frac{BC}{H_0} m. \quad (9) \end{aligned}$$

$$\begin{aligned} H_3^{H_3} &= H_0 - \frac{8}{9} \left(\frac{b_2^2}{H_0}\right)^2 + \frac{1}{10} \left(\frac{b_4^2}{H_0}\right)^2 + \frac{2b_2^2 b_4^2}{H_0} \\ (\frac{1}{2}, m \rightarrow -\frac{1}{2}, m) & - Am - \frac{B^2 + C^2}{4H_0} [I(I+1) - m^2]. \quad (10) \end{aligned}$$

The magnetic field positions for the EPR lines along the x- and

y-axes can be obtained using Vinokurov's equivalents.

The value of A is obtained by taking the average of all the hyperfine line spacings along the z-axis (25 of them). The second order terms will cancel out. Parameters B and C are obtained in a similar manner for the y- and x-axes. The signs of A, B and C can be obtained from the second order effects of the hyperfine splitting as done by Bleaney and Ingram<sup>1</sup>.

#### G. EPR Line Widths

In paramagnetic resonance the two major causes of line broadening are the interaction between the paramagnetic ions and the lattice, and the interaction between the ions themselves. These interactions have often been treated as giving relaxation effects, characterized by the spin-lattice relaxation time  $T$  and the spin-spin relaxation time.

(i) Spin-lattice interaction. The inverse of the spin-lattice relaxation time is a measure of the rate at which a spin exchanges a whole quantum of energy with the lattice. The theory of this is mainly due to Van Vleck<sup>30</sup>. The mechanism considered is one in which the thermal vibrations of the lattice give a fluctuating crystalline electric field. The spin-orbit coupling plays an essential role as the mechanism by which the spin of the paramagnetic ion feels the effect of the thermal vibrations. The development of the theory shows that the spin-lattice relaxation time  $T$  is strongly temperature dependent, becoming longer as the temperature is reduced. The theory also shows that  $T$  depends very markedly on the separa-

tion between the ground state and the first excited state. If this separation is large then  $T$  is long, and if the separation is small  $T$  is short.

(ii) Spin-spin interaction. The broadening due to this process arises from the interaction between the paramagnetic dipoles. There is no dependence on temperature due to this broadening, and the effect can only be reduced by separating the magnetic carriers. A picture of the broadening process can be obtained as follows. The magnetic moment of each ion is regarded as precessing about the external magnetic field  $H_0$ , and can be resolved into a component which is steady and directed along  $H_0$ , together with a rotating component perpendicular to  $H_0$ . The steady component sets up a steady field at neighbouring ion positions, and so the ions behave as if they were in a magnetic field which is slightly different from the external magnetic field. The rotating component sets up a rotating magnetic field. If this rotating field has the same frequency as the other paramagnetic ions, then there will be a couple acting on the steady component of the magnetic moment of the latter ion, tending to change its direction. The first process gives a broadening which is similar to that which arises from using an inhomogeneous magnetic field, and the second gives a resonance broadening because it tends to reduce the lifetime of an ion in a given state.

#### H. Comparison Of Spin Hamiltonian And Quadrupole Resonance Parameters.

One can correlate the paramagnetic resonance data with

quadrupole resonance data, if these are available. Following Bersohn<sup>31</sup> we can write

$$\begin{aligned}\phi'_{xx} &= \sum_j e_j \frac{3X_j^2 - a_j^2}{5a_j} \\ \phi'_{yy} &= \sum_j e_j \frac{3Y_j^2 - a_j^2}{5a_j} \\ \phi'_{zz} &= \sum_j e_j \frac{3Z_j^2 - a_j^2}{5a_j} \\ \phi'_{xx} - \phi'_{yy} &= \sum_j e_j \frac{3(X_j^2 - Y_j^2)}{5a_j} \\ \eta &= \frac{\phi'_{xx} - \phi'_{yy}}{\phi'_{zz}}\end{aligned}\quad (11)$$

where  $\eta$  is the asymmetry parameter. Therefore:

$$\eta \phi'_{zz} = \sum_j e_j \frac{3(X_j^2 - Y_j^2)}{5a_j}.$$

The interaction energy between a paramagnetic ion and the neighbouring ions in a crystal is given by

$$V_c = \sum_{i,j} e_i e_j \sum_k \frac{r_i^k}{a_j^{k+1}} \frac{4\pi}{2k+1} \sum_{m=-k}^k Y_k^m(X_i Y_i Z_i) Y_k^m(X_j Y_j Z_j)^* \quad (12)$$

where  $Y_k^m$  are normalized spherical harmonics with phases specified by Condon and Shortly<sup>32</sup>. A partial list of  $Y_k^m$  is given

by Ballhausen<sup>33</sup>. The index  $i$  above refers to the  $i$ th electron of the paramagnetic ion and  $j$  refers to a neighbouring ion whose charge is  $e_j$  and whose distance is  $a_j$  from the origin. In the orthorhombic case the important spherical harmonics are

$$(Y_2^0)^* = \sqrt{\frac{5}{4\pi}} \sqrt{\frac{1}{4}} \frac{3Z_j^2 - a_j^2}{a_j^2}$$

$$(Y_2^2)^* = \sqrt{\frac{5}{4\pi}} \sqrt{\frac{3}{8}} \left( \frac{X_j - iY_j}{a_j} \right)^2$$

$$(Y_2^{-2})^* = \sqrt{\frac{5}{4\pi}} \sqrt{\frac{3}{8}} \left( \frac{X_j + iY_j}{a_j} \right)^2$$

Substitute these into equation (12). The orthorhombic part of equation (4), ( $k=2$ ), is

$$\begin{aligned} V_{\text{ortho}} &= \sqrt{\frac{5}{4\pi}} \sum_{i,j} \frac{4\pi}{5} e_i e_j \frac{r_i^2}{a_j^3} \left\{ \sqrt{\frac{1}{4}} \frac{3Z_j^2 - a_j^2}{a_j^2} Y_2^0(X_i Y_i Z_i) \right. \\ &\quad \left. + \sqrt{\frac{3}{8}} \left( \frac{X_j - iY_j}{a_j} \right)^2 Y_2^2(X_i Y_i Z_i) + \sqrt{\frac{3}{8}} \left( \frac{X_j + iY_j}{a_j} \right)^2 Y_2^{-2}(X_i Y_i Z_i) \right\} \\ &= \sqrt{\frac{4\pi}{5}} \sum_{i,j} e_i r_i^2 \left\{ \frac{1}{2} e_j \frac{3Z_j^2 - a_j^2}{a_j^5} Y_2^0(X_i Y_i Z_i) \right. \\ &\quad \left. + \sqrt{\frac{3}{8}} e_j \left[ \left( \frac{X_j - iY_j}{a_j} \right)^2 Y_2^2(X_i Y_i Z_i) + \left( \frac{X_j + iY_j}{a_j} \right)^2 Y_2^{-2}(X_i Y_i Z_i) \right] \right\} \end{aligned} \quad (13)$$

When referred to the  $x$ ,  $y$  and  $z$  magnetic axes, equation (13)

becomes

$$V_{\text{ortho}} = \sqrt{\frac{4\pi}{5}} \sum_{i,j} r_i^2 e_i \left\{ \frac{1}{2} e_j \frac{(3Z_j - a_j^2)}{a_j^5} Y_2^0(i) \right. \\ \left. + \sqrt{\frac{3}{8}} e_j \frac{(X_j^2 - Y_j^2)}{a_j^5} \left[ Y_2^2(i) + Y_2^{-2}(i)^* \right] \right\}$$

The required spherical harmonics in terms of the index  $i$  are

$$Y_2^0(i) = \sqrt{\frac{5}{4\pi}} \sqrt{\frac{1}{4}} \frac{3Z_i^2 - r_i^2}{r_i^2}$$

$$Y_2^2(i) = \sqrt{\frac{5}{4\pi}} \sqrt{\frac{3}{8}} \frac{(X_i + iY_i)^2}{r_i^2}$$

$$Y_2^{-2}(i) = \sqrt{\frac{5}{4\pi}} \sqrt{\frac{3}{8}} \frac{(X_i - iY_i)^2}{r_i^2}$$

$$Y_2^2(i) + Y_2^{-2}(i)^* = \sqrt{\frac{5}{4\pi}} \sqrt{\frac{3}{8}} \left( \frac{(X_i + iY_i)^2}{r_i^2} + \frac{(X_i - iY_i)^2}{r_i^2} \right) \\ = 2 \sqrt{\frac{5}{4\pi}} \sqrt{\frac{3}{8}} \frac{(X_i^2 - Y_i^2)}{r_i^2} .$$

Hence , we have

$$V_{\text{ortho}} = \frac{1}{4} \sum_{i,j} e_i \left[ \frac{1}{2} e_j \frac{(3Z_j - a_j^2)}{a_j^5} (3Z_i^2 - r_i^2) \right. \\ \left. + \frac{3}{4} e_j \frac{(X_j^2 - Y_j^2)}{a_j^5} (X_i^2 - Y_i^2) \right]$$

$$= \frac{1}{4} e \left[ \phi'_{zz} (3z_i^2 - r_i^2) + \eta \phi'_{zz} (X_i^2 - Y_i^2) \right] \quad (14)$$

where,

$$\phi'_{zz} = \sum_j e_j \frac{3z_j^2 - a_j^2}{a_j^5}$$

$$\eta \phi'_{zz} = 3 \sum_j e_j \left( \frac{X_j^2 - Y_j^2}{a_j^5} \right)$$

$$e = \sum_i e_i .$$

Equation (13) can be put in terms of operator equivalents.

To do this we must put

$$\begin{aligned} X &\rightarrow S_x \\ Y &\rightarrow S_y \\ Z &\rightarrow S_z \\ r^2 &\rightarrow S(S+1) \end{aligned}$$

Hence,

$$V_{ortho} = e \alpha \langle r^2 \rangle \left\{ \frac{1}{4} \phi'_{zz} (3S_z^2 - S(S+1)) + \frac{1}{4} \eta \phi'_{zz} (S_x^2 - S_y^2) \right\}$$

This can be compared with the ordinary spin Hamiltonian given by

$$\mathcal{H} = \frac{1}{3} b_2^0 (3S_z^2 - S(S+1)) + \frac{1}{3} b_2^2 (S_x^2 - S_y^2)$$

Therefore

$$\frac{1}{3} b_2^0 = e \alpha \langle r^2 \rangle \frac{1}{4} \phi'_{zz}$$

$$\frac{1}{3} b_2^2 = e\alpha \langle r^2 \rangle \frac{1}{4} \eta \phi_{zz}'$$

or,

$$\frac{b_2^2}{b_2^0} = \eta .$$

## IV

### EQUIPMENT

#### A. K-Band Spectrometer

The k-band spectrometer operated at room temperature only. It was of balanced bridge design with the microwave frequency stabilized against the sample cavity. A block diagram of the system is shown in Figure 5. The klystron was a Varian type VA - 98E reflex klystron producing 30 milliwatts of power. The external magnetic field was produced by a 12 inch Varian electromagnet with rotating base, and it was stabilized by a fieldial (Varian) which kept the field value constant to within one gauss for several hours. It was possible to get a linear field sweep up to 20 kgauss.

A phase sensitive detection system was employed when recording signals on the strip-chart recorder, producing the derivative of the absorption pattern. In this case the magnetic field was modulated at 200 c/s. The signals could alternately be observed directly on an oscilloscope. In this case, the magnetic field was modulated at 60 c/s by means of a "Variac" and the EPR signals were detected at the microwave bridge, amplified by an audio amplifier, and fed to the vertical input of an oscilloscope. The horizontal input was connected to a 60 c/s source and phase shifter. Hence the absorption patterns of the EPR lines appeared on the oscilloscope. The method of

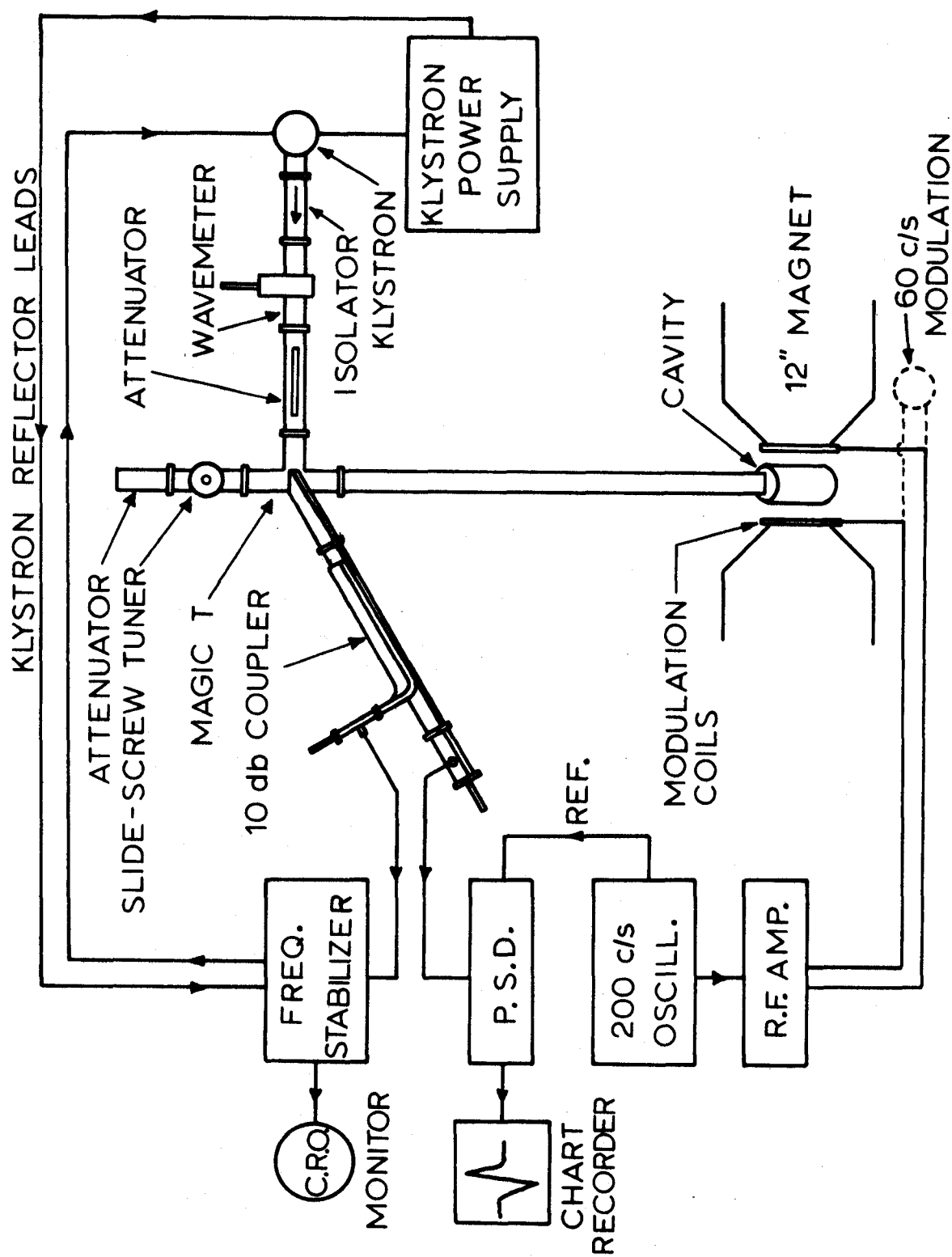


Fig. 5. Block diagram of k-band spectrometer used for EPR experiments at room temperature.

oscilloscope display allows one to observe the EPR signals when both the directions of the magnetic field and the crystal orientation are varied. This permits the direct and rapid observation of the angular variation of the EPR lines.

#### B. X-Band Spectrometer Used At Room Temperature

A block diagram of the x-band spectrometer used at room temperature is shown in Figure 6. The spectrometer was of a balanced bridge design with the microwave frequency stabilized against the sample cavity. The microwave generator was a Varian type VA - 203 klystron producing 30 milliwatts of power. A 7 inch Newport magnet was used with this spectrometer. A phase-sensitive detection system was employed when recording the EPR signals on a chart recorder. In this case, the magnetic field was modulated at 100 kc/s. This modulation frequency was applied to a single loop of copper wire inside the cavity (see Figure 10). The EPR signals obtained on the chart recorder were the derivatives of the absorption lines. For oscilloscope observation, an additional 60 c/s modulation frequency was applied to coils on the pole pieces. The EPR signal was fed from the microwave bridge to the phase-sensitive detector and then to the vertical input of an oscilloscope. The horizontal input was connected to a 60 c/s source and phase shifter. The signals on the oscilloscope showed the derivative pattern of the absorption lines. For oscilloscope observation the time constant on the phase-sensitive detector was 0.0003 seconds.

#### C. X-Band Spectrometer Used At Liquid Helium Temperatures

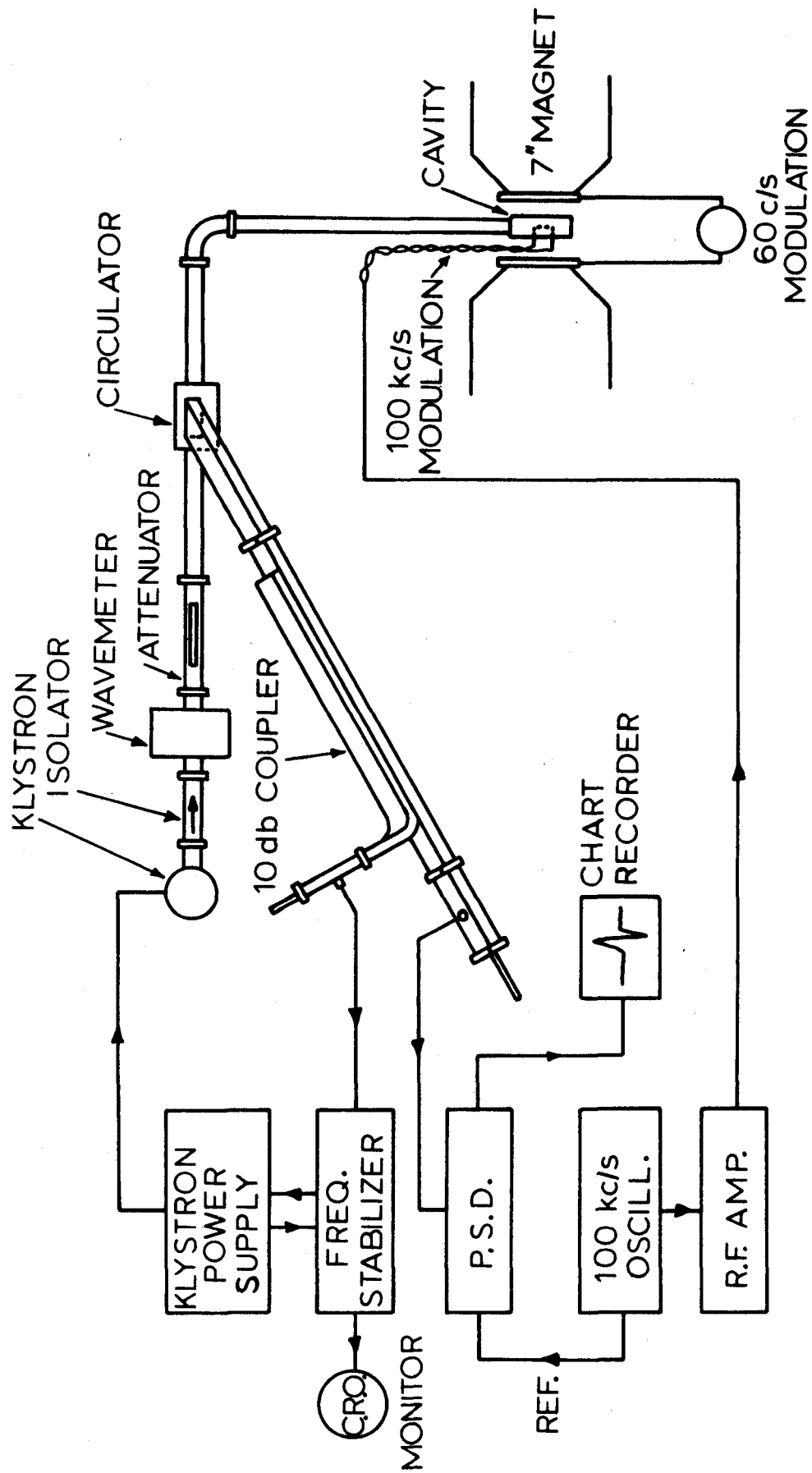


Fig. 6. Block diagram of x-band spectrometer used for EPR experiments at room temperature.

At liquid helium temperatures a superheterodyne spectrometer must be employed because of the low power levels necessary. This is because at liquid helium temperatures the spin lattice relaxation times of the ions in the crystals are longer than at room temperature and one must deal with small power levels so as not to saturate the EPR lines. A block diagram of the spectrometer is shown in Figure 7. The intermediate frequency was 30mc/s. Here again the signal klystron frequency was stabilized against the sample cavity. The local oscillator klystron was stabilized at  $\pm 30$  mc/s away from the signal klystron frequency. The magnetic field was again modulated at 100 kc/s for strip-chart recording and an additional 60 c/s was applied to the pole pieces for oscilloscope observation. A 12 inch magnet was used with this spectrometer.

A double dewar system was employed to hold the liquid helium. Liquid air was placed in the outer dewar and the inner dewar was evacuated to about 25 microns of mercury. The evaporation of helium was about  $1\frac{1}{2}$  inches per hour in the dewar. That is, if two liters of helium were used, one could work for about 7 hours.

#### D. K-Band Cavities

The two k-band cavities used are shown in Figures 8 and 9. With the cavity of Figure 8 one could orient the crystal by x-ray methods prior to conducting EPR measurements. In the x-ray work one fastens the goniometer (b), with attached crystal, to the special base (a) which in turn is connected to the x-ray equipment to find the crystallographic axes. The gonio-

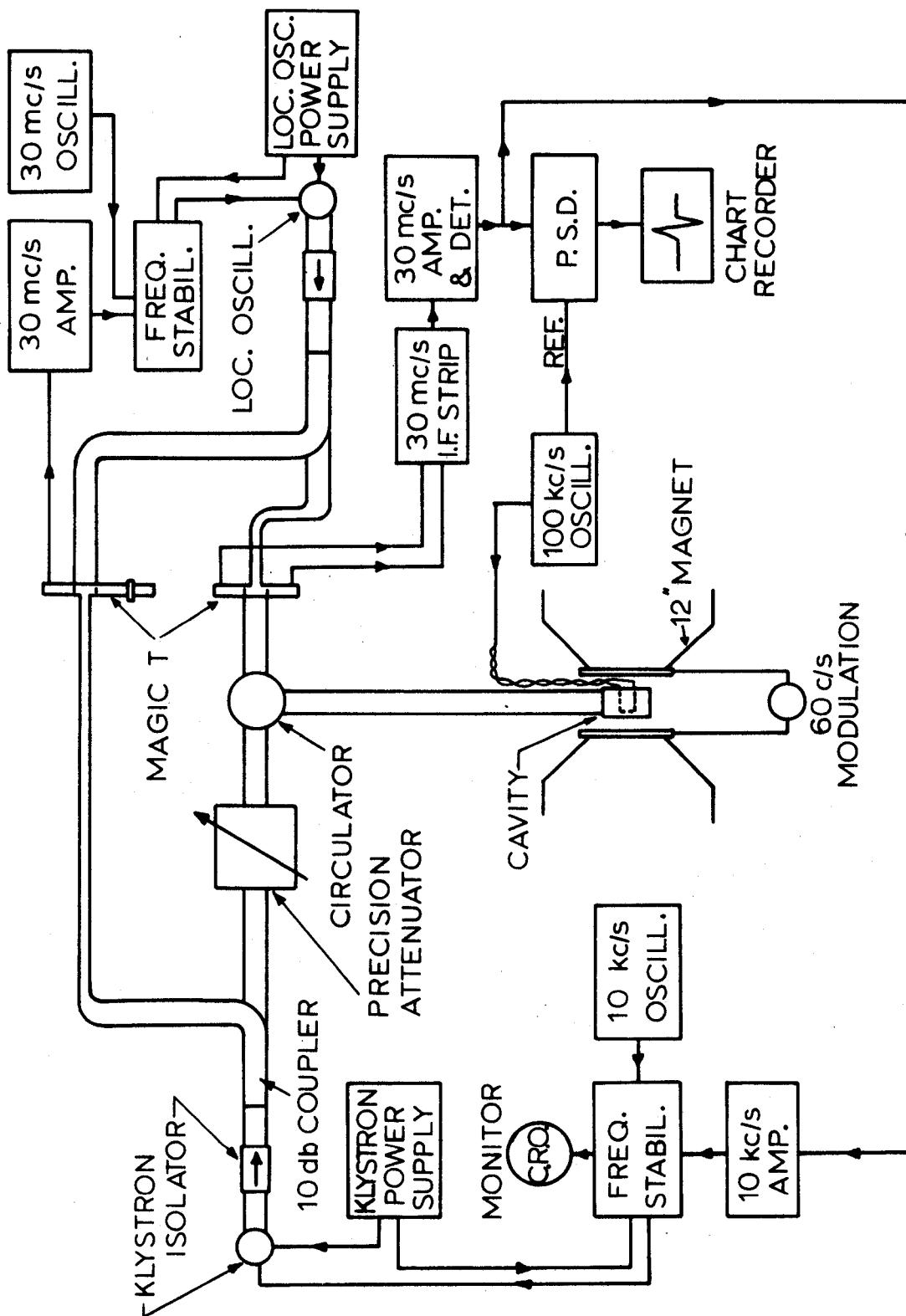


Fig. 7. Block diagram of x-band superheterodyne spectrometer used for EPR experiments at liquid helium temperatures.

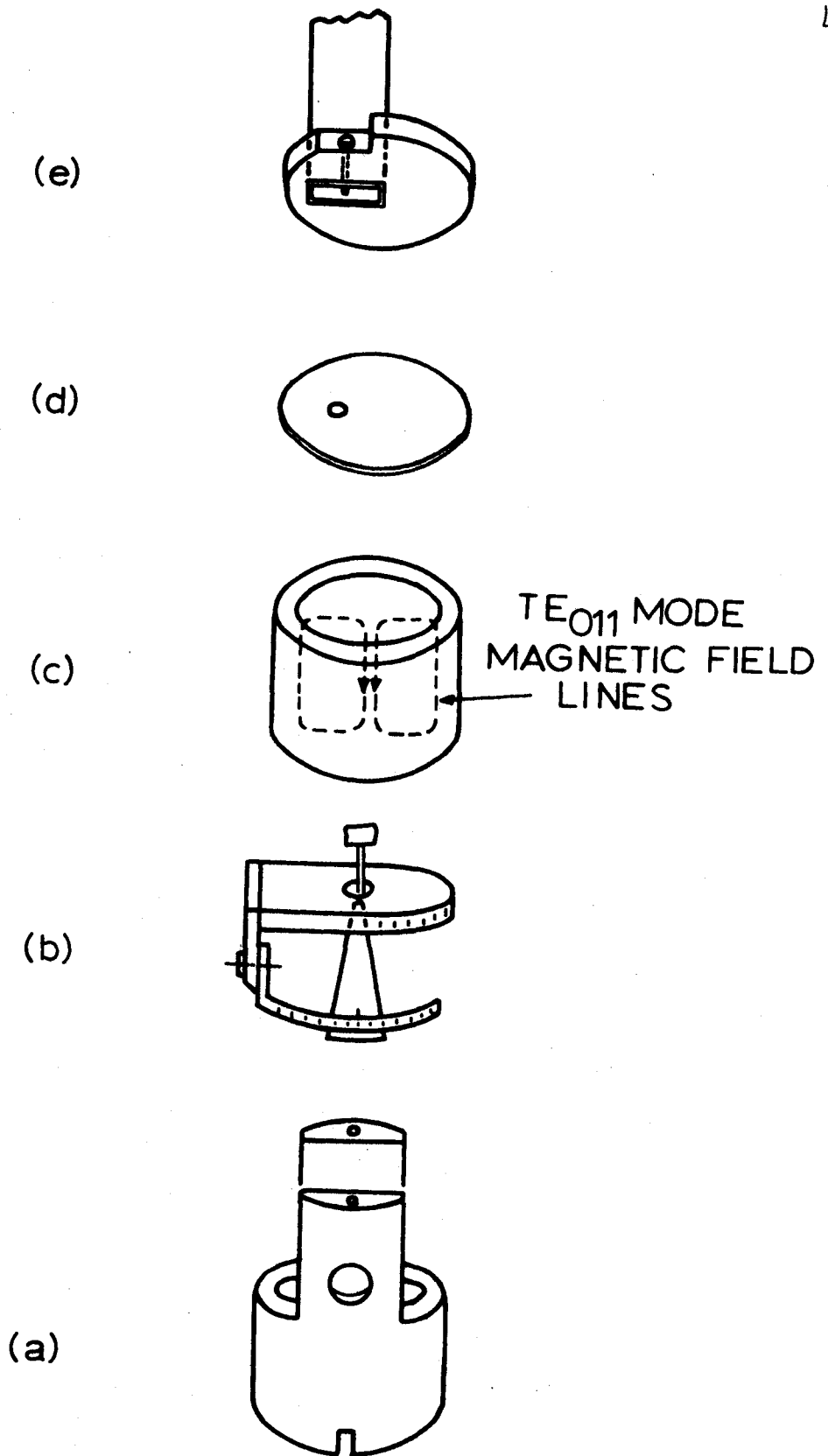


Fig. 8. K-band cavity system with vertical crystal mount.

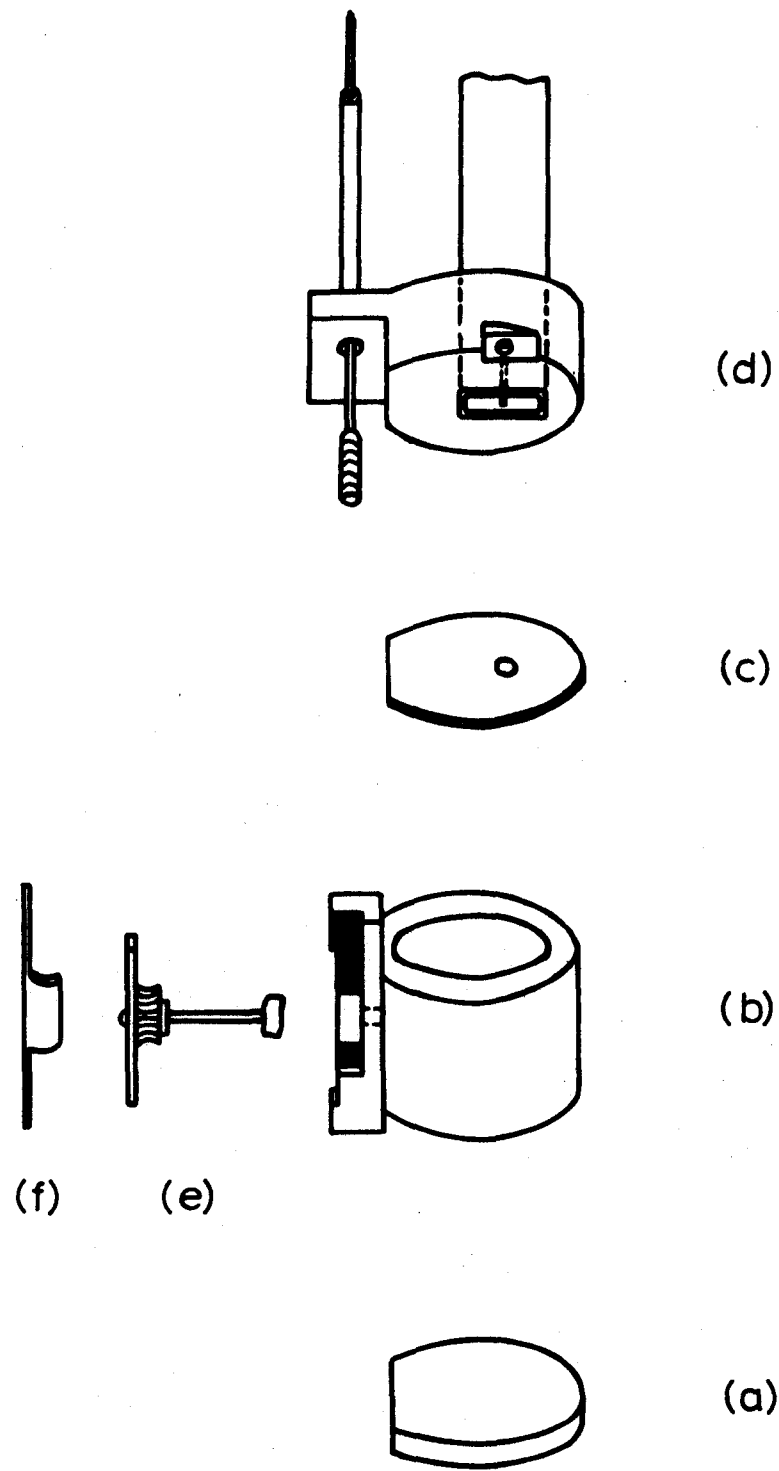


Fig. 9. K-band cavity system with horizontal crystal mount.

meter can also be connected to the bottom of the cavity (c) for EPR work. The goniometer was designed so that the crystal could be rotated independently in two perpendicular directions.

The cavity (c) was cylindrical in shape, operating in the  $TE_{011}$  mode. Its dimensions can be calculated from the formula<sup>34</sup>

$$\lambda = \frac{4}{\sqrt{\left(\frac{1}{h}\right)^2 + \frac{5.93}{a^2}},$$

where  $\lambda = 1.25$  cm,  $a$  is the inside radius of the cavity, and  $2h$  is the height. The optimum condition for best cavity operation occurs when  $a=h$ . This is calculated to be 0.656 inches. The cavity was constructed from rexolite plastic and lined with 0.001 inch thick commercial aluminum foil. The ends of the foil were joined by silver paint. The skin depth of aluminum at k-band frequencies can be found from the formula  $\delta = 2.9 \times 10^{-2} \sqrt{\rho \lambda}$ , where  $\rho$  is the resistivity of aluminum ( $2.8 \times 10^{-6}$  ohm - cm), and  $\lambda$  is the microwave wavelength in air (1.25 cm). One finds :  $\delta = 2.1 \times 10^{-5}$  inches. This figure is small enough when compared with the thickness of 0.001 inches of the commercial foil.

Besides the  $TE_{011}$  mode, there also exists a  $TM_{111}$  mode of identical frequency. The existence of the latter mode is undesirable since its presence lowers the overall Q of the cavity. The  $TM_{111}$  mode is suppressed to a considerable extent by

a break in the electrical connection at the ends of the cavity. The loaded Q of the cavity was about 1500.

Microwave power was fed into the cavity through a hole in the diaphragm(d). The diaphragm was made of bronze of thickness 0.005 inches. The hole size in the diaphragm was adjusted for each sample to give optimum spectrometer sensitivity. It was found that a nominal hole size was nearly the same size as the width of the waveguide. Matching was achieved by adjusting a screw placed near the coupling hole (e).

The cavity system of Figure 9 allowed the crystal to move about a horizontal axis by means of a worm gear arrangement. Part (a) shows the cavity bottom plate, (b) the aluminum foil-lined cavity with gear mount, (c) the diaphragm (d) the top plate with worm gear and impedance matching screw, (e) the crystal mount on the horizontal gear, and (f) shows a spring clamp used to keep the gears in mesh without slipping.

If one uses a magnetic field rotating about a vertical axis with the cavity system of Figure 9, then it is possible to obtain all the principal magnetic axes without reorienting the crystal. The positions of the principal axes can be plotted on a stereographic projection net, as done below. This arrangement is particularly useful if one has more than one magnetic complex in the crystal.

#### E. X-Band Cavity

The x-band cavity was rectangular and operated in the  $TE_{012}$  mode. A diagram of this system is shown in Figure 10. The sample is again mounted so that it can be rotated about

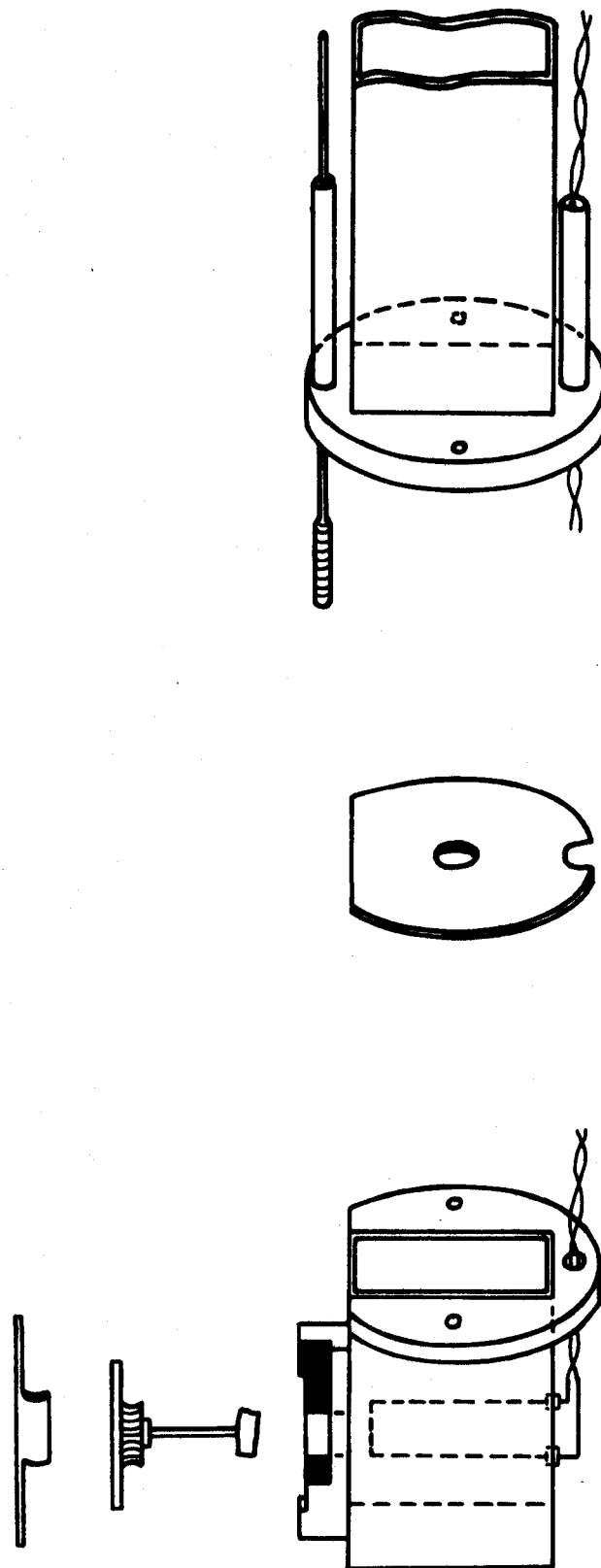


Fig. 10. X-band cavity system with horizontal crystal mount.

a horizontal axis. The 100 kc/s magnetic field modulation loop is provided by a single turn of copper wire placed at the center of the cavity. The end of the loop is bent aside in order to clear the crystal hole on the side of the cavity. The crystal mount and the gear system is similar to that shown in Figure 9.

#### F. Crystal Heating Equipment

Figure 11 shows the equipment used for heating and subsequent cooling of the crystals. The crystal to be heated under vacuum is placed on a quartz holder inside a quartz tube. The tube is connected to a pump system through a stopcock at the top end, and the bottom is sealed by an O-ring. With the stopcock open, the region around the crystal is continuously evacuated. The region around the crystal was surrounded by a furnace housed in a steel container and wrapped by aluminum foil to reduce heat loss due to radiation. Temperatures of 900° C could easily be reached. The temperature was determined by a chromel - alumel thermocouple.

The crystal could be cooled by shutting off the vacuum pumps and opening the system to the atmosphere. This causes the O-ring seal to break and the crystal with its holder to fall into the water bath. The crystal could also be slowly cooled under vacuum or in air if desired.

#### G. Magnetic Field Measurement

The magnetic field at which the EPR transitions occurred was measured by proton resonance. The source of protons was water with a small amount of copper sulphate added to it or,

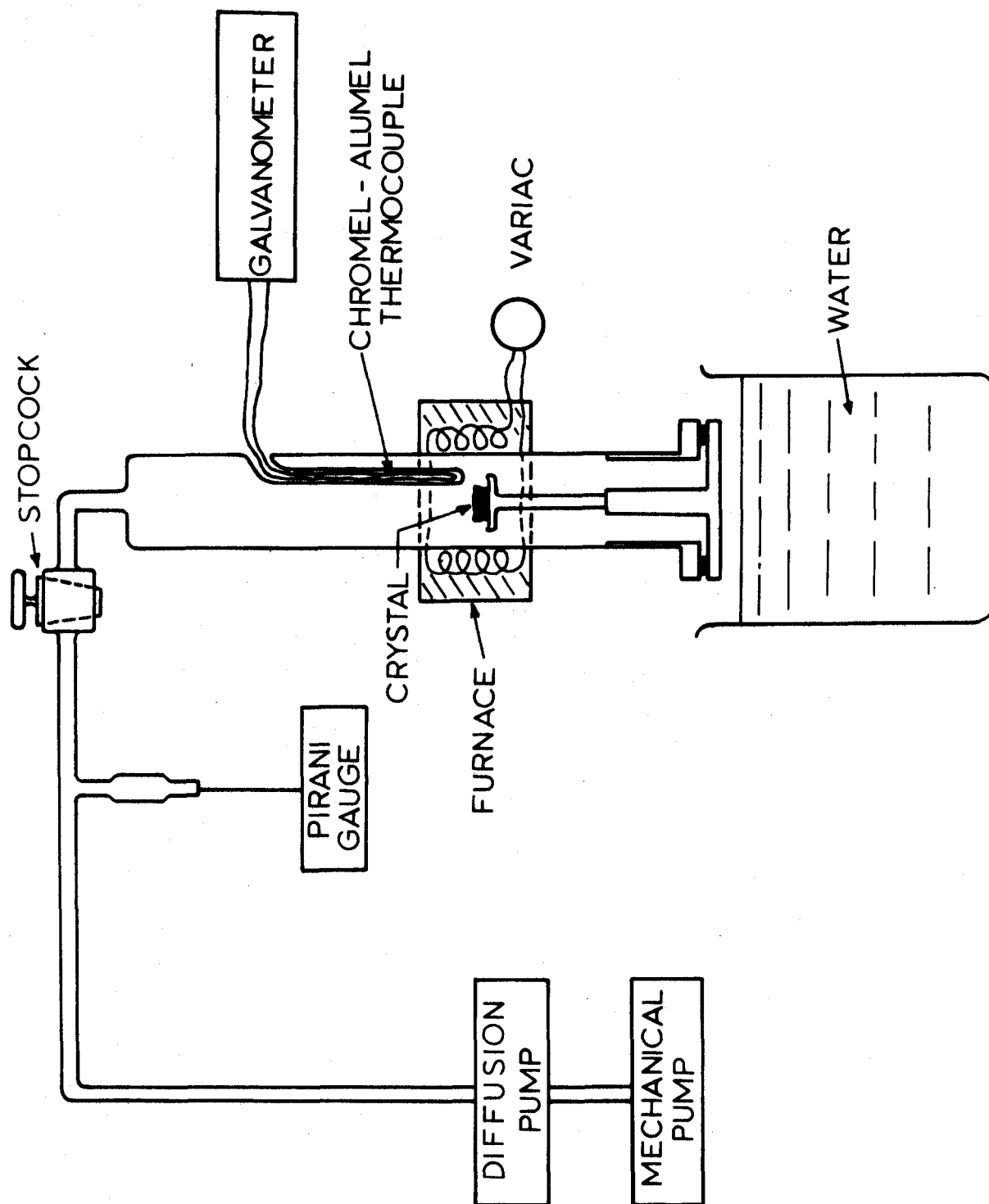


Fig. 11. Crystal heat-treatment apparatus.

alternately, paraffin oil. The proton resonance was observed on an oscilloscope. Here, the magnetic field was modulated at 60 c/s, and the horizontal input of the oscilloscope was connected to a 60 c/s source and phase shifter. To obtain a measurement, the frequency of the proton oscillator was varied until the proton resonance signal was observed on the oscilloscope. The frequency at which proton resonance occurred was measured with a Hewlett Packard No. 5253B frequency counter. Using the formula

$$H \text{ (kgauss)} = \frac{\nu \text{ (mc/s)}}{4.25759} ,$$

one obtains the strength of the magnetic field in kgauss. Here,  $\nu$  is the proton resonance frequency in mc/s, and the quantity 4.25759 is the frequency for proton resonance in a 1 kgauss magnetic field.

#### H. Microwave Frequency Measurement

The microwave frequency could be measured with sufficient accuracy by using a small amount of DPPH as a reference marker. The DPPH is placed on the crystal in the cavity and its single line is recorded with the EPR lines arising from the crystal. In principle, when making calculations, one needs only to know the magnetic field position of the DPPH line since its  $g$  value is known to be 2.0036. However, if desired, the microwave frequency can be found knowing the magnetic field of the DPPH resonance, using the formula

$$h\nu = g_d \beta H_d ,$$

The quantity  $h$  is Planck's constant ( $6.62517 \times 10^{-27}$  erg sec),  $\nu$  is the required microwave frequency,  $g_d$  is 2.0036 for DPPH,

$\beta$  is the Bohr magneton (  $0.92731 \times 10^{-21}$  erg / gauss ), and  
 $H_d$  is the resonant magnetic field of the DPPH.

## EXPERIMENTAL PROCEDURE AND RESULTS

A. Fe<sup>+3</sup> In Spodumene

The EPR spectrum of Fe<sup>+3</sup> was analyzed at room temperature and at k-band frequencies, using the spectrometer system of Figure 5, and the cavity system of Figure 8. Many samples of spodumene were investigated and all contained iron and manganese in varying proportions. The sample containing the least amount of manganese was selected. Figure 12 shows the trace of a spectrum obtained when the magnetic field was aligned along the z-axis of Fe<sup>+3</sup> in spodumene. In addition to the five iron lines there is a "forbidden" iron line, as well as others due to manganese.

(i) Determination of the magnetic axes. The directions of the magnetic axes of Fe<sup>+3</sup> with respect to the crystallographic axes were determined as follows. The crystal symmetry demands that one magnetic axis be along the [010] direction, and the remaining two in the (010) plane. This investigation located one axis in the (010) plane as being at 5° to the c-axis and 65° to the a-axis. We define the magnetic z-axis as the axis along which the spread of the five EPR lines is greatest, and the y-axis as the axis being in the plane normal to the z-axis and having the greatest spread of the five EPR lines in this plane. The remaining x-axis is thus fixed. It turned out that the y-axis was the one pointing along the

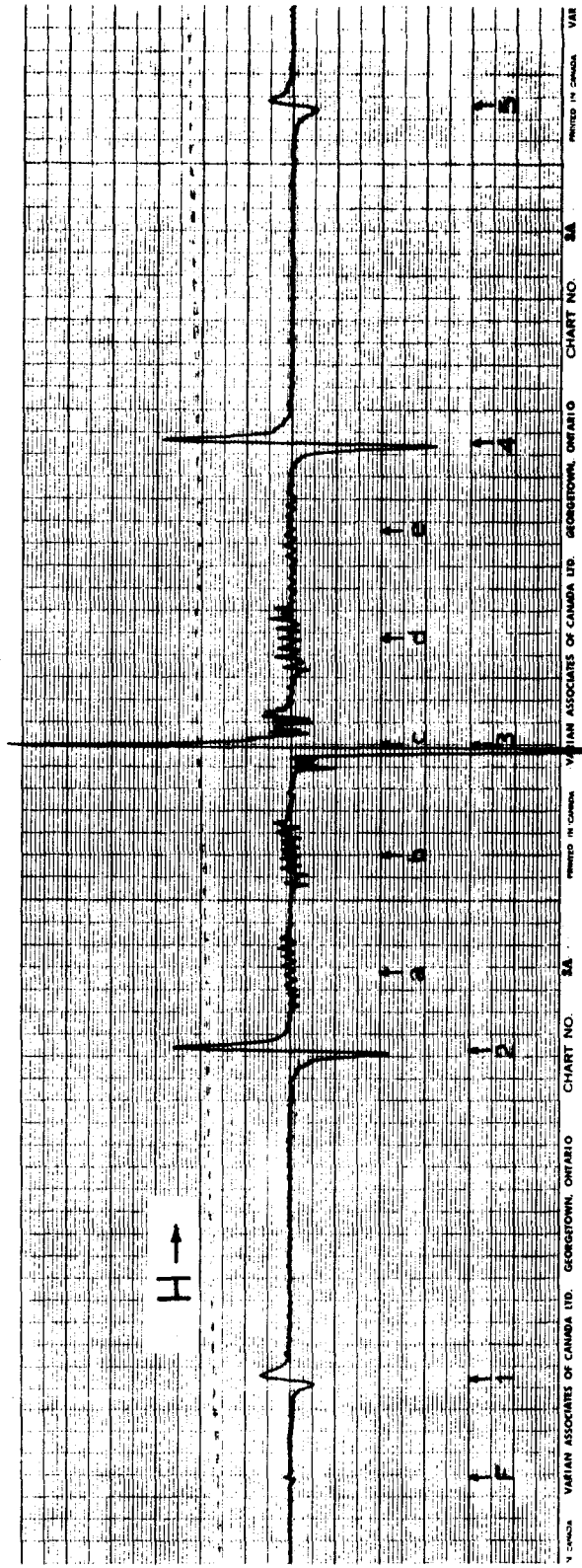


Fig. 12. The spectrum of  $Fe^{+3}$  ions in spodumene with the magnetic field along the z-axis. Numbers 1-5 indicate the five  $Fe^{+3}$  lines, a-e indicate five groups of lines due to  $Mn^{+2}$ , and F shows a forbidden line of iron. The DPPH line is 6 gauss greater than the central iron line.

[ 010 ] direction and the remaining z- and x-axes were positioned in the (010) plane, with the z-axis at  $5^\circ$  to the c-axis. Figure 13 and 14 show the variation of the five  $\text{Fe}^{+3}$  lines when the magnetic field was rotated in the planes perpendicular to the spectral x- and z-axes, respectively. The magnetic field values of each of the resonances along the three principal magnetic axes were measured by proton resonance and are listed in Table 5.

TABLE 5. Resonant Fields Of  $\text{Fe}^{+3}$  EPR Lines In Spodumene Along The Magnetic Axes

Transition	H    z	H    y	H    x
$H_1$	2,612	11,923	10,795
$H_2$	5,635	9,934	9,399
$H_3$	8,388	8,183	7,978
$H_4$	11,140	6,576	6,916
$H_5$	14,194	5,466	6,693
DPPH	8,394	8,500	8,490

(ii) Comparison of  $\text{Fe}^{+3}$  spectra at room and liquid helium temperatures. In order to determine the order of the energy levels, that is, the sign of  $b_2^0$  in the spin Hamiltonian, one must compare the spectrum of  $\text{Fe}^{+3}$  at room and liquid helium temperatures. The basis of this procedure is the following argument. The electron spin populations of the energy levels are

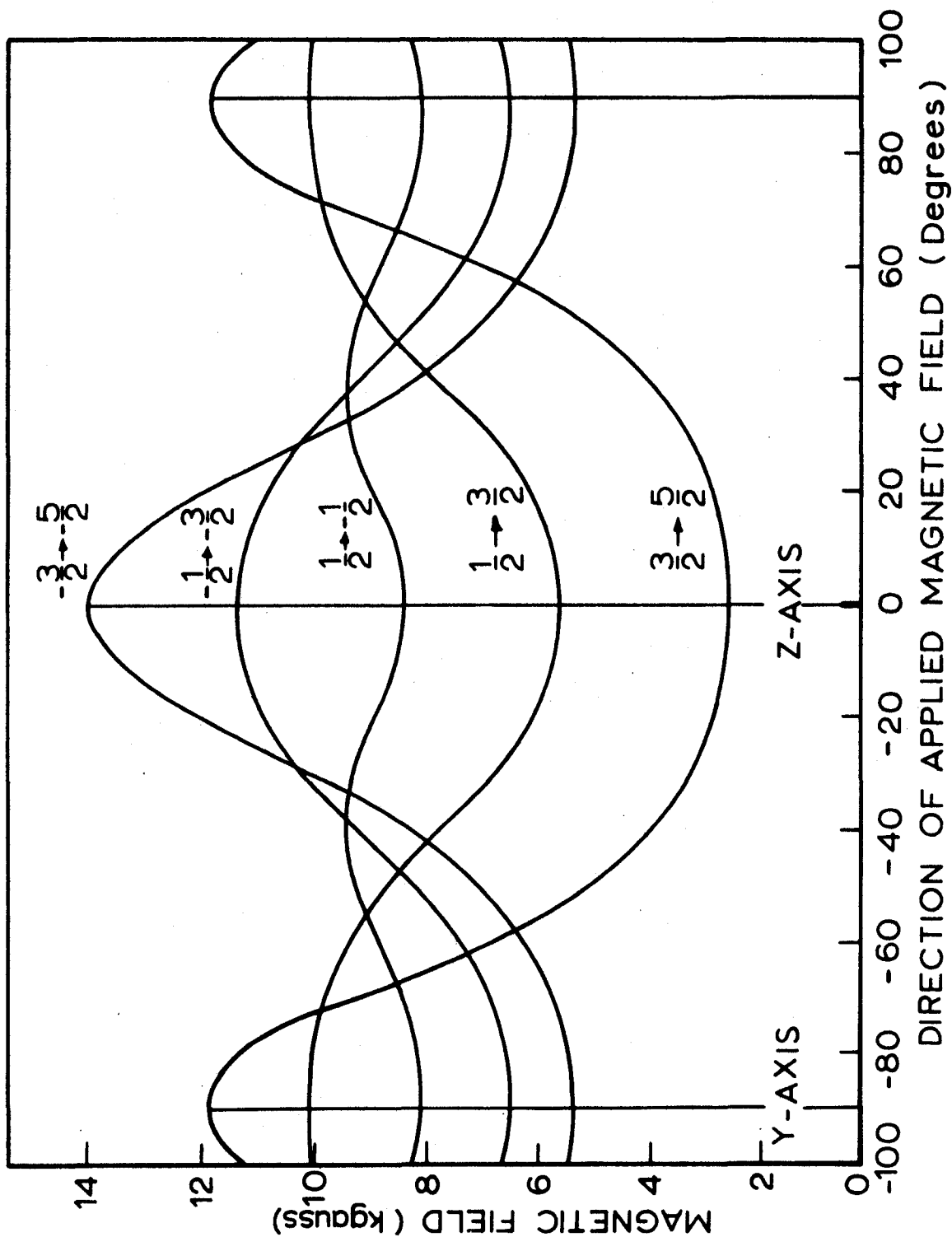


Fig. 13. Angular variation of the EPR spectrum of Fe<sup>3+</sup> in the plane perpendicular to the magnetic x-axis.

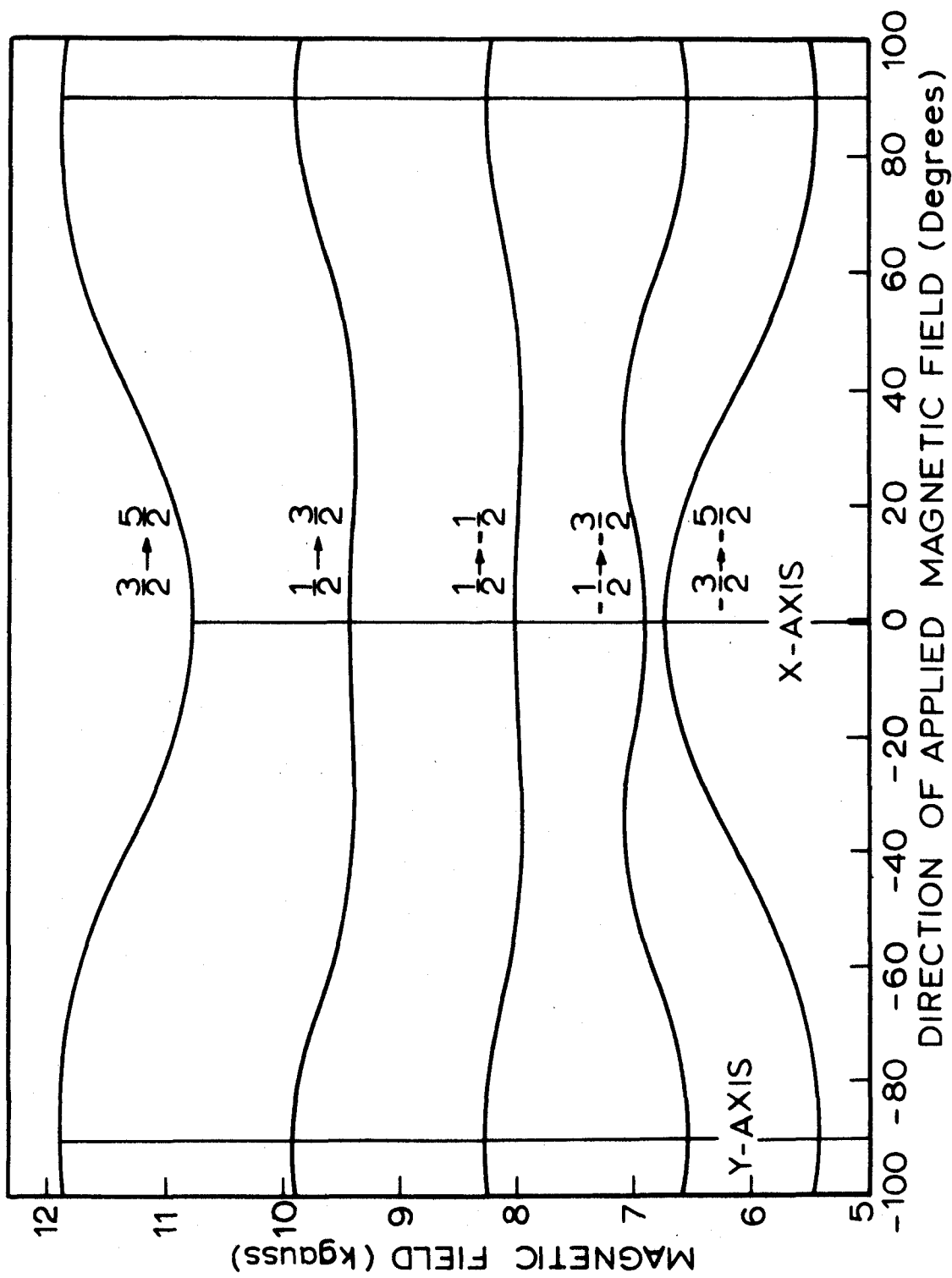


Fig. 14. Angular variation of the EPR spectrum of  $\text{Fe}^{+3}$  in the plane perpendicular to the magnetic z-axis.

determined by the Boltzman factor  $\exp[-\Delta E/kT] \doteq 1-\Delta E/kT$ , where  $\Delta E=h\nu$ ,  $k$  is the Boltzman constant and  $T$  is the absolute temperature. The ground state is more populated even at room temperature but the effect of populations becomes measurable at liquid helium temperature.

Since the only low temperature spectrometer that was available operated at x-band frequencies it was necessary to obtain the comparison of the spectra taken at the two temperatures in this band. The spectra along the  $z$  magnetic axis for the two temperatures are shown in Figure 15. Part (a) shows the room temperature spectrum while part (b) shows the liquid helium temperature spectrum. The ratio of the intensity of the high field line (2) to the low field line (1) is 1.5/1 at room temperature, and 3/1 at liquid helium temperature. This indicates that the high field line has increased its amplitude at low temperature while the low field line has decreased. Hence, the high field line is closer to the ground state than is the low field line. This means that the substates  $M_S = \pm 1/2$  lie lowest and so the sign of  $b_2^0$  is positive when calculated from the spin Hamiltonian.

(iii) Calculation of spin Hamiltonian parameters for  $Fe^{+3}$  in spodumene. The values of the parameters  $b_n^m$  were found by a self-consistent method. Rough values for  $b_n^m$  were first tried in the equations for the  $x$ ,  $y$ - and  $z$ -directions and this process was repeated until a good fit was obtained. The iteration was done using an IBM 1620 computer program and the following results

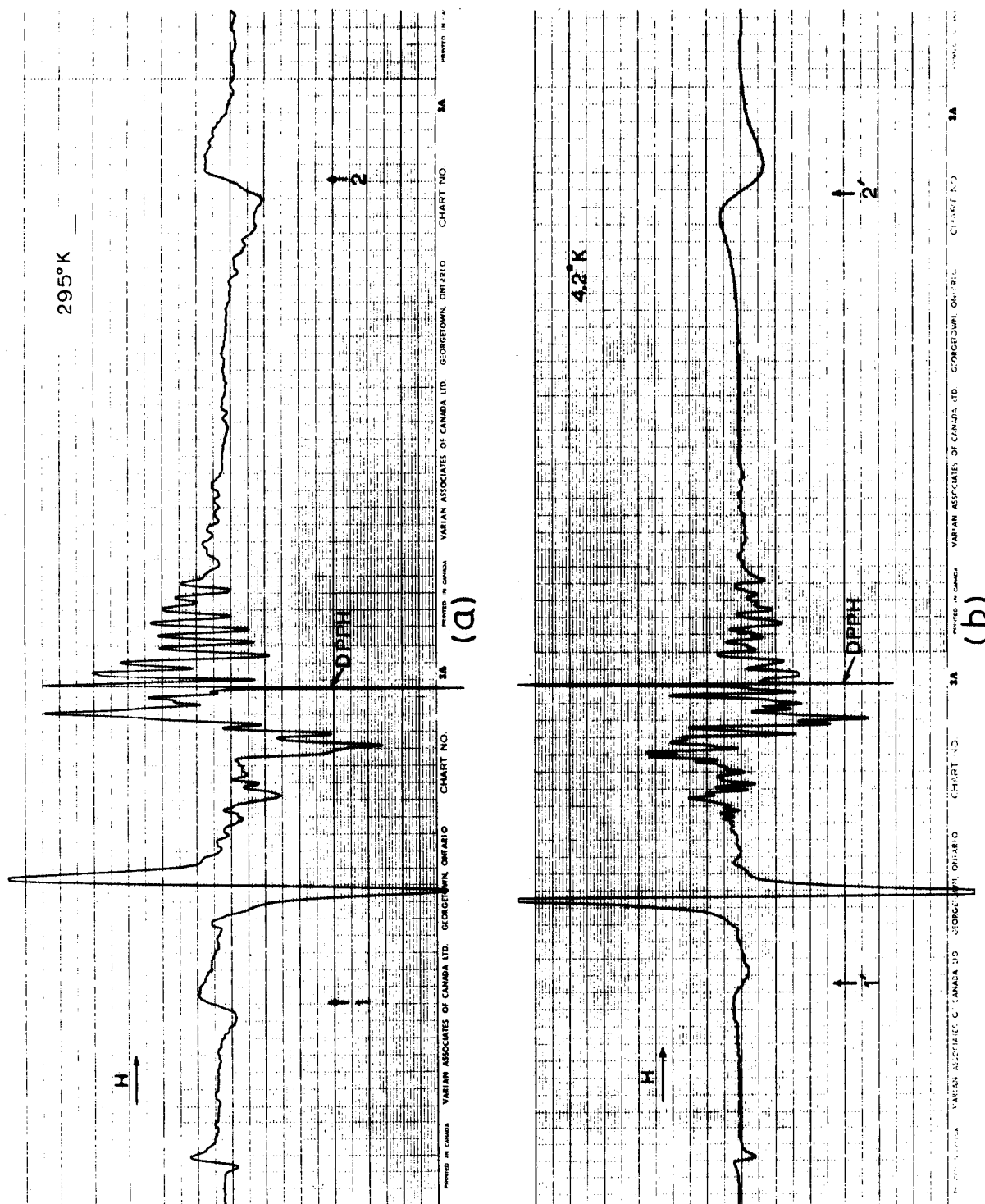


Fig. 15. Comparison of the  $\text{Fe}^{+3}$  spectra for the magnetic field along the z-axis at (a) room temperature and (b) liquid helium temperature.

were obtained:  $g_x = 2.0047 \pm 10$ ,  $g_y = 2.0047 \pm 10$ ,  $g_z = 2.0041 \pm 5$ ,  $b_2^0 = 1,430$ ,  $b_2^2 = 280$ ,  $b_4^0 = 20$ ,  $b_4^2 = -82$ ,  $b_4^4 = 202$ . The  $b_n^m$  values are in gauss.

To check the results, the matrix of Table 3 was diagonalized for each resonant field using the above values of the constants in a computer program. The transitions for the three magnetic axes were fitted to an accuracy of 10 gauss. The values of the energy levels were also calculated at small intervals of magnetic field and were plotted for the three magnetic axes as shown in Figures 16, 17 and 18. Figure 16 also shows the observed x-band transitions. An analysis of the spectrum in this band would be quite difficult, as is evident in this figure.

(iv) Heat-treatment of spodumene. The sample of spodumene used in the analysis above was heated to about  $600^\circ \text{C}$  in vacuum and then quickly cooled in water. The  $\text{Fe}^{+3}$  spectrum did not change due to this treatment other than the fact that the five iron lines increased their line widths. A diagram of the spectrum along the z-axis of iron in heat-treated spodumene is shown in Figure 19.

(v) Line intensities of  $\text{Fe}^{+3}$  in spodumene. The relative intensities of the five iron lines along the z-axis, for equal line widths, should be proportional to  $(S+M_s)(S-M_s+1)$ . The intensity ratios should therefore be  $I_{5/2 \rightarrow 3/2} : I_{3/2 \rightarrow 1/2} : I_{1/2 \rightarrow -1/2} : I_{-1/2 \rightarrow -3/2} : I_{-3/2 \rightarrow -5/2} = 5:8:9:8:5$ . Since the lines did not have equal line widths it was found desirable to measure their integrated intensities as well as their line widths. This was done for the heated as well as

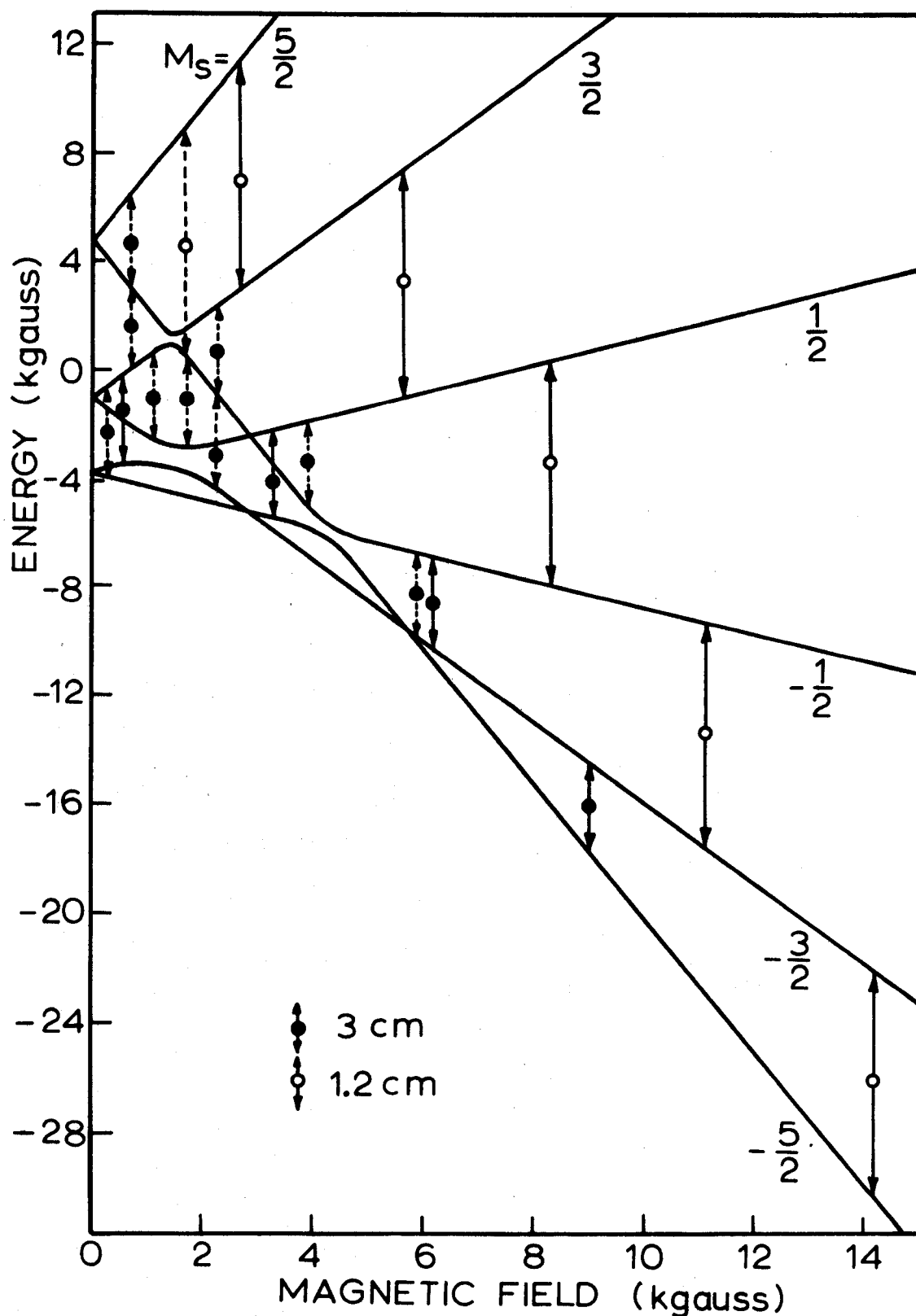


Fig. 16. Energy level diagram of  $\text{Fe}^{+3}$  with the magnetic field along the z-axis. The vertical dashed lines indicate forbidden transitions, while the solid lines indicate allowed transitions. The transitions obtained at x-band frequencies are also indicated.

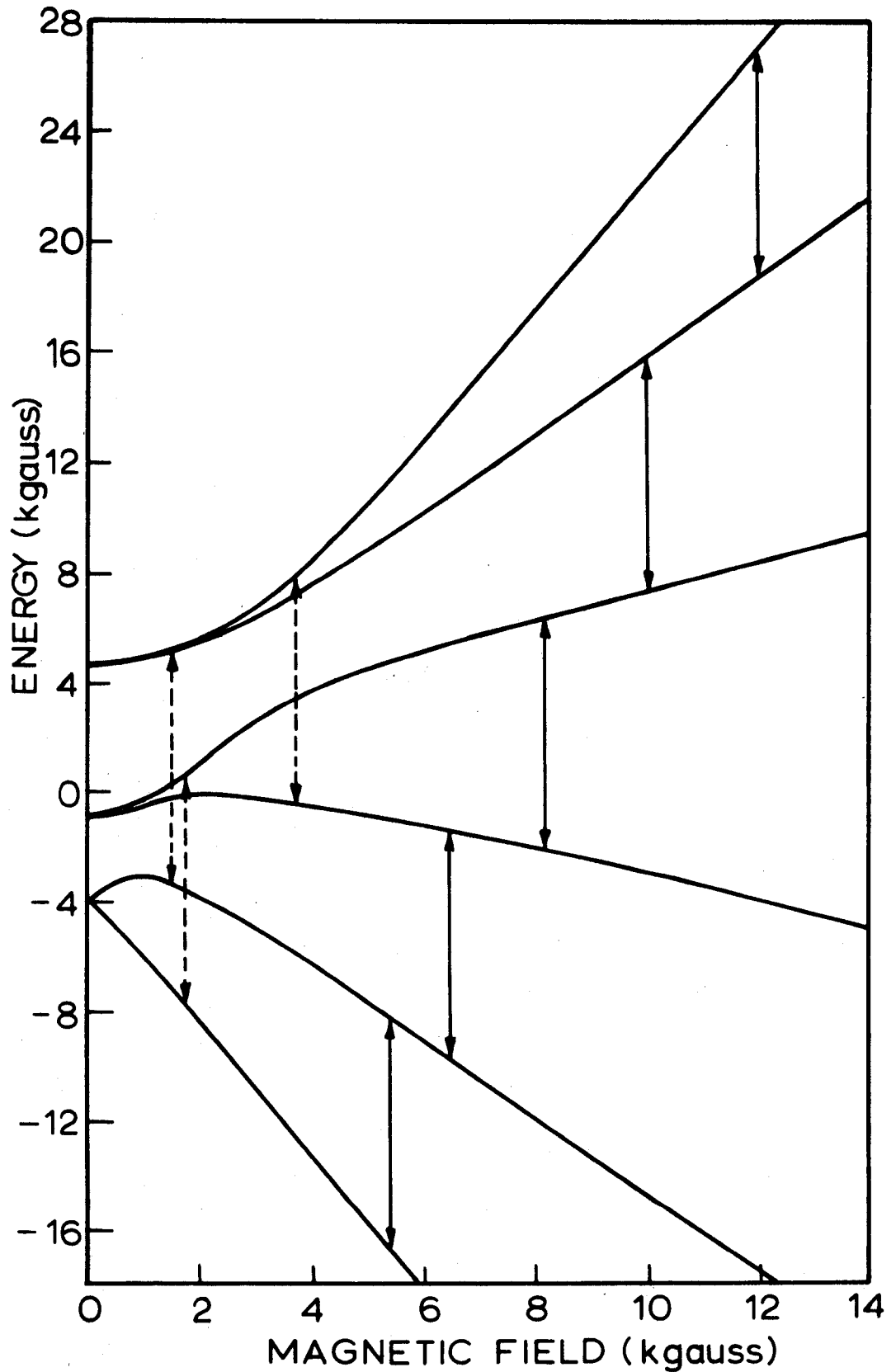


Fig. 17. Energy level diagram of  $\text{Fe}^{+3}$  with the magnetic field along the y-axis. The vertical dashed lines indicate forbidden transitions, while the solid lines indicate allowed transitions.

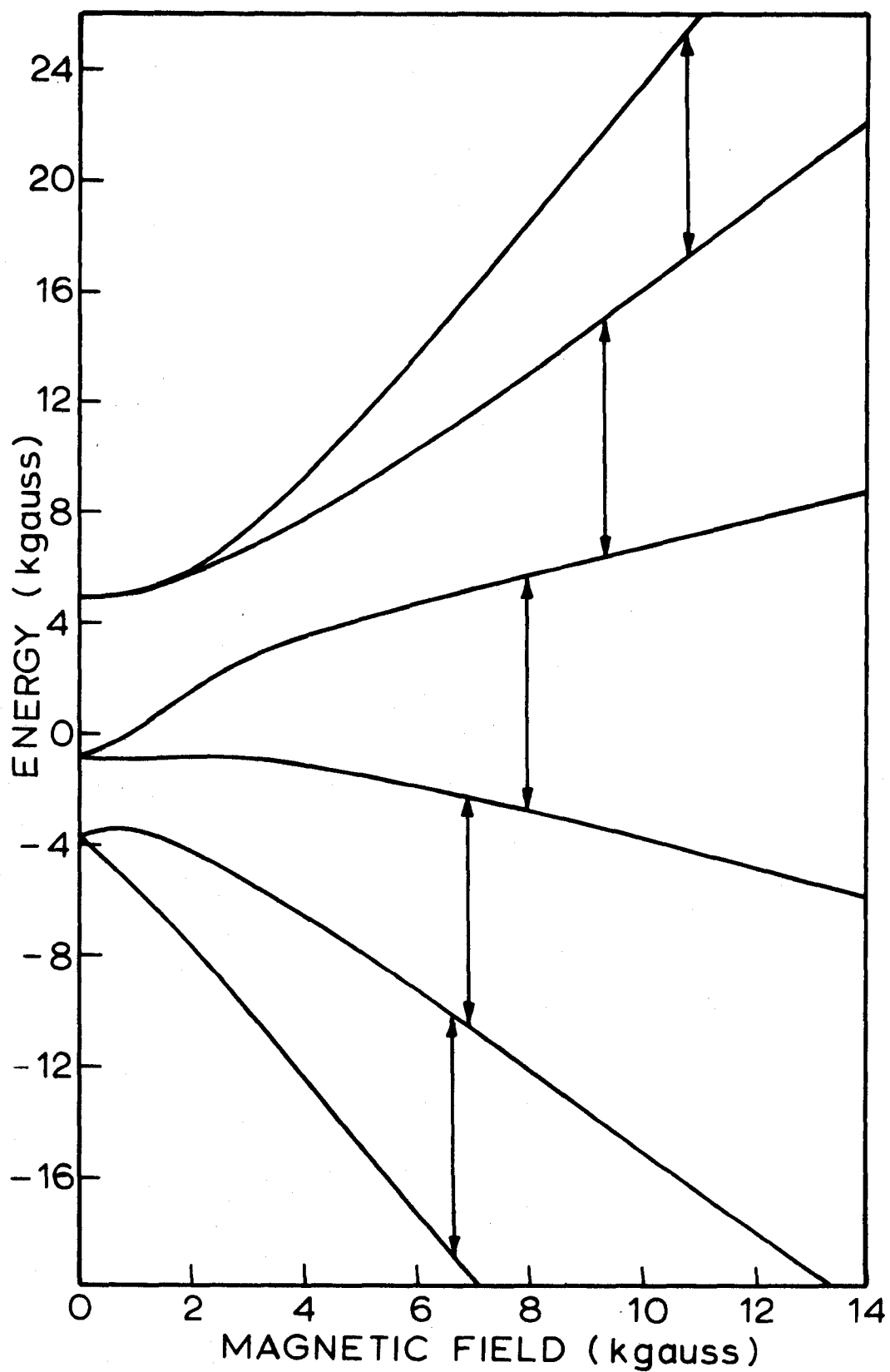


Fig. 18. Energy level diagram of  $\text{Fe}^{+3}$  with the magnetic field along the x-axis. The vertical solid lines indicate allowed transitions.



Fig. 19. The spectra of heat-treated spodumene with the magnetic field along the z-axis of  $\text{Fe}^{+3}$ . Numbers 1-5 indicate the five  $\text{Fe}^{+3}$  lines, a - e indicate the five groups of lines due to  $\text{Mn}^{+2}$ , and F shows a forbidden line of iron.

the unheated crystal of spodumene. The absorption line shapes were photographed as displayed on an oscilloscope and the areas were measured from the photographs. The results are given in Table 6.

TABLE 6. Line Widths And Integrated Intensities Of The Five Iron Lines In Spodumene Before And After Heat Treatment

Transition	Before Heat-Treatment		After Heat-Treatment	
	Line Width (gauss)	Integrated Line Intensity	Line Width (gauss)	Integrated Line Intensity
$5/2 \rightarrow 3/2$	77	$1.7 \pm 0.5$	125	$2.0 \pm 0.5$
$3/2 \rightarrow 1/2$	50	4.5	77	4.5
$1/2 \rightarrow -1/2$	20	9	26	9
$-1/2 \rightarrow -3/2$	53	4.5	70	4.5
$-3/2 \rightarrow -5/2$	75	1.7	145	2.0

#### B. $Mn^{+2}$ In Kunzite

The EPR spectrum of  $Mn^{+2}$  in kunzite was analyzed at room temperature and at k-band frequencies. In the unheated samples the  $Mn^{+2}$  spectrum is split into four complexes with principal magnetic axes only slightly displaced from each other. A typical spectrum is shown in Figure 20. From the k-band results it was determined that the analysis could equally well have

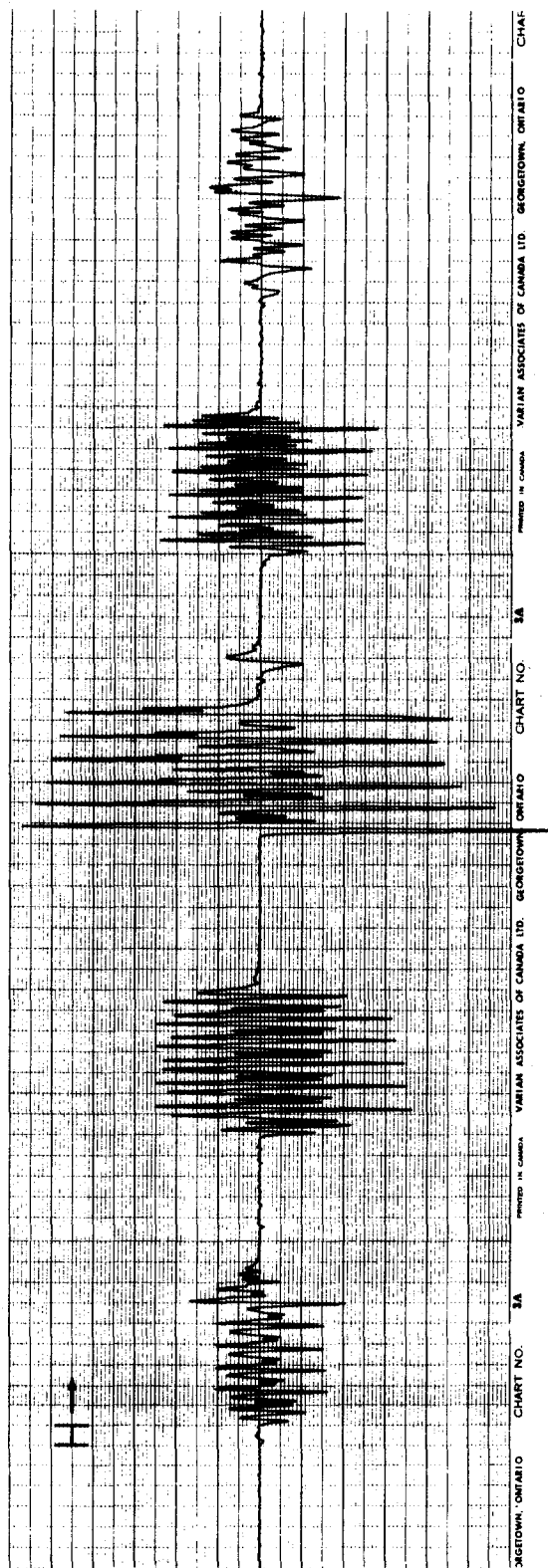


Fig. 20. A typical spectrum near the z-axes of the four magnetic complexes of  $Mn^{+2}$  in kunzite.

been done at x-band frequencies.

(i) Determination of the magnetic axes. Using the cavity system of Figure 9, in conjunction with a stereographic plot, it was possible to sort out the four complexes. The relative positions of the complexes with respect to each other and to the crystallographic axes are shown on the stereographic plots of Figures 21 and 22. In determining a magnetic axis the crystal is rotated in steps on its horizontal mount and the magnetic field position is adjusted each time until a maximum spacing of the EPR fine-structure lines is obtained. Two groups of four magnetic axes were determined in this manner. The axes in the group that showed the largest spacing of the fine-structure lines were designated the z-axes. Their positions were approximately in the (010) plane, making an average angle of  $24^\circ$  to the c-axis and  $46^\circ$  to the a-axis. The axes in the second group were designated the y-axes. Their positions were near the [010] direction. A third group of four magnetic axes, designated the x-axes, were not well resolved and so no measurements were made for these. However, the positions of the x-axes could be predicted from the y- and z-axes on the stereographic plot.

The magnetic field positions of the  $m_I = + 5/2$  EPR lines for each of the four complexes along the y- and z-axes were measured by proton resonance and are listed in Table 7.

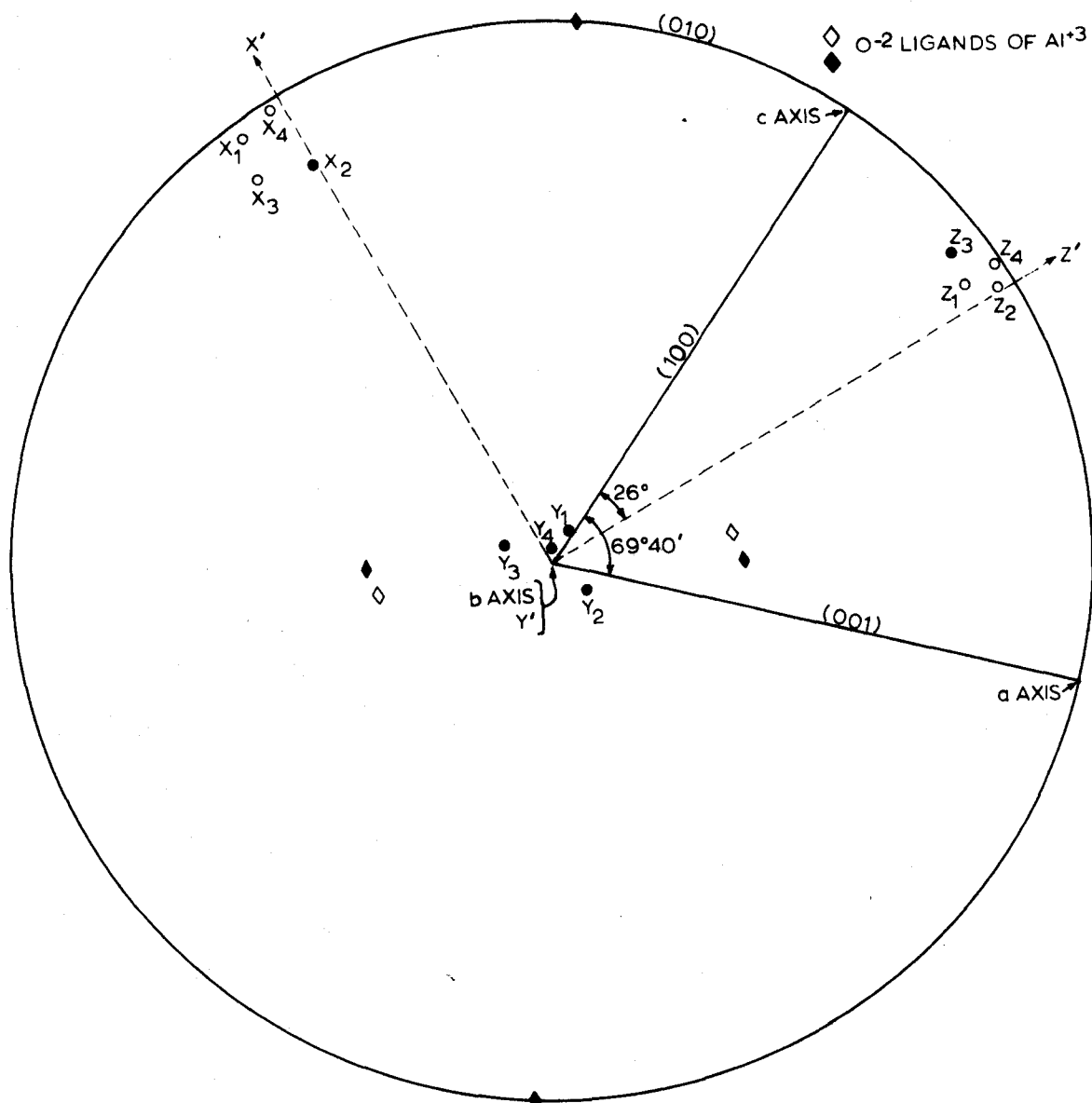


Fig. 21. Stereographic projection of the  $Mn^{+2}$  magnetic axes in kunzite, along with the oxygen ligands surrounding an  $Al^{+3}$  site. The quantities  $x_1, y_1, z_1$ , etc. represent axes due to unheated kunzite while  $x', y', z'$  represent those due to the thermally quenched samples. Shaded symbols represent points through the top hemisphere while the unshaded ones represent points through the bottom hemisphere.

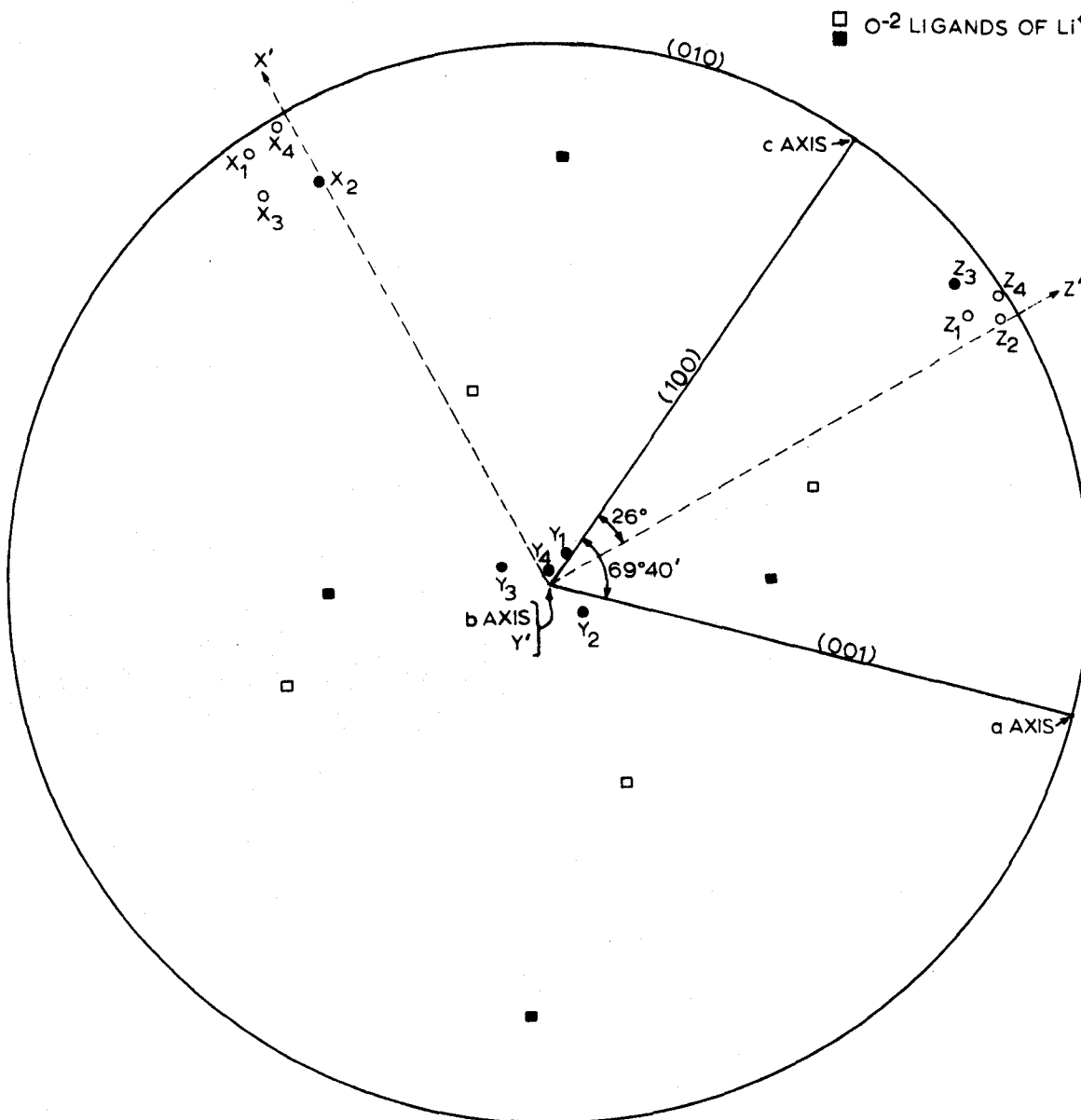


Fig. 22. Stereographic projection of the  $Mn^{+2}$  magnetic axes in kunzite, along with the oxygen ligands surrounding an  $Li^+$  site. The quantities  $x_1, y_1, z_1$ , etc, represent axes due to unheated kunzite while  $x', y', z'$  represent those due to the thermally quenched samples. Shaded symbols represent points through the top hemisphere while the unshaded ones represent points through the bottom hemisphere.

TABLE 7. Magnetic Field Positions For The  $m_I = + 5/2$  Transitions Of Each Group Of Hyperfine Lines In Each Of The Four Complexes.

	Site 1	Site 2	Site 3	Site 4
<b>z-axis</b>				
H <sub>5</sub>	10,474	10,456	10,472	10,447
H <sub>4</sub>	9,326	9,314	9,325	9,308
H <sub>3</sub>	8,165	8,163	8,156	8,163
H <sub>2</sub>	7,006	7,009	6,991	7,025
H <sub>1</sub>	5,865	5,864	5,857	5,894
DPPH	8,383	8380	8376	8381
<b>y-axis</b>				
H <sub>5</sub>	6,401	6,393	6,585	6,568
H <sub>4</sub>	7,251	7,247	7,447	7,415
H <sub>3</sub>	8,122	8,114	8,127	8,123
H <sub>2</sub>	9,018	9,026	8,854	8,876
H <sub>1</sub>	9,981	9,975	9,787	9,824
DPPH	8,390	8,382	8,392	8,393

(ii) Comparison of  $Mn^{+2}$  spectra at room and liquid helium temperatures. The sign of  $b_2^0$  for  $Mn^{+2}$  is determined in a similar manner to that of  $Fe^{+3}$ . Figure 23 shows a comparison of the x-band spectra near the z-axes at room and liquid helium temperatures. It is seen that the high field lines have increased their intensities with respect to the low field lines at liquid helium

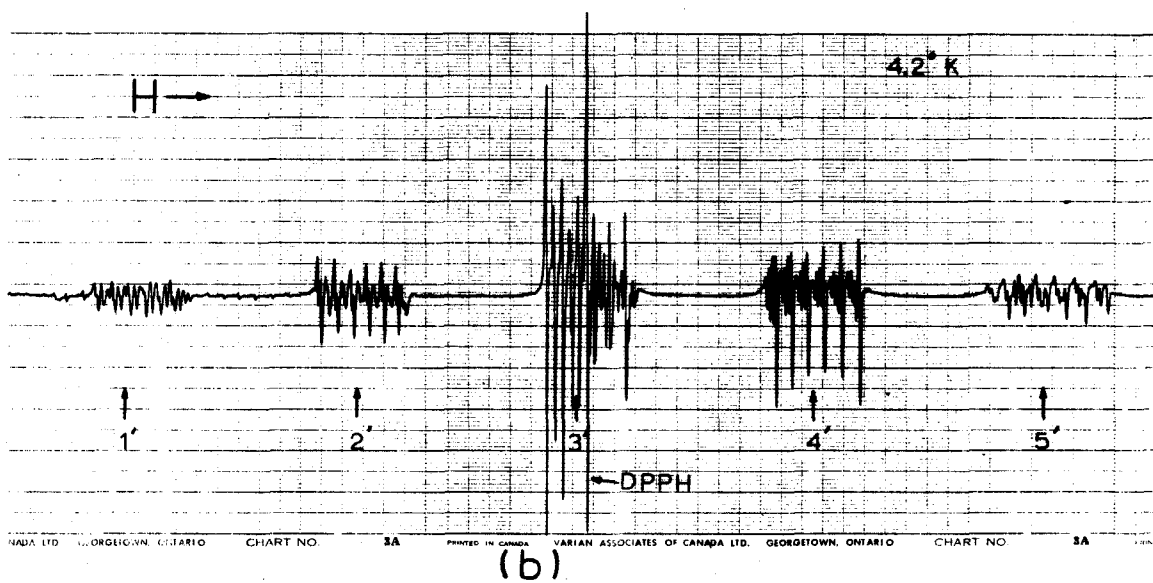
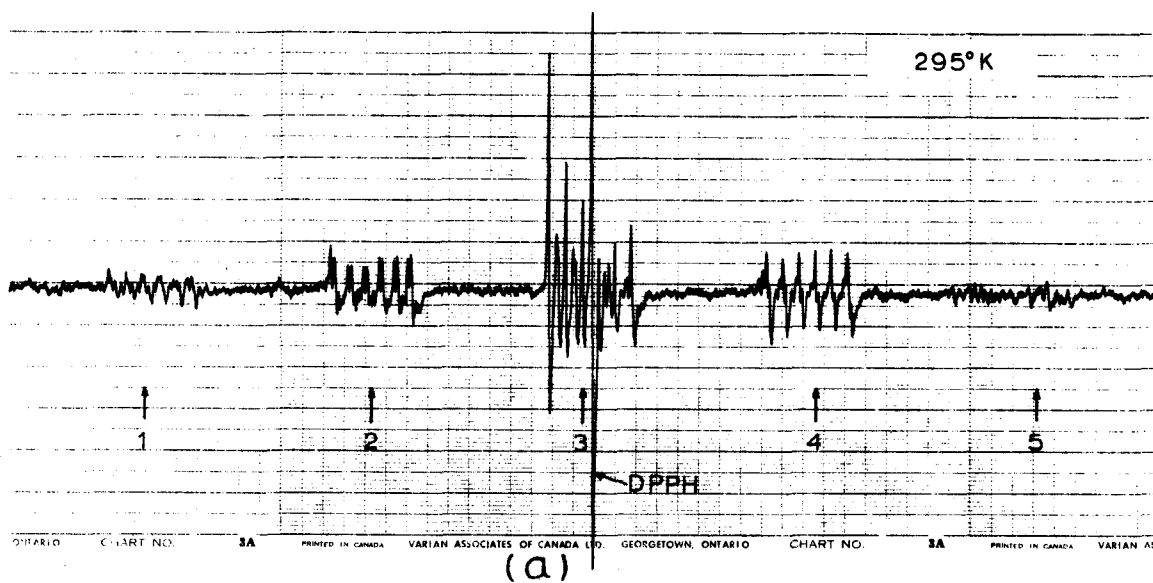


Fig. 23. Comparison of the  $\text{Mn}^{+2}$  spectra in kunzite for the magnetic field near the z-axes at (a) room temperature and (b) liquid helium temperature.

temperature. This means that the high field line is between the ground state energy level and the next highest level. This also means that the substates  $M_S = \pm 1/2$  lie lowest and so the sign of  $b_2^0$  is positive when calculated from the spin Hamiltonian.

(iii) Calculation of spin Hamiltonian parameters for  $Mn^{+2}$  in kunzite. The parameters  $b_n^m$ , A and B were found from the equations 8, 9, and 10 using the magnetic field positions for the hyperfine lines given in Table 7. The results are in Table 8.

TABLE 8. The Spin Hamiltonian Parameters For The Four Magnetic Complexes Of  $Mn^{+2}$  In Kunzite.

Parameter	Site			
	1	2	3	4
$g_z$	2.0014 $\pm 0.0010$	2.0024 $\pm 0.0010$	2.0014 $\pm 0.0010$	2.0012 $\pm 0.0010$
$g_y$	2.0036 $\pm 0.0025$	2.0034 $\pm 0.0025$	2.0038 $\pm 0.0025$	2.0031 $\pm 0.0025$
A	-89.2	-89.1	-88.9	-89.1
B	-88.2	-89.1	-88.9	-88.8
$b_2^0$	578	576	580	571
$b_2^2$	311	316	191	224
$b_4^0$	-1.1	-0.64	-1.9	-0.46
$b_4^2$	93	165	-53	-30
$b_4^4$	-104	-168	-51	-35

The values of  $b_n^m$ , A and B are in gauss.

Using the values of the constants for site 3 as a typical

case, the matrix of the spin Hamiltonian was diagonalized by employing an IBM 1620 computer program. Also, the energy levels were calculated along the z-, y- and x-magnetic axes for small intervals of the magnetic field. The results are plotted in Figures 24, 25 and 26, respectively. The line intensities for the manganese EPR lines have the approximate ratios of 1:3:9:3:1. The above remarks also apply to the remaining three manganese sites.

(iv) Heat treatment of kunzite. The kunzite crystals were heated in vacuum in steps of  $50^{\circ}$  C and then quickly cooled in water. After each step of heating and cooling the EPR spectrum was recorded. It was observed that the spectral lines due to the four  $Mn^{+2}$  complexes gradually decreased their intensities while spectral lines due to  $Mn^{+2}$  in a single complex formed and increased their intensities with increasing temperature. At  $500^{\circ}$  C the spectrum is virtually that due to manganese in a single complex, indicating that the twofold axis through a manganese site is restored. This effect is shown in Figure 27 for the  $M_s = 5/2 \rightarrow 3/2$  group of hyperfine lines with the magnetic field direction along the z-axis.

The study of the angular variation of the spectra revealed that the y-axis pointed along the  $[010]$  direction and the x- and z-axes were located in the (010) plane, the z-axis making an angle of  $26^{\circ}$  with the c-axis and  $44^{\circ}$  with the a-axis. The positions of the axes are shown on the stereographic plot of Figure 21. Figure 28 (a), (b) and (c) shows the spectra of the single manganese complex with the magnetic field directions

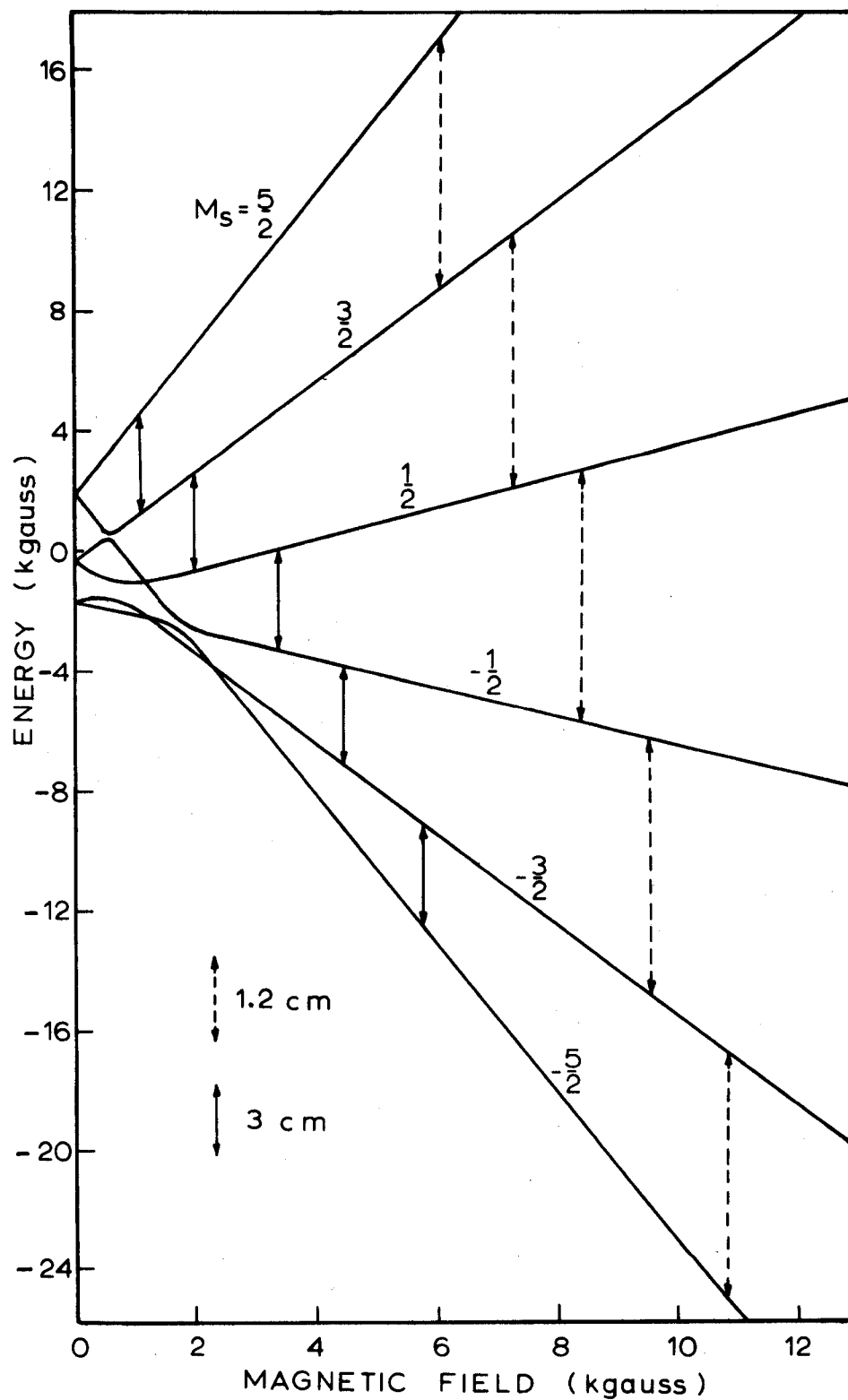


Fig. 24. Energy level diagram of  $Mn^{+2}$  in kunzite with the magnetic field direction along the z-axis. The vertical transitions indicate the centers of gravity of the hyperfine lines at x- and k-band frequencies as indicated.

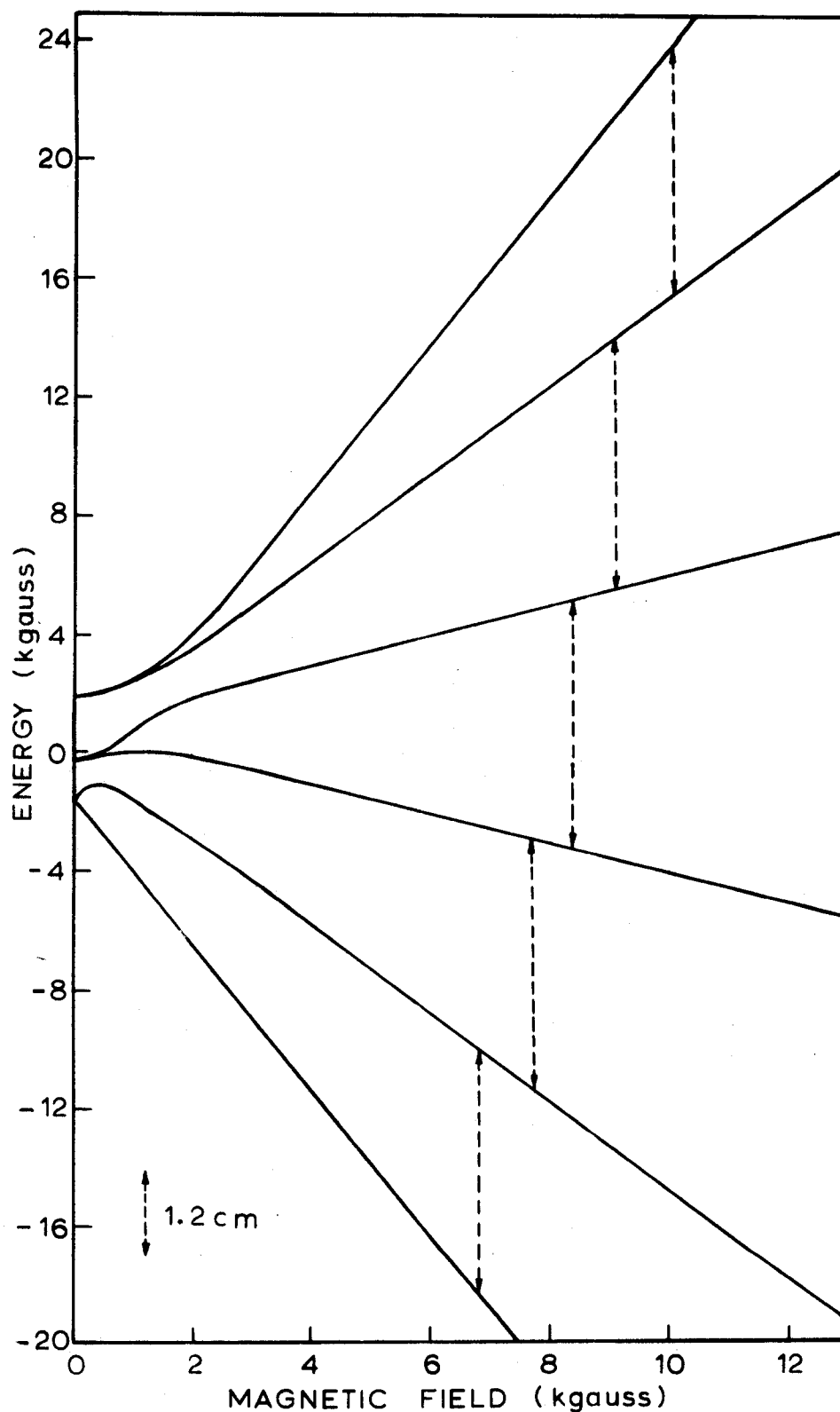


Fig. 25 Energy level diagram of  $\text{Mn}^{+2}$  in kunzite with the magnetic field direction along the y-axis. The vertical dashed lines indicate the centers of gravity of the hyperfine lines at k-band frequencies.

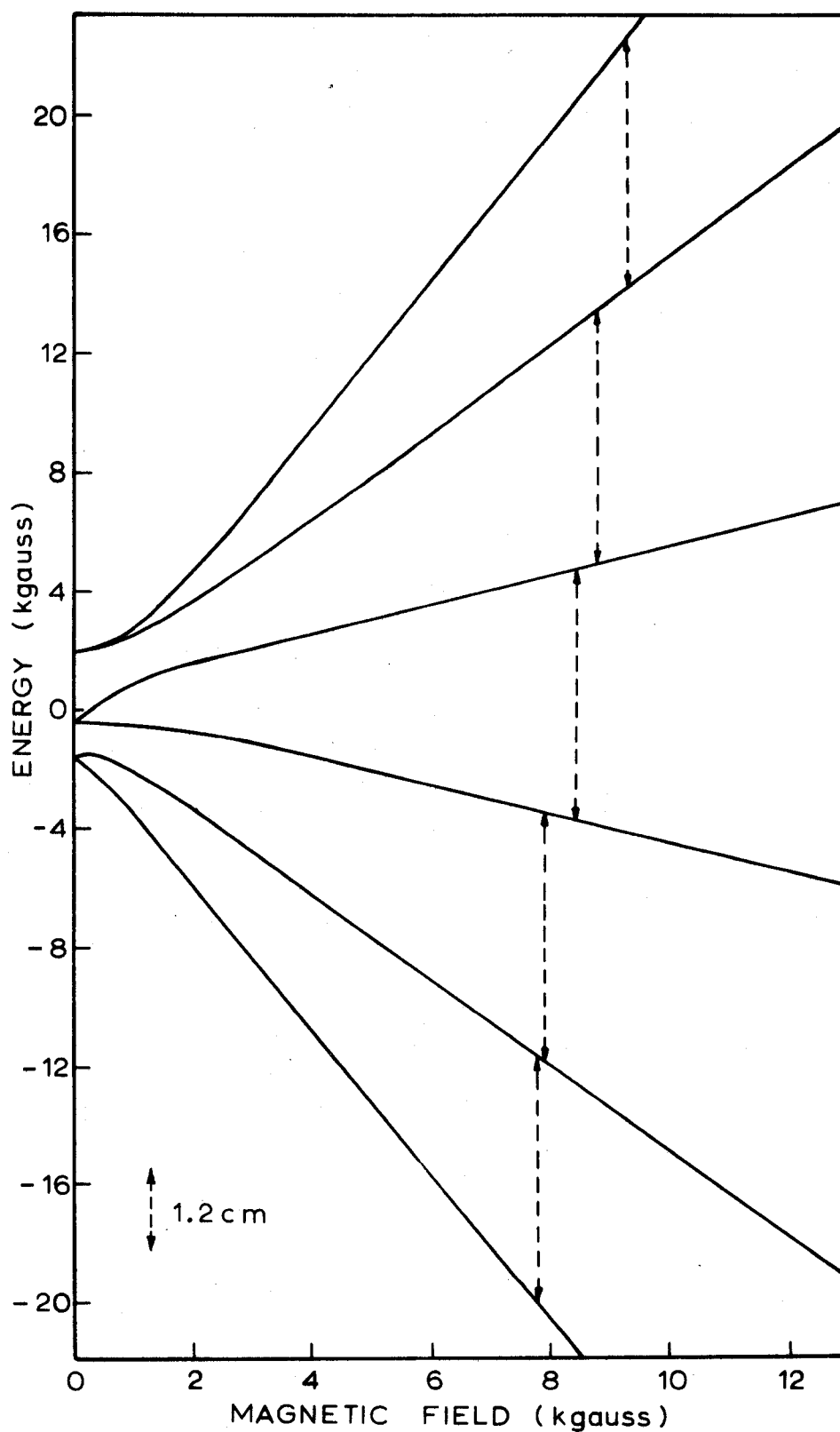


Fig. 26. Energy level diagram of  $\text{Mn}^{+2}$  in kunzite with the magnetic field direction along the x-axis. The vertical dashed lines indicate the predicted positions of the centers of gravity of the hyperfine lines at k-band frequencies.

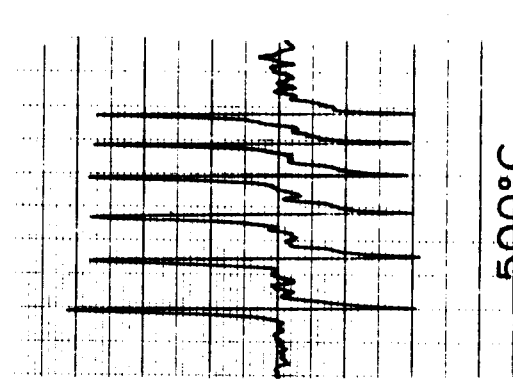
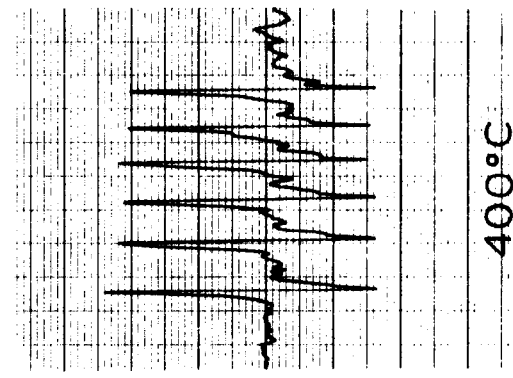
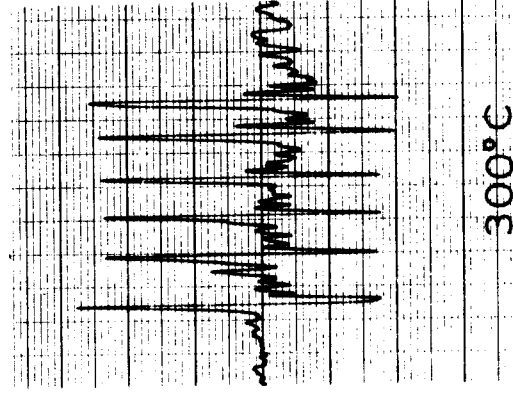
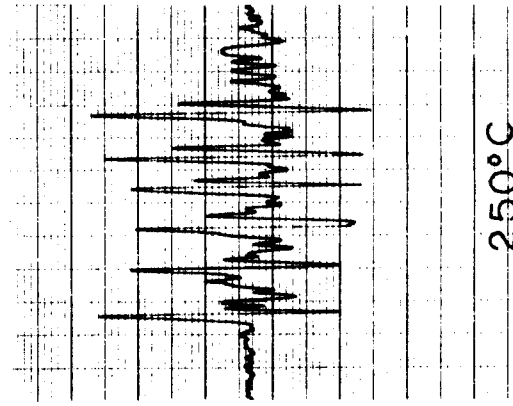
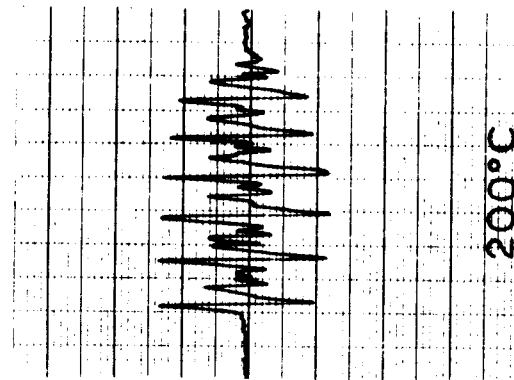
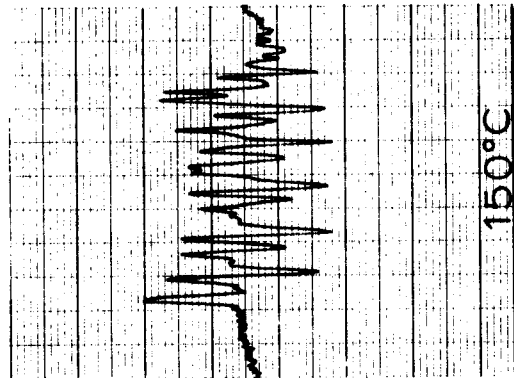
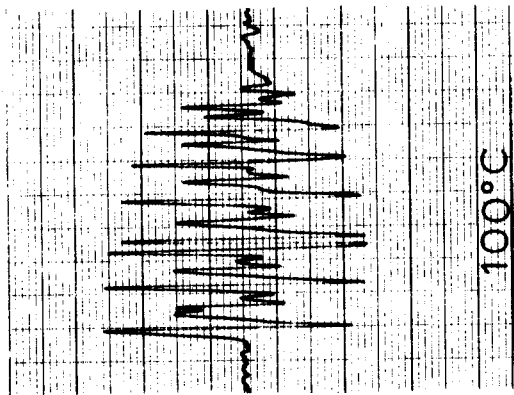
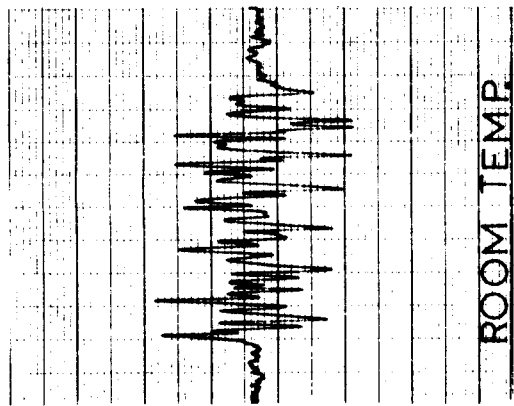
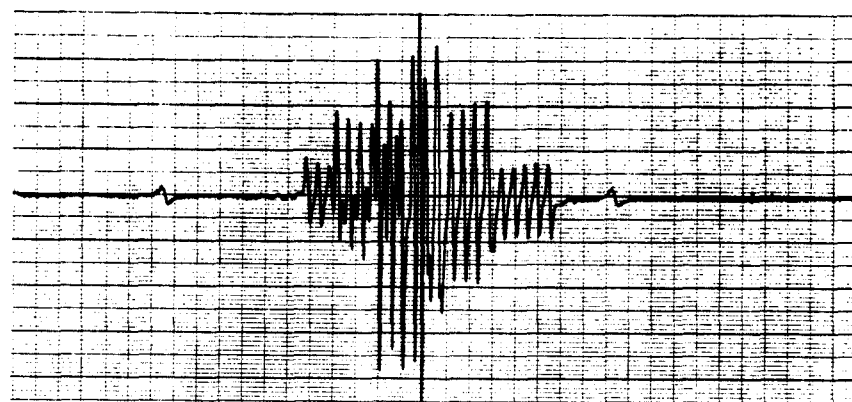
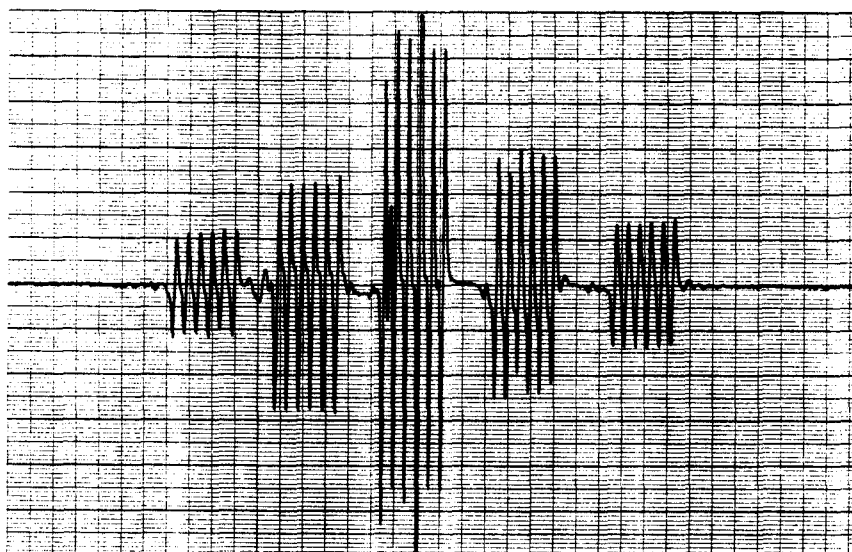


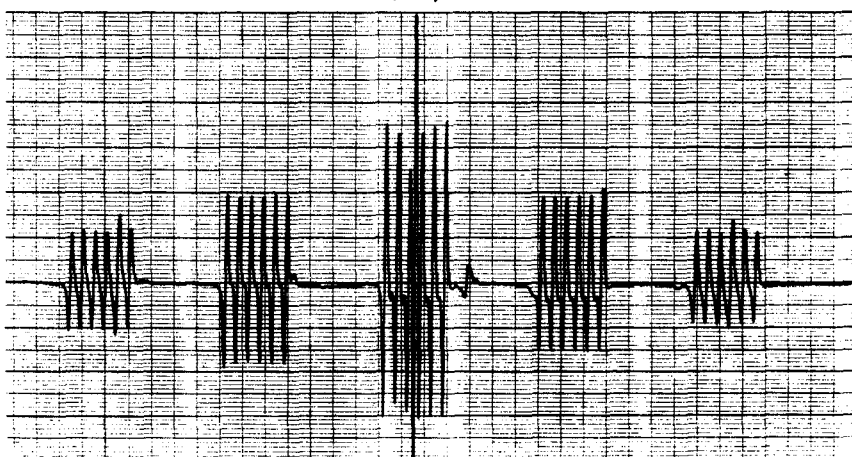
Fig. 27. Effect of thermal quenching of kunzite from various elevated temperatures. The hyperfine lines are due to the  $M_S = 5/2 \rightarrow 3/2$  transition.



(a)



(b)



(c)

Fig. 28. The spectra of  $Mn^{+2}$  in heat treated kunzite. Part (a) shows the x-axis, (b) the y-axis, and (c) the z-axis. Some low intensity  $Fe^{+3}$  lines also appear in the spectra. The strong central line is due to DPPH.

along the x-, y- and z-axes, respectively. Some low intensity  $\text{Fe}^{+3}$  lines are also present, as these figures show. The ratios of the intensities of the manganese EPR lines were measured to be 3:5:9:5:3 along the z-axis.

The magnetic field positions of the  $m_I = + 5/2$  transitions for the z- and y-axes are given in Table 9.

TABLE 9. Magnetic Field Positions For The  $m_I = + 5/2$  Transitions Of Each Group Of Hyperfine Lines In Heat-Treated Kunzite.

	$H_5$	$H_4$	$H_3$	$H_2$	$H_1$	DPPH
z axis	10,515	9,371	8,209	7,056	5,915	8,427
y axis	6,625	7,395	8,189	9,026	9,927	8,442

The spin Hamiltonian parameters for  $\text{Mn}^{+2}$  in the single complex were calculated from equations 8, 9 and 10 and found to be  $g_z = 2.0012 \pm 10$ ,  $g_y = 1.9972 \pm 25$ ,  $A = -89.2$ ,  $B = -88.4$ ,  $b_2^0 = 577$ ,  $b_2^2 = 243$ ,  $b_4^0 = -1.07$ ,  $b_4^2 = 35$ ,  $b_4^4 = -44$ . The values of  $b_n^m$  are in gauss.

It was not possible to restore the four complex spectra or the pink color of the kunzite crystal. Several attempts were made. In one attempt, the crystal was heated to  $600^\circ \text{C}$  and slowly cooled in vacuum over a period of one week. In another attempt the cooling was done in a normal atmosphere.

The ratio of the amplitudes of the increasing one-complex spectrum and the decreasing four-complex spectra (called  $n_d/n_a$ ) is plotted versus the temperature in Figure 29.

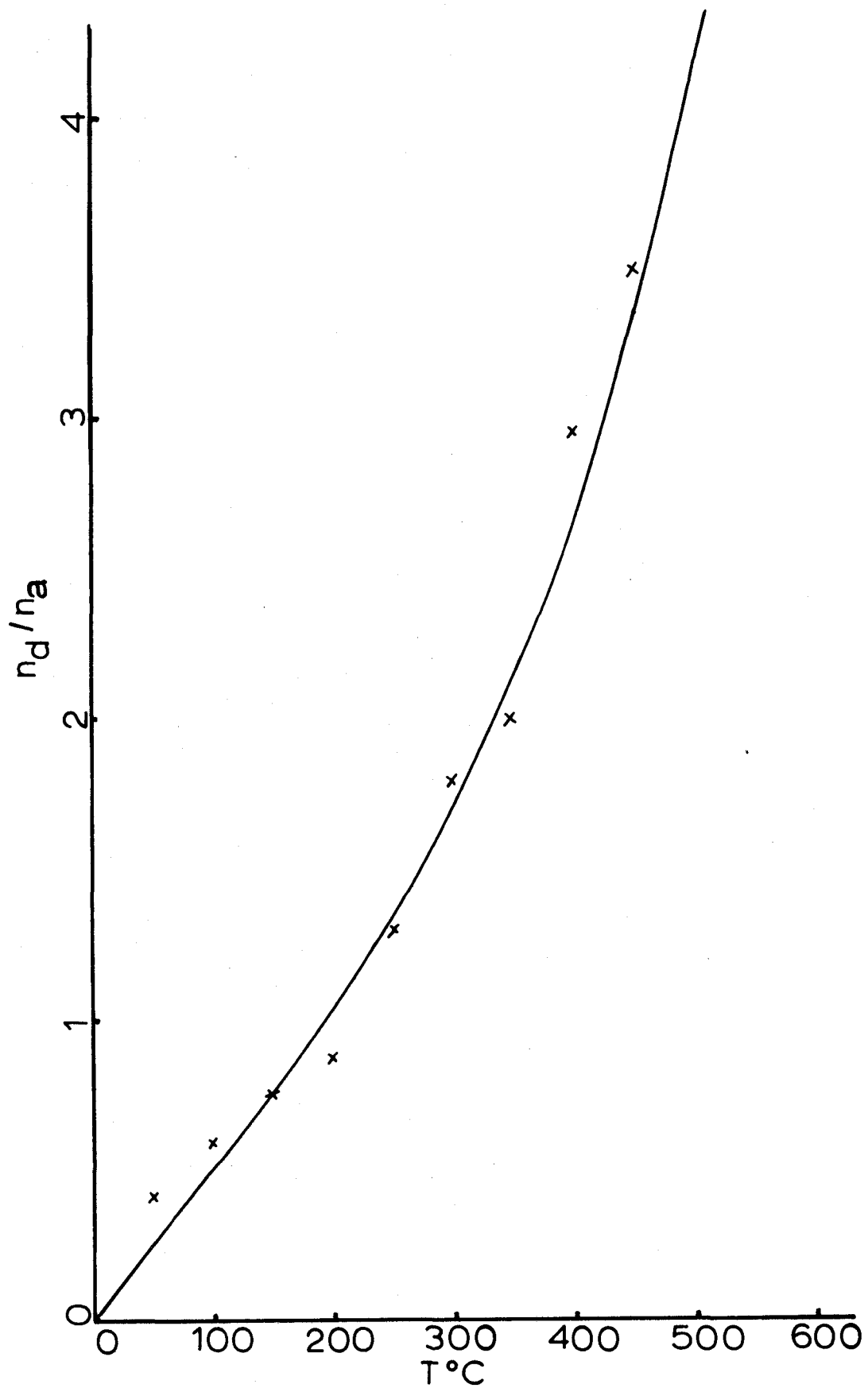


Fig. 29. Increase of amplitude ratios with increase of temperature.

### C. Analysis Of Hiddenite Crystals

The hiddenite crystals contained a prominent amount of  $\text{Fe}^{+3}$  ions and only a very small amount of  $\text{Mn}^{+2}$ . The spectra of these ions in hiddenite are identical to those in ordinary spodumene. A typical spectrum with the magnetic field along the z-axis of  $\text{Fe}^{+3}$  is shown in Figure 29. Part (a) of the figure shows the spectrum in unheated hiddenite and (b) shows the same spectrum after the crystal had been heated to  $600^\circ \text{C}$  in vacuum and then quenched in water. Here again the manganese spectrum in the heat-treated crystal collapsed into one spectrum.

The line widths and integrated line intensities of  $\text{Fe}^{+3}$  in unheated and heat-treated hiddenite are listed in Table 10.

TABLE 10. Line Widths And Integrated Intensities Of The Five Iron Lines In Hiddenite Before And After Heat Treatment.

Transition	Before Heat Treatment		After Heat Treatment	
	Line Width (gauss)	Integrated Line Intensity	Line Width (gauss)	Integrated Line Intensity
$\frac{5}{2} \rightarrow \frac{3}{2}$	70	$2.4 \pm 0.5$	90	$2.7 \pm 0.5$
$\frac{3}{2} \rightarrow \frac{1}{2}$	42	5	54	6
$\frac{1}{2} \rightarrow -\frac{1}{2}$	28	9	31	9
$-\frac{1}{2} \rightarrow -\frac{3}{2}$	43	5	51	6
$-\frac{3}{2} \rightarrow -\frac{5}{2}$	90	2.4	115	2.7

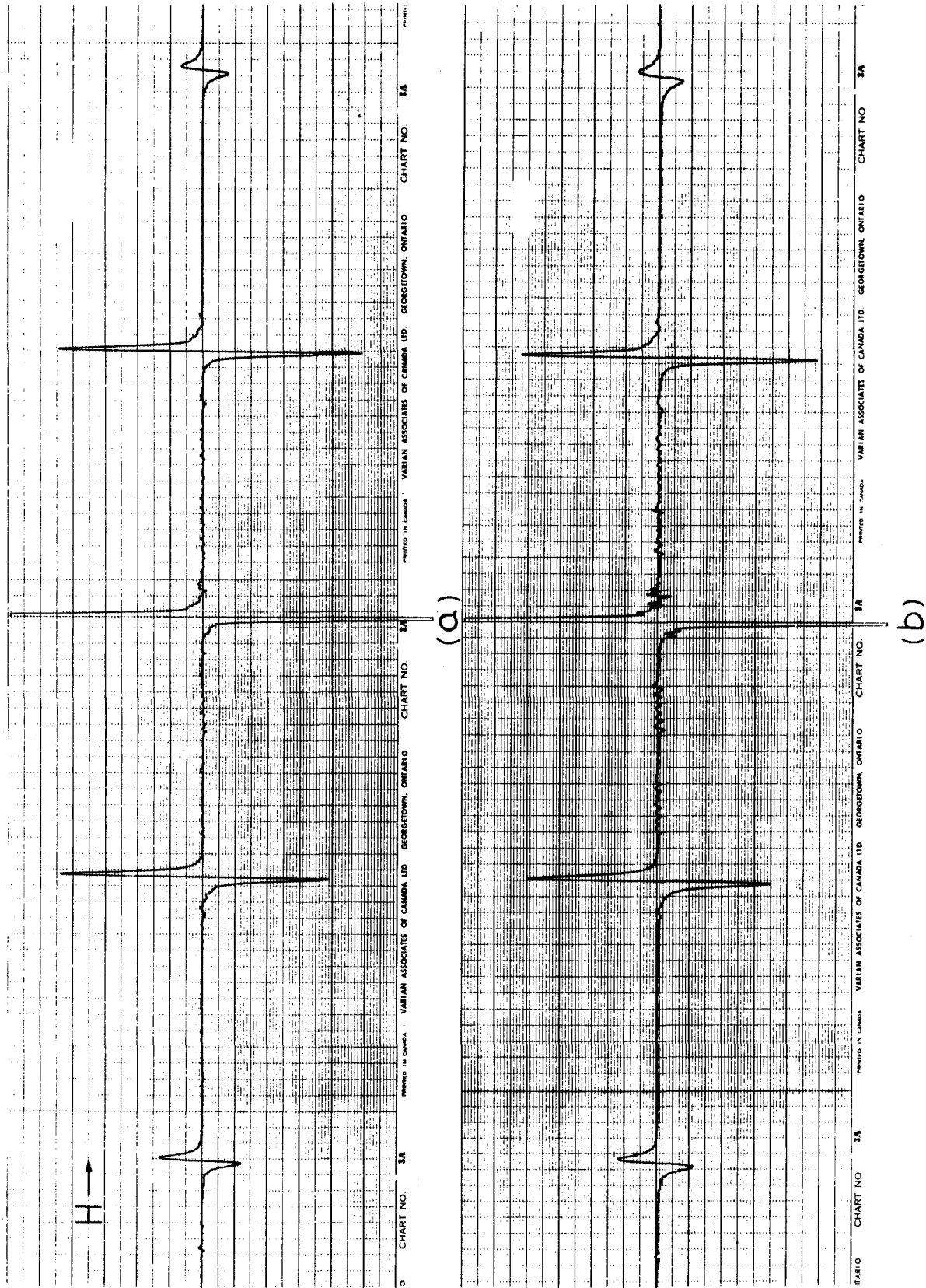


Fig. 30. Spectra of hiddenite with the magnetic field along the z-axis of  $Fe^{+3}$  in (a) the unheated crystal and (b) the heated crystal.

## VI

### DISCUSSION AND CONCLUSIONS

The Hamiltonian given by equation (4) is not complete. It only describes completely the quadratic or orthorhombic parts. The cubic part, which has the coefficient  $b_{44}^4$  should be replaced by terms of the form<sup>15</sup>.

$$b_{44}^4 o_{44}^4 \rightarrow b_{44}^4 \sum_{m=0}^4 a_{44}^m (\alpha \beta \gamma) o_{44}^m,$$

where  $a_{44}^m (\alpha \beta \gamma)$  are functions of the Euler angles which determine the cubic coordinates with respect to the orthorhombic coordinates. These angles cannot be found in this experiment and, therefore, very little can be said about the cubic coefficient occurring in the spin Hamiltonian.

On the other hand, one can correlate the values of  $b_2^0$  and  $b_2^2$  with electric quadrupole data. Volkoff et al<sup>16</sup> and Petch et al<sup>17</sup> have investigated the electric quadrupole resonance spectra of <sup>7</sup>Li and <sup>27</sup>Al in spodumene. Table 11 summarizes their results and the results of this investigation pertaining to the orthorhombic parameters  $b_2^0$  and  $b_2^2$ .  $\Phi_{zz}$ , which occurs in an expression for  $C_z$  (see Volkoff<sup>35</sup>), is related to our  $\Phi'_{zz}$  of equation (11) by  $\Phi'_{zz} = \Phi_{zz} / (1 - \gamma_\infty)$ , where  $\gamma_\infty$  is the anti-shielding factor.

By comparison of the  $\eta$  values obtained by EPR and quadrupole resonance, one cannot arrive at any conclusion regarding the

TABLE 11. Summary Of Data Obtained By Electric Quadrupole Resonance In Spodumene And EPR Of  $\text{Fe}^{+3}$  And  $\text{Mn}^{+2}$  In Spodumene And Heat-Treated Kunzite.

	${}^7\text{Li}$ sites	${}^{27}\text{Al}$ sites
$C_z = eQ\phi_{zz}/h$ in mc/sec	0.076 <sup>a</sup>	2.950 <sup>b</sup>
$\eta$	0.79	0.94
$\phi_{zz}$ (e.s.u./cm <sup>3</sup> )	$1.0 \times 10^{13c}$	$2.6 \times 10^{14b}$
$\phi'_{zz} = \phi_{zz}/(1 - \delta)$ e.s.u./cm <sup>3</sup>	$1.3 \times 10^{13c}$	$7.2 \times 10^{13c}$
$C_z$ for ${}^{57}\text{Fe}$ (in mc/sec)	2.7 <sup>d,e</sup>	15.1
<u>Direction of principal axes of <math>\nabla E</math> tensor</u>		
z	46.5° from c towards a axis <sup>a</sup>	34° from c away from a axis <sup>b</sup>
y	Along b axis	56° from c towards a
x	43.5° from c away from a axis	Along b axis
<u>EPR of <math>\text{Fe}^{+3}</math> in spodumene</u>		
z - magnetic axis		5° from c towards a axis <sup>f</sup>
y - magnetic axis		along b axis
$\eta = b_2^2 / b_0^2$		0.20 <sup>f</sup>
<u>EPR of <math>\text{Mn}^{+2}</math> in heat-treated kunzite</u>		
z - magnetic axis		26° from c toward a axis <sup>f</sup>
y - magnetic axis		along b axis
$\eta = \frac{b_2^2}{b_0^2}$		0.42 <sup>f</sup>

<sup>a</sup>Volkoff et al<sup>16</sup>.

<sup>b</sup>Petch et al<sup>17</sup>.

<sup>c</sup> Appropriate  $\phi$  and  $\gamma_{\infty}$  as given by Bersohn<sup>31</sup>.

<sup>d</sup>  $Q$  for  $^{57}\text{Fe}$  given by Burns<sup>36</sup>.

<sup>e</sup>  $\gamma_{\infty}$  for  $\text{Fe}^{+3}$  given by Burns et al<sup>37</sup>.

<sup>f</sup> This investigation.

location of the iron and manganese impurities in spodumene. From quadrupole resonance, the values of  $\eta$  for the lithium and aluminum sites are 0.79 and 0.94, respectively. The values obtained from EPR measurements for iron and manganese are 0.20 and 0.42, respectively. Probably one cannot make an exact comparison because the iron and manganese impurities distort the sites considerably and the simple crystal field theory breaks down. Nicholson and Burns<sup>38</sup> also find that the  $\eta$  values for  $\text{Fe}^{+3}$  in  $\text{Ti}_2\text{O}_3$ , obtained by quadrupole resonance and Mössbauer effect, do not correspond very closely. They conclude that there is strong covalent bonding and the ionic model of crystal field theory is inadequate. Burns<sup>36</sup> finds a similar discrepancy in GASH.

From the point of view of charge compensation, the  $\text{Fe}^{+3}$  ions is most likely to replace an  $\text{Al}^{+3}$  ion substitutionally in spodumene. It is possible to account for the splitting of the  $\text{Mn}^{+2}$  complex into four complexes if one assumes that the  $\text{Mn}^{+2}$  ion also substitutes for an  $\text{Al}^{+3}$  ion. In this case there will be a net negative charge at the manganese site. It is possible that a single positively charged ion such as  $\text{Li}^+$  or  $\text{Na}^+$  is trapped in an interstitial site near the manganese ion. The crystal symmetry allows eight such sites (related in pairs

by the inversion centers). An interaction between compensating charges and the  $Mn^{+2}$  ions could cause the observed splitting.

There are additional reasons for believing that this mechanism could be responsible for the splitting. One reason is that the crystal heating caused the spectral lines due to the four  $Mn^{+2}$  complexes to decrease their intensities gradually while spectral lines due to  $Mn^{+2}$  in a single complex formed and increased their intensities with increasing temperature. This would mean that the compensating charges which are associated with the  $Mn^{+2}$  impurity before heating gradually dissociate as the temperature increases. Another reason for believing that compensating charges cause the observed splitting is due to the fact that the  $Fe^{+3}$  line widths increased after thermal quenching. This is explained as follows. Before heating, the combination of the net negative charge at the  $Mn^{+2}$  site with the compensating  $M^+$  cation acts as a dipole. This dipole interacts with an  $Fe^{+3}$  ion with an interaction proportion to  $1/r^3$ , as illustrated in Figure 31 (a). After heating, the  $M^+$  cation is removed from the vicinity of the  $Mn^{+2}$  ion and hence has a larger monopole interaction varying as  $1/r$  with the  $Fe^{+3}$  ion. This is illustrated in Figure 31 (b).

It is possible to obtain an estimate of the dissociation energy by applying the formula

$$n_d = N \exp\left[ (E_1 - E_2)/kT \right]$$

as done by Watkins<sup>11</sup>. Here,  $N$  is the total number of associated pairs  $n_a$  plus dissociated pairs  $n_d$ , i.e.  $N = n_a + n_d$ , and  $E_1 - E_2$  is the dissociation energy. This energy can conveniently be

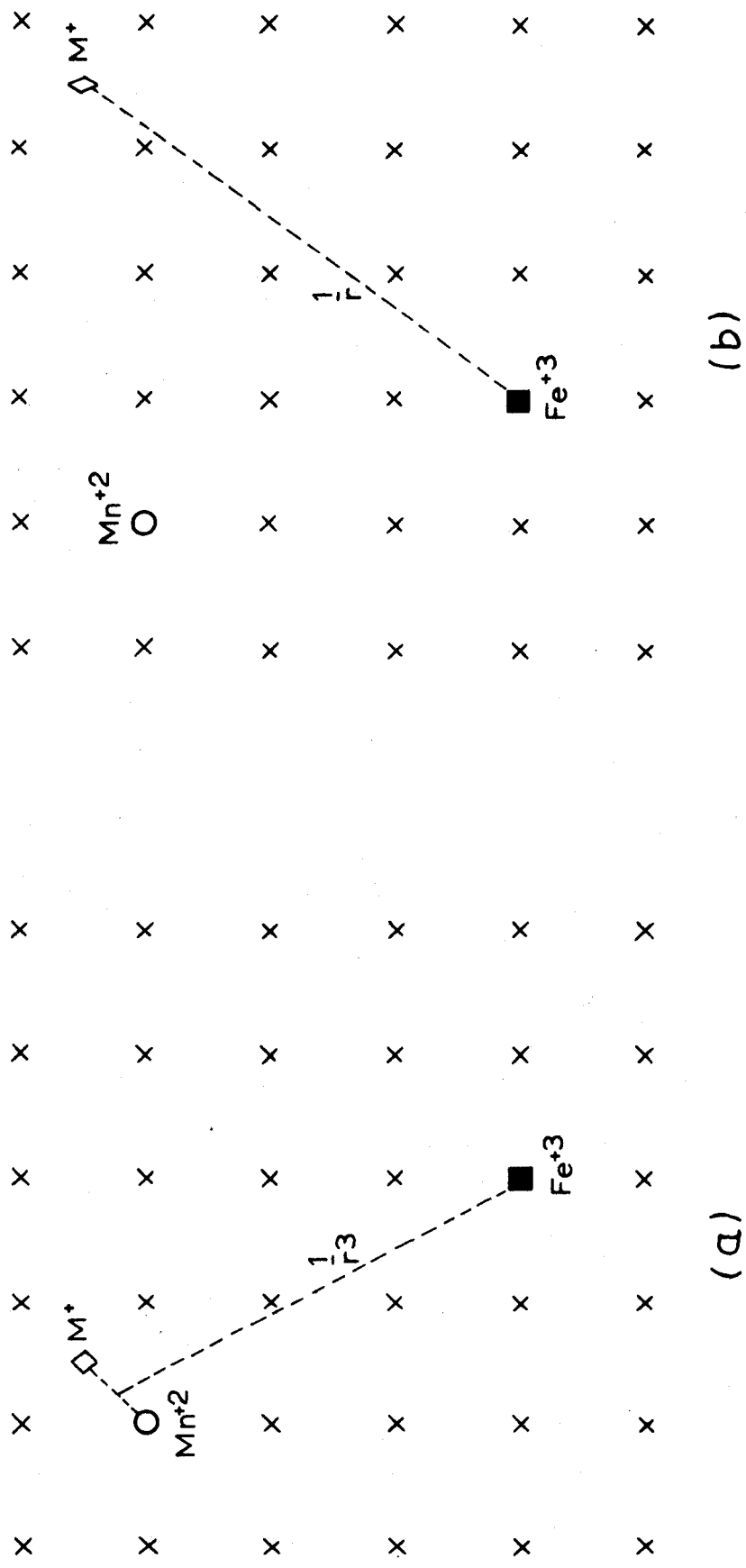


Fig. 31. Diagrams illustrating the mechanism causing broadening of the Fe<sup>+3</sup> EPR lines: (a) before thermal quenching and (b) after thermal quenching.

written as

$$E_1 - E_2 = \left[ \ln \left( \frac{n_d/n_a}{1 + n_d/n_a} \right) \right] 1/kT. \quad (15)$$

Assuming that the ratio of the amplitude of growth of the single complex spectrum to the amplitude of the decreased four-complex spectra is proportional to  $n_d/n_a$ , then the results of Figure 29 can be used to plot equation (15). This is done in Figure 32, with the slope of the line giving a value of  $E_1 - E_2 = 0.068$  e.v. For  $Mn^{+2}$  in alkali chlorides Watkins<sup>11</sup> obtains approximately 0.03 e.v. His result is smaller because he observes dissociation even at room temperature.

The integrated line intensities of  $Fe^{+3}$  in spodumene are approximately 1.7:4.5:9:4.5:1.7, before and after heat-treatment. The theoretical intensity ratios are 5:8:9:8:5. The intensity ratios for the  $Mn^{+2}$  lines before heating are: 1:3:9:3:1, and after thermal quenching are 3:5:9:5:3. A similar discrepancy from the theoretical ratios is obtained for  $Fe^{+3}$  and  $Mn^{+2}$  in MgO by Low<sup>39,40</sup>. He finds the ratios to be approximately 1.4:3.8:9:3.8:1.4 and attributes their difference from the theoretical ratios to be due to crystal defects.

The pink color of kunzite can be due to  $Mn^{+2}$  ions. Upon thermal quenching the crystal becomes bleached. This effect may be related to the interaction caused by the compensating ions and the  $Mn^{+2}$  ions, with the thermal quenching causing a shift of the pink color into the infrared region.

From the work of Van Wieringen<sup>9</sup> it is seen that the magnitude of the hyperfine constant,  $A$ , depends on the amount of covalent bonding in the crystal. That is, the greater the co-

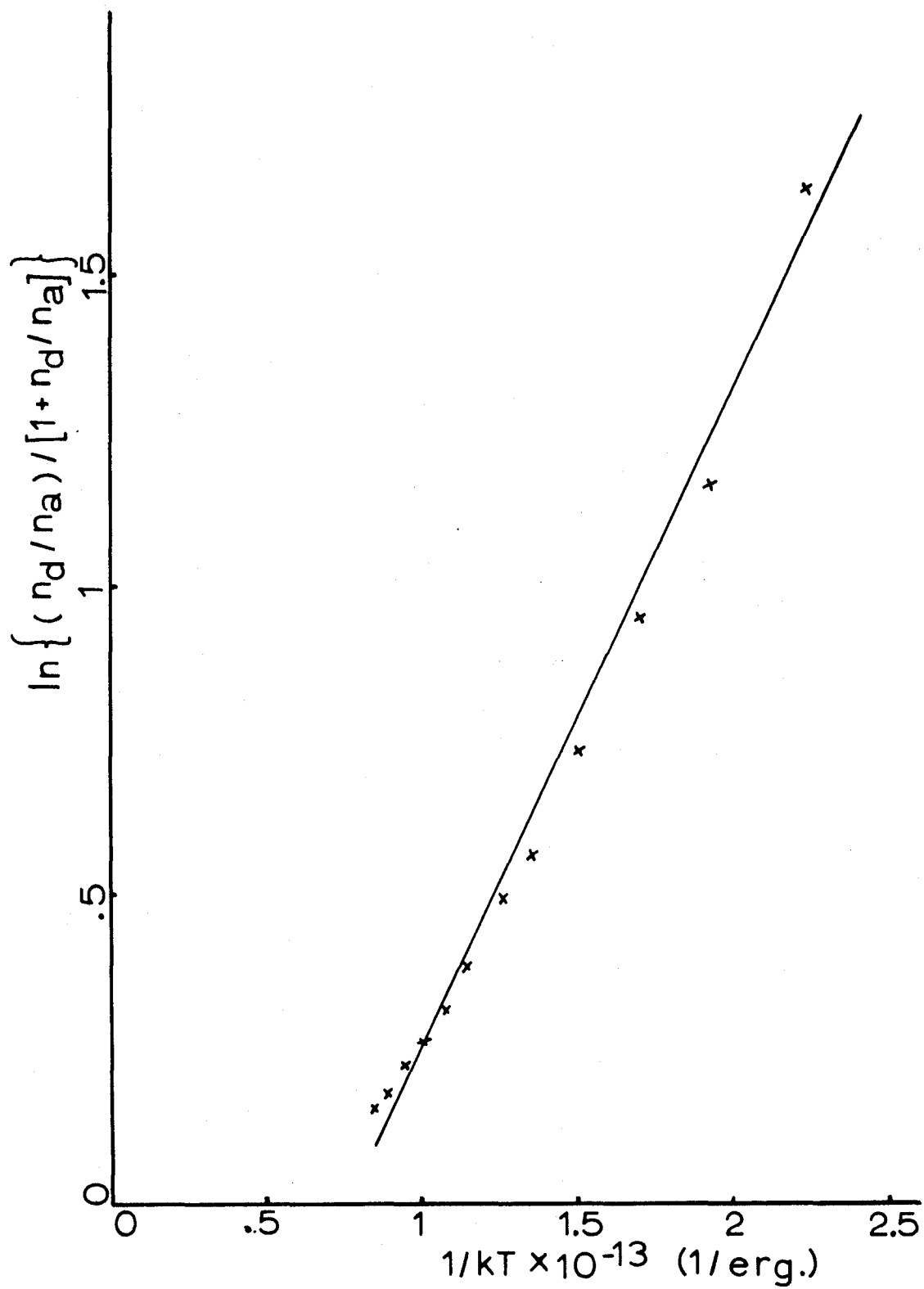


Fig. 32. Dissociation energy curve.

valent bonding, the smaller will be the hyperfine splitting. Using Matumura's<sup>10</sup> plot of percent ionicity versus the magnitude of the hyperfine structure constant  $A$ , we find that for  $A = 89$  gauss (or  $83 \times 10^{-4} \text{ cm}^{-1}$ ), as is the case for  $\text{Mn}^{+2}$  in kunzite, there is about 91% ionicity or 9% covalency.

The values of  $g$  and  $b_2^0$  for  $\text{Fe}^{+3}$  found in this investigation can be compared to those found by Geschwind<sup>41</sup> for  $\text{Fe}^{+3}$  in the tetrahedral sites of yttrium iron garnet. His results are  $g = 2.0047$  and  $b_2^0 = 1,386$  gauss. For the case of  $\text{Mn}^{+2}$  replacing Mg in diopside crystals, Vinokurov et al obtained  $g_x = 2.0016$ ,  $g_y = 2.0016$ ,  $g_z = 2.0017$ ,  $A = 84.4$ ,  $B = 84.4$ ,  $C = 81.9$ ,  $b_2^0 = 452.95$ ,  $b_2^2 = -308.5$ ,  $b_4^0 = 0.34$ ,  $b_4^2 = -4.74$  and  $b_4^4 = 15.88$ . The values of  $A$ ,  $B$ ,  $C$  and  $b_n^m$  are in gauss.

## REFERENCES

1. B. Bleaney and D.J.E. Ingram, Proc. Roy. Soc. A205, 336(1951).
2. J.H. Van Vleck and W.G. Penney, Phil. Mag. 17, 961(1934).
3. A. Abragam and M.H.L. Pryce, Proc. Roy. Soc. A205, 135(1951).
4. H. Watanabe, Progr. Theoret. Phys. (Kyoto) 18, 405(1957).
5. J.R. Gabriel, D.F. Johnson and M.J.D. Powell, Proc. Roy. Soc. A264, 503 (1961).
6. A.M. Leushin, Soviet Phys. Solid State (English Transl.) 5, 2477 (1964).
7. H. Watanabe, J. Phys. Chem. Solids 25, 1471 (1964).
8. J. Owen, Proc. Roy. Soc. A227, 183 (1955).
9. J.S. Van Wieringen, Disc. Faraday Soc. 19, 118 (1955).
10. O. Matumura, J.Phys. Soc Japan 14, 108 (1959).
11. G.D. Watkins, Phys. Rev. 113, 79 and 91 (1959).
12. H.J. Gerritsen, Paramagnetic Resonance Volume 1 p.3. (Academic Press Inc., New York).
13. R.S. Rubins and W. Low, Paramagnetic Resonance Volume 1 p.59. (Academic Press Inc., New York).
14. E.S. Kirkpatrick, K.A. Muller and R.S. Rubins, Phys.Rev. 135, A86 (1964).
15. V.M. Vinokurov, M.M. Zaripov and V.G. Stepanov, Soviet Phys. Solid State (English Transl.) 6, 870 (1964).
16. G.M. Volkoff, H.E. Petch and D.W.L. Smellie, Can.J.Phys. 30, 270 (1952).
17. H.E. Petch, N.G. Cranna and G.M. Volkoff, Can. J. Phys. 31, 837 (1953).
18. A. Manoogian, F. Holuj and J.W. Carswell, Can. J. Phys. 43, 2262 (1965).

19. J.W. Carswell, M. Sc. Thesis, Department Of Physics, University Of Windsor, Windsor, Ontario, 1964 (unpublished).
20. R.W.G. Wykoff, Crystal Structures, Vol. III, (Interscience Publishers Inc., New York) 1960.
21. L. Pauling, The Nature Of The Chemical Bond (Cornell University Press, Ithaca, New York) 1960.
22. R.B. Leighton, Principles Of Modern Physics, (McGraw-Hill Book Co., New York) 1959.
23. H. Bethe, Ann. Physik 3, 133 (1929).
24. E. Wigner, Nachr. Akad. Wiss. Gottingen, Math. - physik Kl. II a, 546 (1932).
25. M.H.L. Pryce, Proc. Phys. Soc. A63, 25 (1950).
26. R. Orbach, Proc. Roy. Soc. A264, 458 (1961).
27. K.W.H. Stevens, Proc. Phys. Soc. A65, 209 (1952).
28. D.A. Jones, J.M. Baker and D.F.D. Pope, Proc. Phys. Soc. 74, 249 (1959).
29. W. Low, Paramagnetic Resonance In Solids (Academic Press, New York) 1960.
30. J.H. Van Vleck, Phys. Rev. 57, 426 (1940).
31. R. Bersohn, J. Chem. Phys. 29, 326 (1958).
32. E. Condon and G.H. Shortly, The Theory Of Atomic Spectra (Cambridge University Press, Cambridge) 1953.
33. C.J. Ballhausen, Introduction To Ligand Field Theory (McGraw-Hill Book Co., New York) 1962, p. 110.
34. Reference Data For Radio Engineers, p. 636. (International Telephone and Telegraph Corp. New York).
35. G.M. Volkoff, Can. J. Phys. 31, 820 (1953).
36. G. Burns, Phys. Rev. 124, 524 (1961).
37. G. Burns and G.E. Wikner, Phys. Rev. 121, 155 (1961).
38. W.J. Nicholson and G. Burns, Phys. Rev. 129, 2490 (1963).
39. W. Low, Proc. Phys. Soc. BLXIX, 1169 (1956).

40. W. Low, Phys. Rev. 105, 793 (1957).
41. S. Geschwind, Phys. Rev. 121, 363 (1961).

## VITA AUCTORIS

I was born in Galt, Ontario, on June 16, 1934, where I received my early education. Upon completion of high school I worked for nearly three years as a draftsman in Galt. In 1955 I enrolled in the science course at McMaster University, in Hamilton, Ontario, and in 1959 I received a B.A. degree in science studies.

I have done graduate work at Fresno State College, in Fresno, California, where I received an M.S. degree in physics in 1961. From there I went to McGill University, in Montreal, Quebec, where I received an M.Sc. degree in physics in 1963. I started my Ph.D studies at the University of Windsor in 1964. While at the University of Windsor I have received a Fellowship from the Ontario Government.